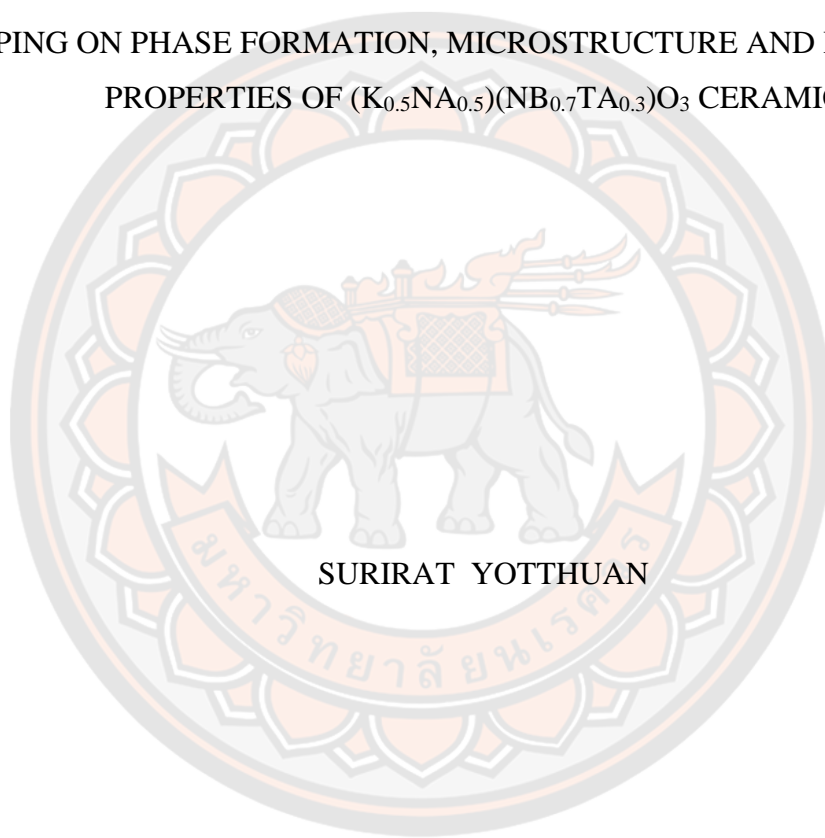




INFLUENCES OF LITHIUM/CAESIUM ADDITIONAL/SUBSTITUTIONAL
DOPING ON PHASE FORMATION, MICROSTRUCTURE AND ELECTRICAL
PROPERTIES OF $(K_{0.5}Na_{0.5})(Nb_{0.7}Ta_{0.3})O_3$ CERAMICS



A Thesis Submitted to the Graduate School of Naresuan University
in Partial Fulfillment of the Requirements
for the Doctor of Philosophy in Applied Physics - (Type 1.1)

2021

Copyright by Naresuan University

INFLUENCES OF LITHIUM/CAESIUM ADDITIONAL/SUBSTITUTIONAL
DOPING ON PHASE FORMATION, MICROSTRUCTURE AND ELECTRICAL
PROPERTIES OF $(K_{0.5}Na_{0.5})(Nb_{0.7}Ta_{0.3})O_3$ CERAMICS



A Thesis Submitted to the Graduate School of Naresuan University
in Partial Fulfillment of the Requirements
for the Doctor of Philosophy in Applied Physics - (Type 1.1)
2021

Copyright by Naresuan University

Thesis entitled "INFLUENCES OF LITHIUM/CAESIUM
ADDITIONAL/SUBSTITUTIONAL DOPING ON PHASE FORMATION,
MICROSTRUCTURE AND ELECTRICAL PROPERTIES OF
(K_{0.5}Na_{0.5})(Nb_{0.7}Ta_{0.3})O₃ CERAMICS"

By SURIRAT YOTTHUAN

has been approved by the Graduate School as partial fulfillment of the requirements
for the Doctor of Philosophy in Applied Physics - (Type 1.1) of Naresuan University

Oral Defense Committee

..... Chair
(Associate Professor Orawan Ritthidech, Ph.D.)

..... Advisor
(Associate Professor Theerachai Bongkarn, Ph.D.)

..... Co Advisor
(Associate Professor Tawat Suriwong, Ph.D.)

..... Co Advisor
(Assistant Professor Sasipohn Prasertpalichat, Ph.D.)

..... Internal Examiner
(Assistant Professor Jaru Jutimoosik, Ph.D.)

Approved

.....
(Associate Professor Krongkarn Chootip, Ph.D.)

Dean of the Graduate School

Title	INFLUENCES OF LITHIUM/CAESIUM ADDITIONAL/SUBSTITUTIONAL DOPING ON PHASE FORMATION, MICROSTRUCTURE AND ELECTRICAL PROPERTIES OF (K _{0.5} NA _{0.5})(NB _{0.7} TA _{0.3})O ₃ CERAMICS
Author	SURIRAT YOTTHUAN
Advisor	Associate Professor Theerachai Bongkarn, Ph.D.
Co-Advisor	Associate Professor Tawat Suriwong, Ph.D.
Academic Paper	Assistant Professor Sasipohn Prasertpalichat, Ph.D. Ph.D. Dissertation in Applied Physics - (Type 1.1), Naresuan University, 2021
Keywords	KNNT, Phase formation, Rietveld refinement, Electrical properties, Solid-state combustion method

ABSTRACT

The effect of the firing conditions on the phase formation, microstructure, and electrical properties of (K_{0.5}Na_{0.5})(Nb_{0.7}Ta_{0.3})O₃ (KNNT) ceramics synthesized by the solid-state combustion technique using glycine as fuel has been investigated. All samples were calcined at 600 to 800°C for 2 h and sintered at 1150 to 1190°C for 2 to 5 h. Pure KNNT powders were produced after calcination at 600°C for 2 h. The average particle size increased when the calcination temperature was increased. The KNNT powder calcined at 600°C for 2 h showed rather square morphology with average particle size of ~160 nm. The x-ray diffraction (XRD) analysis results for the ceramics revealed the presence of orthorhombic (*O*) and tetragonal (*T*) phases in all samples. When sintering at 1150°C for 4 h, the *O*:*T* ratio was 50:50, as verified by the Rietveld refinement technique. The average grain size, density values, and dielectric properties tended to increase when the dwell time was increased from 2 to 4 h, but then degraded. The KNNT ceramic produced at the optimum firing condition (1150°C for 4 h) showed good crystalline morphology, the highest density ($\rho = 5.28 \text{ g/cm}^3$), the highest dielectric constant ($\epsilon_C = 5002$), and good ferroelectric behavior ($P_r = 18.50 \text{ } \mu\text{C/cm}^2$ and $E_c = 9.04 \text{ kV/cm}$).

Then, the effects of Cs⁺ substitution and direct doping in

($\text{K}_{0.5}\text{Na}_{0.5}$)($\text{Nb}_{0.7}\text{Ta}_{0.3}$) O_3 (KNNT) ceramics, on the crystal structure, microstructure and electrical properties were investigated. Both the KNNT with Cs^+ substitution ($\text{K}_{0.5-x}\text{Cs}_x\text{NNT}$) and addition (KNNT- $x\text{Cs}$) ($x=0, 0.01, 0.02, 0.03$ and 0.04 mol.%) were synthesized by the solid-state combustion technique using glycine as fuel. All samples were sintered at $1130\text{-}1150^\circ\text{C}$ for 4 h. The x-ray diffraction (XRD) analysis for the ceramics revealed the presence of *O* and *T* phases in all samples. Increasing both the Cs^+ substitution and doping amounts, enhanced orthorhombicity, as verified by the Rietveld refinement technique. It was found that Cs^+ doping, either substitutional or additional, strongly decreased their density, dielectric and ferroelectric properties. The undoped KNNT ceramic exhibited well-saturated *P-E* hysteresis loop. With Cs^+ doping, the samples became unsaturated and a leakage current was produced. The KNNT- $x\text{Cs}$ ceramics demonstrated higher density and dielectric properties than the $\text{K}_{0.5-x}\text{Cs}_x\text{NNT}$ ceramics.

After that, lead-free ($\text{K}_{0.5}\text{Na}_{0.5}$)($\text{Nb}_{0.7}\text{Ta}_{0.3}$) O_3 (KNNT) ceramics with Li^+ substitution ($\text{KN}_{0.5-x}\text{Li}_x\text{NT}$) and direct (KNNT- $x\text{Li}$) doping at $x=0, 0.01, 0.02, 0.03$ and 0.04 mol.% were synthesized by the solid-state combustion route. The phase, microstructure, dielectric and ferroelectric properties of the ceramics were examined. The XRD pattern of the ceramics revealed orthorhombic and tetragonal phases were in all specimens. The Rietveld refinement procedure showed that increasing either the Li^+ substitution or doping levels enhanced the amount of the tetragonal phase. It was found that Li^+ doping, either substitutional or additional, enhanced the Curie temperature (T_C) by increasing the tetragonal distortion, while the dielectric constant (ϵ_C) decreased. The good remanent *P-E* loops of the $\text{KN}_{0.5-x}\text{Li}_x\text{NT}$ ceramics was found with $x=0.01$ ($P_r \sim 10.89 \mu\text{C}/\text{cm}^2$ and $E_C \sim 13.09 \text{ kV}/\text{cm}$), while for KNNT- $x\text{Li}$ ceramics, it was obtained with $x=0.02$ ($P_r \sim 15.65 \mu\text{C}/\text{cm}^2$ and $E_C \sim 11.46 \text{ kV}/\text{cm}$), which were confirmed by remanent *P-E* hysteresis measurements.

ACKNOWLEDGEMENTS

I would like to express the deepest gratitude to my advisor, Associate Professor Theerachai Bongkarn, Ph.D, and co-advisor Assistant Professor Sasipohn Prasertpalichat, Ph.D. and Associate Professor Tawat Suriwong, Ph.D, for his initial idea, guidance, and encouragement which enable me to carry out my study successfully. I consider it as a great opportunity to do my doctoral program under his advice and to learn from his research expertise.

My sincere gratitude also goes to my thesis committee, Associate Professor Orawan Ritthidech, Ph.D, and Assistant Professor Jaru Jutimoosik, Ph.D. for their helpful advice, comments and suggestions.

My profound thanks to Department of Physics, Faculty of Science, Naresuan University for being warmest places to study since the researcher studied a Bachelor's degree and Doctoral degree here. I feel love and commitment with here. I would like to thank Science Lab Center and Miss Thanita Sutthatang for XRD analysis, Mr. Seangphet Boonpang and Miss Prakaitip Kitikhun for from SEM analysis for their assistance in the part of instrument.

I would like to acknowledge the Science Achievement Scholarships of Thailand (SAST) Ph.D. Program to Miss Surirat Yotthuan all financial support during this study.

Finally, I would like to thank my family for their love and their understanding. They have been constantly providing me with encouragement, enjoyment during my life and enabled me to complete this thesis.

SURIRAT YOTTHUAN

TABLE OF CONTENTS

	Page
ABSTRACT.....	C
ACKNOWLEDGEMENTS.....	E
TABLE OF CONTENTS.....	F
LIST OF TABLES.....	H
LIST OF FIGURES.....	I
CHAPTER I INTRODUCTION.....	1
Overview.....	1
Research objectives.....	3
Research expected outputs.....	3
Research scope.....	4
CHAPTER II RELATED THEORY AND LITERATURE REVIEW.....	5
Fundamental theory.....	5
A literature reviews.....	17
CHAPTER III RESEARCH METHODOLOGY.....	37
Samples Synthesis.....	37
Samples Characterization.....	43
CHAPTER IV RESULTS AND DISCUSSION.....	56
1. Effect of firing conditions on phase formation, microstructure, and electrical properties of $(K_{0.5}Na_{0.5})(Nb_{0.7}Ta_{0.3})O_3$ ceramics synthesized by solid-state combustion method.....	56
2. The influences of Cs^+ substitution and direct doping on the phase evolution, microstructure and electrical properties of KNNT ceramics.....	74
3. The phase evolution, microstructure and electrical response of KNNT ceramics with Li^+ substitution and doping.....	87
CHAPTER V SUMMARY.....	99
REFERENCES.....	102

BIOGRAPHY 114



LIST OF TABLES

	Page
Table 1 The density values, dielectric properties and piezoelectric coefficient at room temperature of the $K_{0.5}Na_{0.5}Nb_{1-x}Ta_xO_3$ ceramics with different x.	23
Table 2 Crystal data and structure refinement conditions for the KNN-0.06Li and KNN-0.07Li. The distortions for orthorhombic phase and tetragonal phase are designed as $2(c-b)/(c+b)$	30
Table 3 Goodness of fit parameters, lattice parameters, atomic information and the percentage of phases for KNNT ceramics with different dwell times during sintering.	62
Table 4 The ratio of all element spectrums of the KNNT ceramics with different dwell times.	66
Table 5 Dielectric and ferroelectric properties of the KNNT ceramics sintered at 1150°C with the different dwell times.	72
Table 6 Goodness of fit, volume cell and phase percentage of the KNNT ceramics with different Cs^+ substitutional and additional doping.	78
Table 7 Dielectric and ferroelectric properties of KNNT ceramics as a function of Cs^+ additional and substitutional doping.	85
Table 8 The goodness of fit parameters, lattice parameters and the percentage of phases for the $KN_{0.5-x}Li_xNT$ and $KNNT-xLi$ ceramics as a function of x.	90
Table 9 Chemical compositions of the $KN_{0.5-x}Li_xNT$ and $KNNT-xLi$ ceramics as a function of x.	93
Table 10 Dielectric and ferroelectric behaviors of KNNT ceramics as a function of Li^+ additional and substitutional doping.	98

LIST OF FIGURES

	Page
Figure 1 Various types perovskite unit cells. Blue spheres refer to the A cations, yellow spheres refer to the B cations and red spheres refer to oxygen anions forming an octahedra.	6
Figure 2 Geometric characteristics of the 7 crystal systems and 14 Bravais lattices. ..	7
Figure 3 (a) Diagram of a polycrystalline specimen. A polycrystal is consist of numerous grains separated from one another by areas of disorder called grain boundaries and (b) Normal microstructure as seen via an optical microscope.....	8
Figure 4 A normal hysteresis loop in ferroelectrics, including domain reversal (polarization rotation) and strain-electric field curve.	10
Figure 5 (a) Parallel-plate capacitor of area A and separation d in vacuum connect with DC power source. (b) Closing of the circuit results in a transient surge of current to flow through the circuit. Charge collected on the capacitor is equal to the area under the curve. (c) Same as (a) except, now a dielectric is placed between the plates. (d) Closing of the circuit caused a charge retained on the parallel plates, which has to be greater than that stored in (b).	12
Figure 6 Functional dependence of Q on applied voltage. Slope of curve is associated to the dielectric constant of the materials.	13
Figure 7 Schematic of two possible paths by which a collection of particles can lower its energy. (a) Densification followed by grain growth. In this case shrinkage of the compact has to happen (b) Coarsening where the large grains grow at the expense of the smaller ones.....	14
Figure 8 (a) Equilibrium dihedral angle between grain boundary and solid/vapor interfaces, (b) Equilibrium dihedral angle between grain boundary and liquid phase.	15
Figure 9 (a) The spheres in tangential contact indicate the initial phase of the sintering model, (b) The spheres have begun to form as the initial phase draws to a close, (c) Intermediate phase; grains adopted shape of dodecahedra, enclosing pore channels at grain boundary, (d) Pores are tetrahedral inclusions in the corners where four dodecahedra converge in the final phase.....	16
Figure 10 Orthorhombic perovskite structure of KNN ceramic at room temperature.	18
Figure 11 The phase transitions of KNN ceramics.	19

Figure 12 The binary phase diagram of $\text{KNbO}_3\text{-NaNbO}_3$	19
Figure 13 XRD pattern at room temperature of the $\text{K}_{0.5}\text{Na}_{0.5}\text{Nb}_{1-x}\text{Ta}_x\text{O}_3$ ceramics with $x=0\text{-}0.30$ mol.%	21
Figure 14 SEM images of $\text{K}_{0.5}\text{Na}_{0.5}\text{Nb}_{1-x}\text{Ta}_x\text{O}_3$ ceramics with different x; (a) 0.00 mol.%, at 1090°C (b) 0.10 mol.%, at 1110°C, (c) 0.15 mol.%, at 1120°C, (d) 0.20 mol.%, at 1145°C, (e) 0.25 mol.%, at 1150°C and (f) 0.30 mol.%, at 1170°C.	22
Figure 15 The dielectric constant against temperature of the $\text{K}_{0.5}\text{Na}_{0.5}\text{Nb}_{1-x}\text{Ta}_x\text{O}_3$ ceramics with various x, measured at 100 kHz.....	23
Figure 16 The evolution of d_{33} in $\text{K}_{0.5}\text{Na}_{0.5}\text{Nb}_{1-x}\text{Ta}_x\text{O}_3$ ceramics with different x.	24
Figure 17 Polarization hysteresis loops of the KNNT ceramics at different sintering temperature.	25
Figure 18 XRD patterns at room temperature of the KNN-xLi ceramics in the 2θ (a) $20\text{-}60^\circ$ and (b) $31\text{-}47^\circ$, and the $I_{(022)}/I_{(200)}$ ratios of all samples as an inset in (a).	27
Figure 19 Rietveld refinements on XRD data for (a) the KNN-0.06Li and (b) the KNN-0.07Li ceramics.....	29
Figure 20 SEM micrographs of KNN-xLi ceramics with different x (a) 0, (b) 0.055, (c) 0.06, (d) 0.065 and (e) 0.07. The insets depict grain size distributions.....	31
Figure 21 Temperature dependence of (a) dielectric permittivity and (b) dielectric loss of the KNN-xLi samples with different x.....	32
Figure 22 The P_r , S_{33} and d_{33} for the KNN-xLi samples with different x.....	32
Figure 23 XRD patterns of 0.93KNN-0.07SZ-xLi ceramics in the 2θ range of (a) $10\text{-}70^\circ$ and (b) $44\text{-}48^\circ$	33
Figure 24 SEM image of 0.93KNN-0.07SZ-xLi ceramics with (a) $x=0$, (b) $x=0.03$, (c) $x=0.07$, (d) $x=0.10$, (e) $x=0.13$ and (f) The average grain size and bulk density of the 0.93KNN-0.07SZ-xLi ceramics with different x.	34
Figure 25 Temperature-dependent dielectric constant and dielectric loss of the 0.93KNN-0.07SZ-xLi ceramics with (a) $x=0$, (b) $x=0.03$, (c) $x=0.07$, (d) $x=0.10$, (e) $x=0.13$ and (f) The T_m and ϵ of the 0.93KNN-0.07SZ-xLi ceramics with different x.35	
Figure 26 (a) P-E loops and (b) the variation of P_r , d_{33} and k_p ; (c) d_{33} against annealing temperature of the 0.93KNN-0.07SZ-xLi samples with various x; (d) Schematic diagram explains why the sample with $x = 0.03$ has a high d_{33}	36
Figure 27 Diagram of the synthesis process of KNNT powders and ceramics.	39

Figure 28 Diagram of the synthesis process of $K_{0.5-x}Cs_xNNT$ powders and ceramics.	40
Figure 29 Diagram of the synthesis process of $KNNT-xCs$ ceramics.	41
Figure 30 Diagram of the synthesis process of $KN_{0.5-x}Li_xNT$ powders and ceramics.	42
Figure 31 Diagram of the synthesis process of $KNNT-xLi$ ceramics.	43
Figure 32 Diagram of samples characterization of $KNNT$ powders.	43
Figure 33 Diagram of samples characterization of $K_{0.5-x}Cs_xNNT$, $KNNT-xCs$, $KN_{0.5-x}Li_xNT$ and $KNNT-xLi$ ceramics.	44
Figure 34 X-ray diffraction instruments	45
Figure 35 Windows of the FullProf Suite toolbar.....	47
Figure 36 Rietveld refinement on XRD patterns of $KNNT$ ceramic at $1150^\circ C$ for 4 h.	47
Figure 37 The XPS analysis of surface for pure copper sample.....	48
Figure 38 X-ray photoelectron spectroscopy (XPS).....	49
Figure 39 Schematic diagram of typical scanning electron microscope.....	50
Figure 40 The interaction between an electron beam and electrons inside an atom used in EDS.....	51
Figure 41 Scanning electron microscope (SEM).....	51
Figure 42 Schematic diagram of typical transmission electron microscopy.	52
Figure 43 Transmission electron microscopy (TEM).....	53
Figure 44 The LCR meter at Naresuan University.	54
Figure 45 The computer controlled modified Sawyer Tower circuit.	55
Figure 46 X-ray diffraction patterns of $KNNT$ powders calcined at temperatures between 600 and $800^\circ C$ for 2 h in the 2θ range of $10-70^\circ$	57
Figure 47 SEM images of $KNNT$ powders calcined at the temperatures of: (a) 600 , (b) 650 , (c) 700 , (d) 750 and (e) $800^\circ C$ for 2 h.....	57
Figure 48 (a-c) TEM micrograph and (d) SAED pattern of $KNNT$ powders calcined at temperature of $600^\circ C$ for 2 h.	59

Figure 49 X-ray diffraction patterns of KNNT ceramics with various sintering temperatures in the 2θ range of (a) $10-70^\circ$ and (b) $24-36^\circ$; filled club, Nb_2O_5 ; filled circle, KNO_3 ; filled heart, KO_2 ; filled diamond, NaNO_2 ; filled spade, KNaO	60
Figure 50 X-ray diffraction patterns of KNNT ceramics at a sintering temperature of 1150°C for the different dwell times of 2-5 h in the 2θ range of $10-70^\circ$	61
Figure 51 Typical Rietveld refinement analysis for KNNT ceramics at different dwell times: (a) 2, (b) 3, (c) 4 and (d) 5 h.....	64
Figure 52 (a) The wide-range, high-resolution XPS spectrum of (b) Nb 3d, (c) Ta 4f, and (d) O 1s of KNNT ceramics as a function of dwell times.....	66
Figure 53 SEM images and EDS spectrums of KNNT ceramics sintered at 1150°C for different dwell times: (a), (e) 2 h, (b), (f) 3 h, (c), (g) 4 h and (d), (h) 5 h.....	67
Figure 54 The measured and relative density of KNNT ceramics at a sintering temperature of 1150°C for the different dwell times.	68
Figure 55 Temperature dependent of the dielectric constant and loss of KNNT ceramics at a sintering temperature of 1150°C for the different dwell times: (a) 2, (b) 3, (c) 4 and (d) 5 h.....	69
Figure 56 The plot of $\ln(1/\varepsilon-1/\varepsilon_C)$ versus $\ln(T-T_C)$ at 1 kHz for the KNNT ceramics at a sintering temperature of 1150°C for the different dwell times: (a) 2, (b) 3, (c) 4 and (d) 5 h.....	71
Figure 57 Polarization versus electric field (P-E) loops at room temperature for KNNT ceramics at a sintering temperature of 1150°C for 2-4 h.....	72
Figure 58 XRD patterns of the (a) $\text{K}_{0.5-x}\text{Cs}_x\text{NNT}$ and (b) KNNT-xCs ceramics with different x.....	75
Figure 59 Rietveld refinement on XRD patterns of the KNNT (a), the $\text{K}_{0.5-x}\text{Cs}_x\text{NNT}$ with $x=0.01$ (b) and $x=0.03$ (c), and the KNNT-xCs ceramics with $x=0.01$ (d) and $x=0.03$ (e); (f) the percentage of orthorhombic phase of the samples with different x.	77
Figure 60 SEM images of the (a) KNNT ceramic, (b-e) $\text{K}_{0.5-x}\text{Cs}_x\text{NNT}$ ceramics with $x=0.01-0.04$ and (f-i) KNNT-xCs ceramics with $x=0.01-0.04$	80
Figure 61 Measured density of the $\text{K}_{0.5-x}\text{Cs}_x\text{NNT}$ and KNNT-xCs ceramics as a function of x.....	81
Figure 62 EDS spectra of the $\text{K}_{0.5-x}\text{Cs}_x\text{NNT}$ ceramics with (a) $x=0.01$, (b) $x=0.04$ and the KNNT-xCs ceramics with (c) $x=0.01$ and (d) $x=0.04$	81
Figure 63 Elemental mapping of (a) the $\text{K}_{0.5-x}\text{Cs}_x\text{NNT}$ ceramic with $x=0.04$ and (b) the KNNT-xCs ceramic with $x=0.04$	82

Figure 64 Temperature dependence of the dielectric constant and dielectric loss for the (a) $K_{0.5-x}Cs_xNNT$ and (b) $KNNT-xCs$ ceramics with different x.....	84
Figure 65 Ferroelectric hysteresis (P-E) loops at room temperature for the (a) $K_{0.5-x}Cs_xNNT$ and (b) $KNNT-xCs$ ceramics with different x.	86
Figure 66 Room temperature XRD patterns of the (a) $KN_{0.5-x}Li_xNT$ and (b) $KNNT-xLi$ ceramics with various x.....	88
Figure 67 Rietveld refinement on XRD patterns of the $KNNT$ (a), the $KN_{0.5-x}Li_xNT$ with $x=0.01$ (b) and $x=0.03$ (c), and the $KNNT-xLi$ ceramics with $x=0.01$ (d) and $x=0.03$ (e); (f) the percentage of tetragonal phase of the samples with various x.	89
Figure 68 SEM micrographs of the (a) $KNNT$ ceramics, (b-e) $KN_{0.5-x}Li_xNT$ ceramics with $x=0.01-0.04$ and (f-i) $KNNT-xLi$ ceramics with $x=0.01-0.04$	91
Figure 69 The measured density of the $KN_{0.5-x}Li_xNT$ and $KNNT-xLi$ ceramics as a function of x.....	93
Figure 70 Temperature dependence of the dielectric constant and the loss tangent of the (a) $KN_{0.5-x}Li_xNT$ and (b) $KNNT-xLi$ ceramics with various x, measured at 1 kHz.	94
Figure 71 Room-temperature P-E hysteresis loops of the $KN_{0.5-x}Li_xNT$ ceramics with $x=0.01-0.04$	96

CHAPTER I

INTRODUCTION

Overview

Since the 1650s, the (PbZr_{1-x}Ti_xO₃, PZT)-based materials have been given extremely interest owing to their outstanding piezoelectric constants (d_{33} ~200-750 pC/N) and high Curie temperatures (T_C ~180-320°C) and are presently applied in many electronic devices (e.g., multilayer ceramic capacitors, sensors, actuators, ultrasonic transducers, energy harvesters, and so on) (1-4). Nevertheless, the element of lead (Pb) is dangerous, and high levels (>60 wt.%) of Pb content in the PZT-based ceramics generate great threat to the environmental and human health, including the use of hazardous chemicals in electronic devices has been increasingly banned by laws and regulations (1-4). As a result, scientists have focused their utmost efforts on the development of lead-free replacements. Among various without lead materials (5-7), sodium potassium niobate (K,Na)NbO₃ (KNN) ceramics, the solid solution of ferroelectric KNbO₃ and antiferroelectric NaNbO₃, are one good contestant for lead-free ceramics owing to its great piezoelectric coefficient (d_{33}), high Curie temperature (T_C), large electromechanical coupling factor (k_p) and environmentally friendly chemical composition (8). Unfortunately, a few shortcomings, e.g., poor ferroelectric properties (existing leakage current) and low dielectric constant (ϵ), still preclude huge industrial applications of KNN-based ceramics on account of poor sintering and low density caused by the fluctuation of K₂O and Na₂O compounds at high temperatures. Li et al. (9) synthesized the lead-free K_{0.5}Na_{0.5}Nb_{0.7}Ta_{0.3}O₃ (KNNT) ceramic using a novel hydro/solvothermal technique. The ceramics exhibited coexistence of orthorhombic and tetragonal phases and showed high density (ρ ~93.82%). After that, Lv et al. (10) fabricated KNNT ceramic using the solid-state reaction technique (with calcination at 900°C for 5 h and sintering at 1170°C for 2 h). The samples showed high ρ (~94.40%), dielectric constant at T_C (ϵ_C ~6,000) and T_C (~230°C).

Recently, many studies proved that improvement in the density and electric properties of lead-free materials can be accomplished by adding and/or substituting with a small number of other elements or compounds, such as CoO, CuO, CrO, Fe₂O₃, In₂O₃, Li₂CO₃, MnO, and NiO (11-19). For the direct doping of element in KNN-based ceramics, J. Liu et al. (12) reported that direct doping with Cu²⁺ at an amount of 0.01 mol.% into 0.98K_{0.5}Na_{0.5}NbO₃-0.02BiScO₃ ceramics enhanced the ρ (~4.6 g/cm³), ϵ_C (~5500) and d_{33} (~207 pC/N). In 2016, the maximum ϵ_C (~7520), remnant polarization (P_r ~27.9 $\mu\text{C}/\text{cm}^2$) and d_{33} (~311 pC/N) of (K_{0.44}Na_{0.52}Li_{0.04})(Nb_{0.84}Ta_{0.10}Sb_{0.06})O₃ ceramics were obtained from additional doping Fe³⁺ at 0.6 wt.%, as announced by T. Bongkarn et al. (14). Next, Y. Zhao et al. (15) observed that additional doping of 1 mol% In³⁺ into KNN ceramics could improve P_r ~31.52 $\mu\text{C}/\text{cm}^2$ compared with the undoped ceramics. In that instance of the substitution doping in KNN-based ceramics, C. Long et al. (16) suggested that substitutional doping of Na⁺ and K⁺ by 0.06 mol.% Li⁺ in A-sites of (Na_{0.5}K_{0.5})_{0.94}Li_{0.06}NbO₃ ceramics can enhanced the T_c (~473°C), P_r (~29 $\mu\text{C}/\text{cm}^2$) and large field-induced strain (S_{33} ~0.152%). Similarly, the modified 0.96(K_{0.48}Na_{0.49}Li_{0.03})NbO₃-0.04Bi_{0.5}Na_{0.5}ZrO₃ ceramic with Li⁺ doping at 0.03 mol.% exhibit a highest the dielectric constant at room temperature (ϵ_R ~1300), ϵ_C (~5,000) and large d_{33} (~252 pC/N) (17). On the other hand, various kinds of doping would produce sophisticated influences on the phase evolution, microstructure and electrical behaviors of ceramics, since they have a different valence, ionic size, and doping sites (20). The different valence of the doping ions (acceptor or donor doping) creates of oxygen vacancies and sophisticated flaws, resulting to pinned ferroelectric domain walls and worsening in electrical behaviors of samples (21). Hence, inspection the effects of the ionic size on the phase structure, microstructure and electrical behaviors for the lead-free ceramics without the influence of valence fluctuation is very compelling. In this work, Cs⁺ and Li⁺ are appraised because of its ionic radius (Cs⁺~1.88 Å) larger and (Li⁺~1.15 Å) smaller than the ionic radius of both K⁺ (~1.64 Å) and Na⁺ (~1.39 Å) (16).

So, in this present work, we study the influence of Cs⁺ and Li⁺ substitutional [(K_{0.5-x}Cs_xNa_{0.5}Nb_{0.7}Ta_{0.3}O₃) and (K_{0.5}Na_{0.5-x}Li_xNb_{0.7}Ta_{0.3}O₃)] and additional

[($K_{0.5}Na_{0.5}Nb_{0.7}Ta_{0.3}O_3$ -xmol%Cs) and ($K_{0.5}Na_{0.5}Nb_{0.7}Ta_{0.3}O_3$ -xmol.%Li)] doping (x=0, 0.01, 0.02, 0.03 and 0.04 mol.%) on the crystalline phases, microstructure and electrical behaviors of $K_{0.5}Na_{0.5}Nb_{0.7}Ta_{0.3}O_3$ ceramics synthesized by the solid-state combustion technique.

Research objectives

1. To study the preparation ($K_{0.5}Na_{0.5})(Nb_{0.7}Ta_{0.3})O_3$ ceramics with various firing conditions using the solid-state combustion method.
2. To study the preparation ($K_{0.5}Na_{0.5})(Nb_{0.7}Ta_{0.3})O_3$ ceramics with Cs^+ and Li^+ substitutional and additional doping using the solid-state combustion technique.
3. To inspect the influences of calcination and sintering temperatures on the phase structure, microstructure and electrical properties of ($K_{0.5}Na_{0.5})(Nb_{0.7}Ta_{0.3})O_3$ ceramics.
4. To inspect the effects of Li^+ and Cs^+ substitutional and additional doping on the phase structure, microstructure and electrical properties of ($K_{0.5}Na_{0.5})(Nb_{0.7}Ta_{0.3})O_3$ ceramics.
5. To inspect the correlation between phase structure, microstructure and electrical properties of ($K_{0.5}Na_{0.5})(Nb_{0.7}Ta_{0.3})O_3$ ceramics with Cs^+ and Li^+ substitutional and additional doping.

Research expected outputs

1. To comprehend the preparation of ($K_{0.5}Na_{0.5})(Nb_{0.7}Ta_{0.3})O_3$ ceramics with various firing conditions using the solid-state combustion method.
2. To comprehend the preparation of ($K_{0.5}Na_{0.5})(Nb_{0.7}Ta_{0.3})O_3$ ceramics with Cs^+ and Li^+ substitutional and additional doping using the solid-state combustion technique.
3. To comprehend the influences of calcination and sintering temperatures on the phase structure, microstructure and electrical properties of ($K_{0.5}Na_{0.5})(Nb_{0.7}Ta_{0.3})O_3$ ceramics.
4. To comprehend the effects of Li^+ and Cs^+ substitutional and additional doping on the phase structure, microstructure and electrical properties of ($K_{0.5}Na_{0.5})(Nb_{0.7}Ta_{0.3})O_3$ ceramics.

5. To comprehend the correlation between phase structure, microstructure and electrical properties of $(\text{K}_{0.5}\text{Na}_{0.5})(\text{Nb}_{0.7}\text{Ta}_{0.3})\text{O}_3$ ceramics with Cs^+ and Li^+ substitutional and additional doping.

Research scope

1. The $(\text{K}_{0.5}\text{Na}_{0.5})(\text{Nb}_{0.7}\text{Ta}_{0.3})\text{O}_3$ powder and ceramics were synthesized by the solid-state combustion method. All samples were calcined at 600, 650, 700, 750 and 800°C for 2 h and sintered at 1150, 1160, 1170, 1180 and 1190°C for 2-5 h, respectively.
2. The $(\text{K}_{0.5}\text{Na}_{0.5})(\text{Nb}_{0.7}\text{Ta}_{0.3})\text{O}_3$ samples with Cs^+ substitutional [$(\text{K}_{0.5-x}\text{Cs}_x\text{Na}_{0.5})(\text{Nb}_{0.7}\text{Ta}_{0.3})\text{O}_3$; $\text{K}_{0.5-x}\text{Cs}_x\text{NNT}$] and additional [$(\text{K}_{0.5}\text{Na}_{0.5})(\text{Nb}_{0.7}\text{Ta}_{0.3})\text{O}_3-x\text{Cs}_2\text{CO}_3$; $\text{KNNT}-x\text{Cs}$] doping ($x=0, 0.01, 0.02, 0.03$ and 0.04 mol.%) were fabricated by the solid-state combustion method at calcination temperature of 600°C for 2 h and sintering temperatures of 1130-1150°C for 4 h, respectively.
3. The $(\text{K}_{0.5}\text{Na}_{0.5})(\text{Nb}_{0.7}\text{Ta}_{0.3})\text{O}_3$ samples with Li^+ substitutional [$(\text{K}_{0.5}\text{Na}_{0.5-x}\text{Li}_x)(\text{Nb}_{0.7}\text{Ta}_{0.3})\text{O}_3$; $\text{KN}_{0.5-x}\text{Li}_x\text{NT}$] and additional [$(\text{K}_{0.5}\text{Na}_{0.5})(\text{Nb}_{0.7}\text{Ta}_{0.3})\text{O}_3-x\text{Li}_2\text{CO}_3$; $\text{KNNT}-x\text{Li}$] doping ($x=0, 0.01, 0.02, 0.03$ and 0.04 mol.%) were fabricated by the solid-state combustion method at calcination temperature of 600°C for 2 h and sintering temperatures of 1150°C for 4 h.
4. Inspection of the densification by Archimedes method, phase formation by X-ray diffraction (XRD) and Rietveld refinement method, morphology by scanning electron microscopy (SEM) and transmission electron microscopy (TEM), average grain size by linear intercept method, dielectric properties by an inductance capacitance resistance (LCR) meter and ferroelectric hysteresis (P - E) loops by a computer-controlled modified Sawyer-Tower circuit.

CHAPTER II

RELATED THEORY AND LITERATURE REVIEW

Fundamental theory

Perovskite Structure

In the year 1839, the first mineral (CaTiO_3) with perovskite structure was discovered by Russian mineralogist (Count Lev Alexevich von Perovski) in the Ural Mountains (22-24). The name perovskite represented any compound, which it has the general stoichiometry ABC_3 where an octahedron of C ions surrounded the B ion. The perovskite family consist various types of oxides such as transition metal oxides with the formula ABO_3 . In the ideal ABO_3 formula, A ion is an alkali earth metals or lanthanides with a larger radius, B is a transition metal ion with a small radius, and O is the oxygen ion. Largely, A cations are 1+ or 2+ of charges such as K^+ , Na^+ , Li^+ or Cs^+ and B cations are 4+ or 5+ of charges such as Ti^{4+} , Sn^{4+} , Nb^{5+} or Ta^{5+} . For the cubic unit cell of ABO_3 perovskite structure, atom A is occupied at the body center, atom B is occupied at the cube corner position, and oxygen atoms are occupied at the face-centered position, as presented in Figure 1. The 12-fold coordination of A cation and the 6-fold coordination of the B cation (octahedron) cause the stabilization of the perovskite lattice. The ideal perovskite structure was explained by Hines et al. as corner linked BO_6 octahedra with interstitial A cations (22-30). In the ideal cubic model of perovskite, some distortions can result in orthorhombic, rhombohedral, and hexagonal forms (Figure 1.) (30). Figure 2 display Geometric characteristics of the 7 crystal systems and 14 Bravais lattices. The difference of the 7 crystal systems was determined by the lengths of the unit cell edges (a , b and c) and the angles between the edges (α , β and γ), which collectively known as the lattice parameters (Figure 2.). Nowadays, the perovskite structure has been studied extremely (31-35). Some examples of ceramics with perovskite structure are lead titanate (PbTiO_3), lead zirconate titanate ($\text{PbZr}_{1-x}\text{Ti}_x\text{O}_3$), potassium niobate (KNbO_3), potassium sodium niobite-based ($\text{K}_{1-x}\text{Na}_x\text{NbO}_3$), bismuth sodium titanate-based ($\text{Bi}_{1-x}\text{Na}_x\text{TiO}_3$), barium titanate (BaTiO_3) and so on.

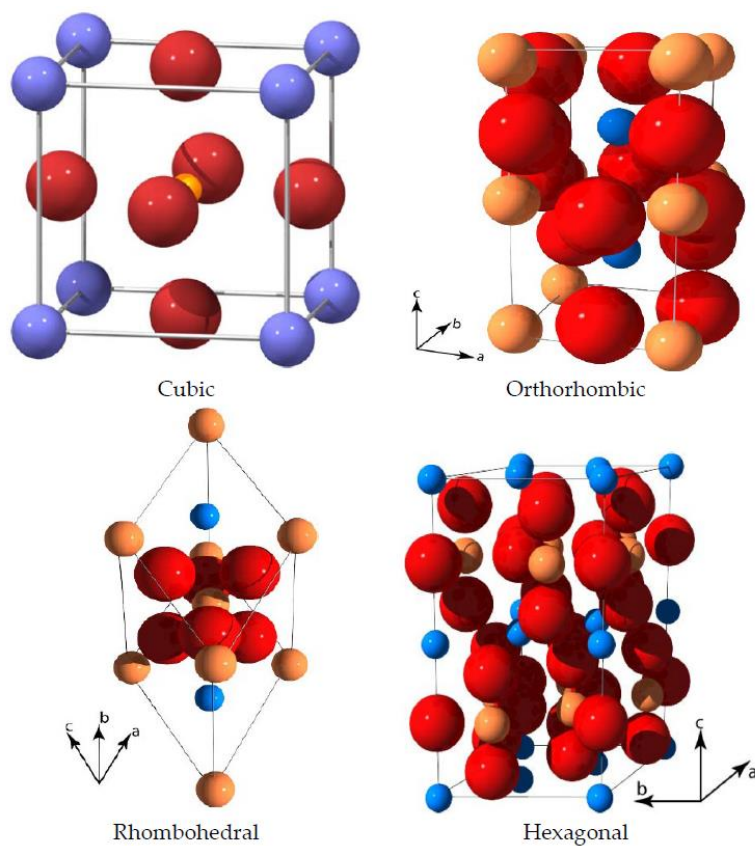


Figure 1 Various types perovskite unit cells. Blue spheres refer to the A cations, yellow spheres refer to the B cations and red spheres refer to oxygen anions forming an octahedra.

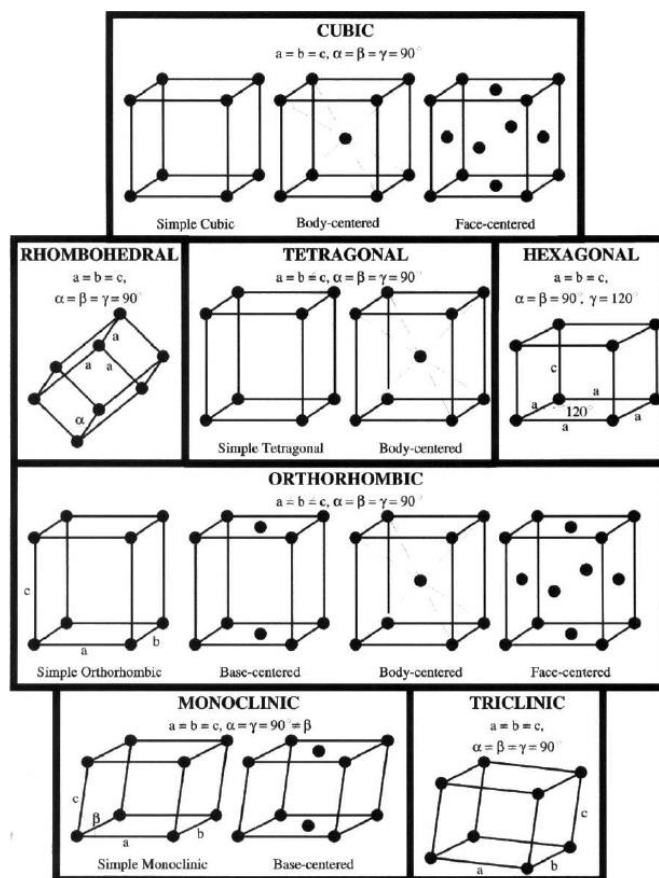


Figure 2 Geometric characteristics of the 7 crystal systems and 14 Bravais lattices.

Ceramic Microstructures

The both of single crystals and polycrystalline solids contain in crystalline solids. A single crystal is a solid in which the periodic and repeated alignment of atoms is excellent and broadens during the entirety of the samples continuous. A polycrystalline solid is included of a bevy of plenty single crystals, called grains, separated from one another by regions of disorder called grain boundaries, as represented in Figure 3. Normally, in ceramics the grains are in the range of 1 to 50 μm and only can be seen under a microscope (35). The microstructure is defined by the shape and size of the grains, existence of porosity, second phases, and other properties, as well as their distribution. Many of the characteristics of ceramics are influenced by their microstructure.

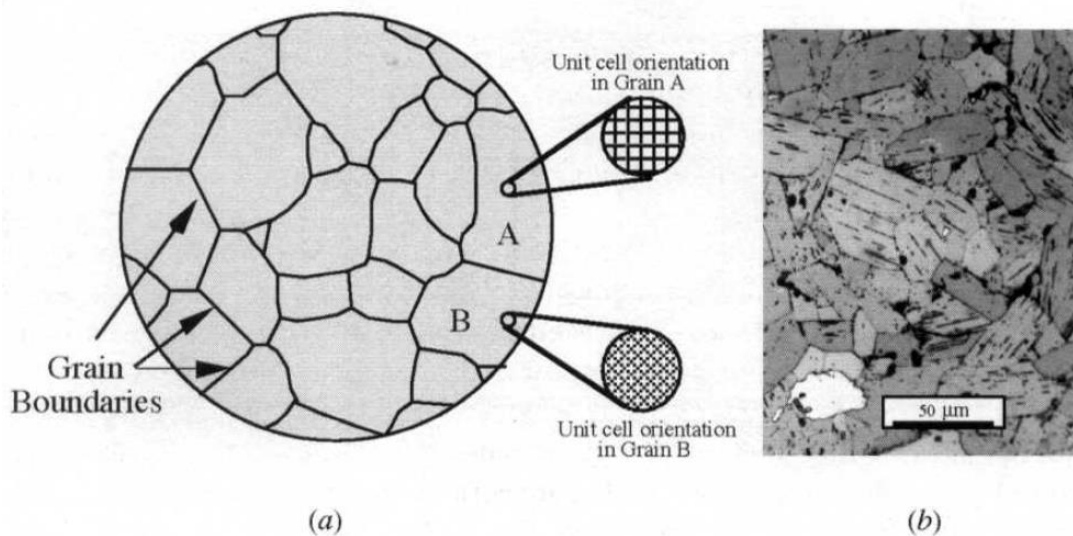


Figure 3 (a) Diagram of a polycrystalline specimen. A polycrystal is consist of numerous grains separated from one another by areas of disorder called grain boundaries and (b) Normal microstructure as seen via an optical microscope.

Ferroelectricity

Ferroelectricity is a phenomenon illustrate by crystals with a spontaneous polarization and hysteresis effects associated with dielectric changes when an electric field is given (36-38). In the year 1921, the ferroelectricity was first discovered in single-crystal materials of Rochelle salt. After that, throughout the early to mid-1940, its subsequent expansion into the scope of polycrystalline ceramics (i.e., barium titanate, BaTiO_3). There has been a continuous succession of new materials and technology developments, leading to a significant number of industrial and commercial applications as such high-dielectric-constant capacitors, piezoelectric sonar and ultrasonic transducers, radio and communication filters, pyroelectric security surveillance devices, medical diagnostic transducers, stereo tweeters, buzzers, gas ignitors, positive temperature coefficient (PTC) sensors and switches, ultrasonic motors, electro-optic light valves, thin-film capacitors and FE thin-film memories, etc. (36-38)

Hysteresis Loop

In basis, every ferroelectric material has own characteristic hysteresis loop, just like a fingerprint. The hysteresis loops can be used to identify the ferroelectricity directly. Figure 4 illustrates a typical ferroelectric hysteresis loop of material. Peculiarity parameters can be prescribed, such as spontaneous polarization (P_s), remnant polarization (P_r) and coercive field (E_C). The grains in polycrystalline materials are often divided into several domains, owing to the necessity of the energy minima. At first, the domain directions are distributed randomly in such a way that they cause zero net macroscopic polarization (O point). Next, when the external field is greater than the E_C , the polycrystalline ferroelectric material may be brought into a polar state (A point). Then, a macroscopic polarization is slowly induced by rising the electric field strength, as seen in Figure 4. Next, the harsh change in the polarization in the neighborhood of E_C can be described by the polarization reversal (domain switching) (B point), while at high field end, the polarization is saturated and the material functions as a linear dielectric (C point). After that, some domains will back-switch as the electric field strength begins to reduce, but at zero field the net polarization is nonzero, come up with the remaining polarization P_r (D point). To achieve zero polarization, an electric field of the opposite direction is necessary in the last stage. This field strength is called the coercive field (or coercivity) (F point). The rising of this opposite field strength, causing a similar rearrangement of the polarization is founded in the negative field part (G point). The spontaneous polarization of the ferroelectric materials P_s may be evaluated by intercepting the polarization axis with the foresee linear section, as shown in Figure 4. Furthermore, the ferroelectrics ordinarily have ferroelastic domains (unless for LiNbO_3 , which only has 180° ferroelectric domains), spontaneous strain is also created with the external electric field concurrently (38). Thus, if the strain is inspected as well as the polarization, a strain-electric field curve, like “butterfly”, can be seen.

For perfect ferroelectric system, the ferroelectric hysteresis loops should be symmetric features. The positive and negative P_r and E_C values are equal. Whereas, the shape of the ferroelectric hysteresis loops in fact may be possible many factors, such as thickness of the samples, material composition, thermal treatment, existence

of the charged flaws, mechanical stresses, measurement conditions and others. Their effect on the material properties may be well expressed through the loops.

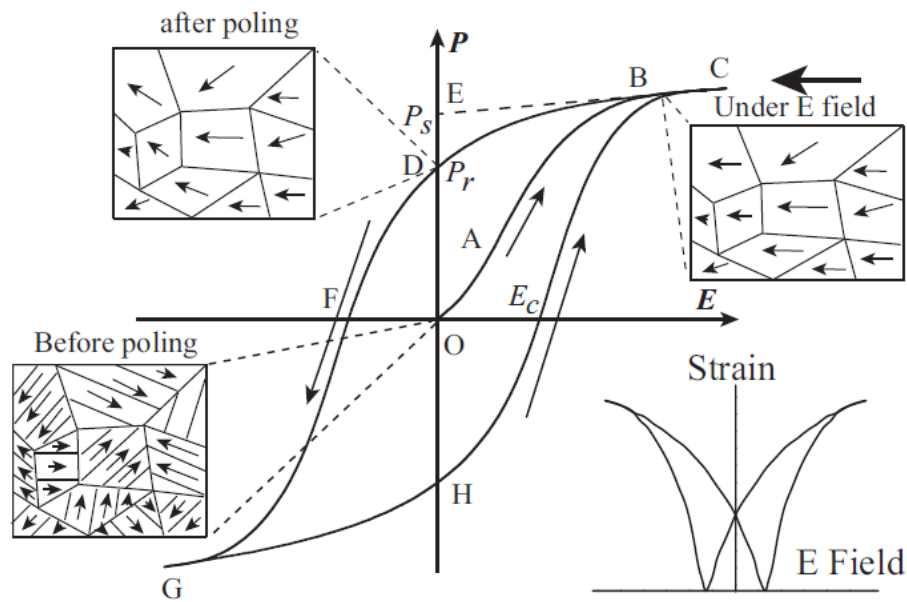


Figure 4 A normal hysteresis loop in ferroelectrics, including domain reversal (polarization rotation) and strain-electric field curve.

Dielectric properties

Dielectric material will not conduct electricity and are critical importance on applied as capacitor in electronic devices (e. g., sensors, actuators, ultrasound transducers, etc.) and as insulators. The ceramic materials had very high charge-storing capabilities, i.e., relative dielectric constants $k' > 1000$.

In contrast to electrical conductivity, which relate to long-rang motion of charge carriers, the dielectric response comes from the short-rang motion of these carriers under the effect of an externally applied electric field. Because all solids consist of positive and negative identity, the application of an electric field to any solid will lead to a separation of its charges. This charge separation is called polarization.

Dielectric properties can vary widely among solids and are a function of temperature, frequency of applied field, moisture, crystal structure, and other external

factors. Additionally, the response can be either linear or nonlinear. This section examines linear dielectrics including the influence of temperature and frequency on the dielectric response.

Basic Theory

Prior to discuss the ferro dielectric polarization, it is important to understand how one measures polarization and to obtain a qualitative understanding of how polarization occurs is difficult or easy. Consider two metal parallel plates of area A separated by a distance d in vacuum, (Figure 5 (a)). These plates are connected to the basic electric circuit, seen in Figure 5 (a), and closing the circuit leads to a transient surge of current, which swiftly decays to zero, as represented in Figure 5 (b). Given that the area under the I against t curve is the total charge that flows through the circuit and now stored on the capacitor plates, following the formula (1):

$$Q = \int I dt \quad (1)$$

Repeating the experiment at different voltages V and plotting Q against V should give a straight line, as seen in Figure 6. The slope of the Q against V curve is the capacitance C_{vac} of the parallel plates in vacuum, which was described below by the following formula (2):

$$Q = CV \quad (2)$$

$$C_{vac} = \frac{\epsilon_0 A}{d} \quad (3)$$

Where ϵ_0 is the permittivity of free space, which is a constant ($8.85 \times 10^{-2} \text{ C}^2/\text{J.m}$).

The units of capacitance are farads (F), where $1 F = 1 \text{ C/V} = 1 \text{ C}^2/\text{J}$.

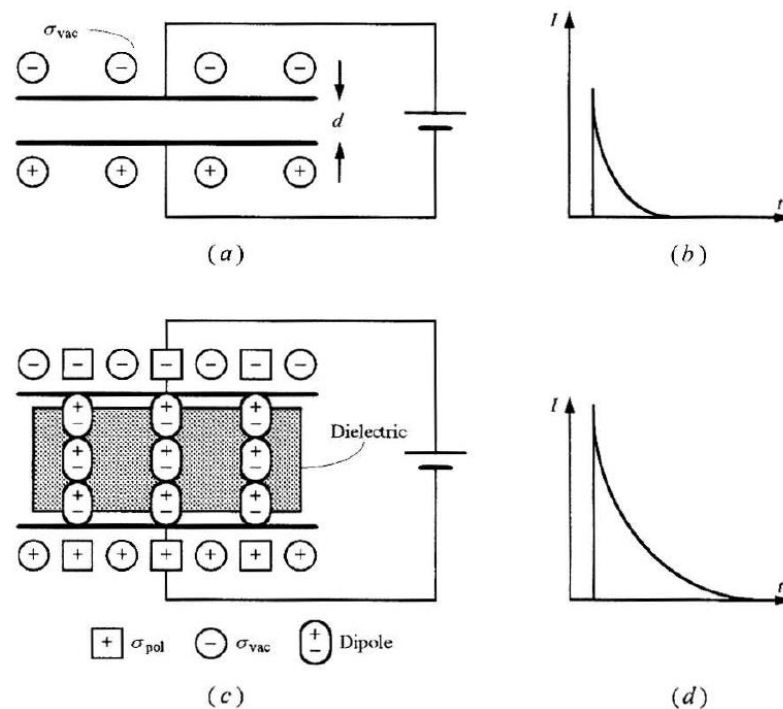


Figure 5 (a) Parallel-plate capacitor of area A and separation d in vacuum connect with DC power source. (b) Closing of the circuit results in a transient surge of current to flow through the circuit. Charge collected on the capacitor is equal to the area under the curve. (c) Same as (a) except, now a dielectric is placed between the plates. (d) Closing of the circuit caused a charge retained on the parallel plates, which has to be greater than that stored in (b).

If a dielectric (which can be a gas, solid, or liquid) is introduced between the plates of the capacitor (Figure 5 (c)) and the aforementioned experiment is repeated, the current that flows through the external circuit and is stored on the capacitor plates will rise (Figure 5 (d)). Repeating the experiment at different voltages and plotting the total charge stored on the capacitor versus the voltage applied will again result in a straight line but with a larger slope than that for vacuum (Figure 5). In other words, equation (3) is now modified to read

$$C = \frac{\epsilon A}{d} \quad (4)$$

Where ϵ is the dielectric constant of the material between the plates. The relative dielectric constant of a material k' is defined as

$$k' = \frac{\epsilon}{\epsilon_0} \quad (5)$$

Since ϵ is always greater than ϵ_0 , the minimum value for k' is 1. By combining equation (4) and (5), the capacitance of the metal plates separated by the dielectric is

$$C = \frac{k'\epsilon_0 A}{d} = k'C_{vac} \quad (6)$$

Thus k' is a dimensionless parameter that compares the charge-storing capacity of a material to that of vacuum.

The foregoing discussion can be summarized as follows: when a voltage is applied to a parallel-plate capacitor in vacuum, the capacitor will retain charge. In the presence of a dielectric, an additional “something” happens within that dielectric which allows the capacitor to retain more charge (35).

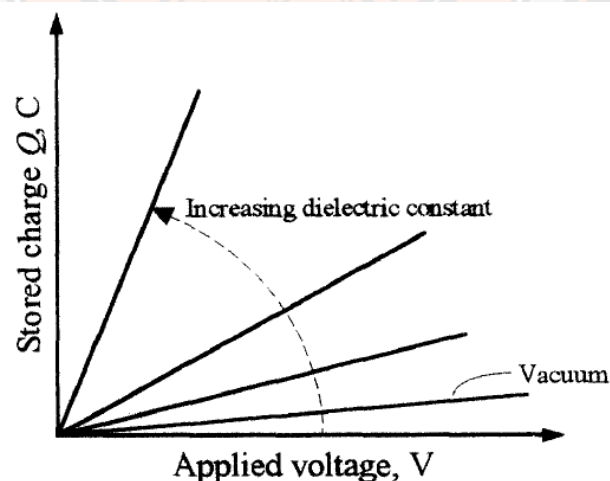


Figure 6 Functional dependence of Q on applied voltage. Slope of curve is associated to the dielectric constant of the materials.

Sintering

Sintering is the procedure by which a powder compact is changed to an athletic, dense ceramic body upon heating. In an alternate explanation given by Herring sintering is to mean any changes in shape which a tiny particle or a cluster of particles of uniform composition undergoes when maintained at high temperature. It can also be said that the sintering mean elimination of pores between particles along with shrinkage (densification) and grain growth (35, 39).

The decline of surplus energy associated with surfaces is the macroscopic driving factor at work during sintering. This can occur by (1) decline of the overall surface area owing to a rise in particles average size, resulting in coarsening (Figure 7 (b)), and/or (2) the removal of solid/vapor interfaces and the formation of grain boundary area, followed by grain growth, resulting in densification (Figure 7 (a)). These two processes are commonly in jousting. If the atomic mechanisms that cause densification dominate, the pores get decrease and eventually vanish and the compact shrinks. However, if the atomic mechanisms that lead to coarsening are quicker, the pores and grains will grow with time.

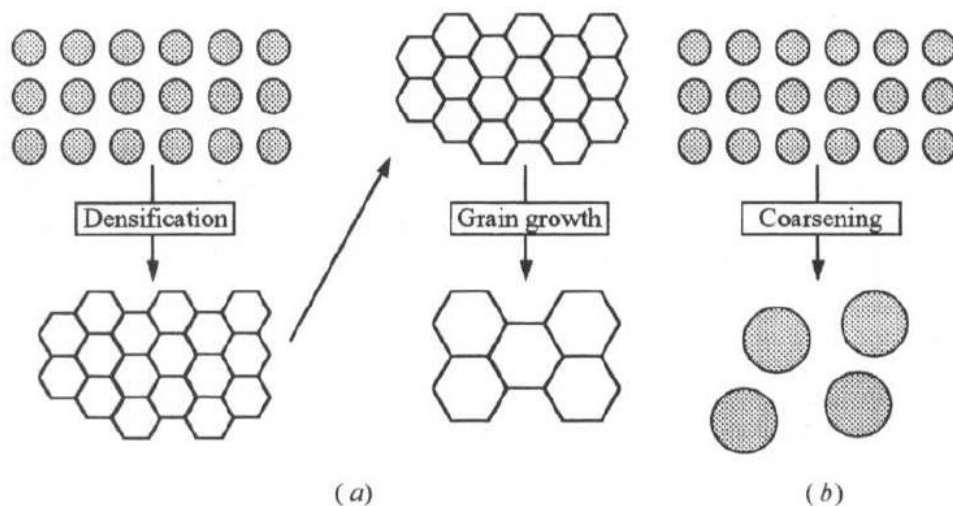


Figure 7 Schematic of two possible paths by which a collection of particles can lower its energy. (a) Densification followed by grain growth. In this case shrinkage of the compact has to happen (b) Coarsening where the large grains grow at the expense of the smaller ones.

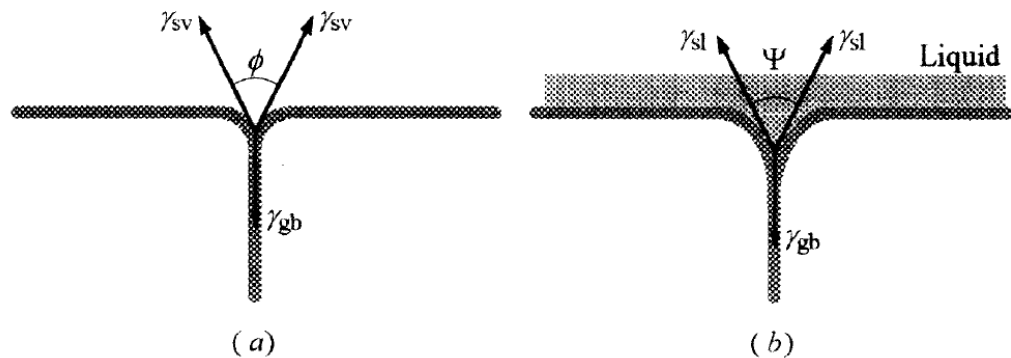


Figure 8 (a) Equilibrium dihedral angle between grain boundary and solid/vapor interfaces, (b) Equilibrium dihedral angle between grain boundary and liquid phase.

An essential condition for densification to arise is that the grain boundary energy γ_{gb} be less than twice the solid/vapor surface energy γ_{sv} . This indicates that the equilibrium dihedral angle ϕ seen in Figure 8 (a) and defined as has to be less than 180° . For numerous oxide systems, the dihedral angle is $\sim 120^\circ$, suggesting that $\gamma_{gb} / \gamma_{sv} \approx 1.0$, as opposed to metallic systems where that ratio is near to between 0.25 and 0.5 (35, 40).

$$\gamma_{gb} = 2\gamma_{sv} \cos \frac{\phi}{2} \quad (7)$$

Sintering stages

Coble explained a sintering phase as an “interval of geometric change in which pore shape is totally assign (such as rounding of necks during the initial phase sintering) or an interval of time during which the pore remains constant in shape while declining in size.” Based on that definition, three phases have been classified: an initial, an intermediate, and a final phase. During the initial phase, the interparticle contact area rises from 0 to ~ 0.2 by neck development (Figure 9 (b)), and the relative density rises from about 60 to 65%. The intermediate phase is unique by continuous pore channels that are coincident with three-grain edges (Figure 9 (c)). During this

stage, the relative density increases from 65 to about 90% by having matter diffuse toward, and vacancies aloof from the long cylindrical channels. The final phase begins when the pore phase is ultimately squeezed off and is unique by the absence of a continuous pore channel (Figure 9 (d)). Individual pores are either of lenticular shape, if they reside on the grain boundaries, or rounded, if they reside within a grain. A significant feature of this phase is the rise in mobilities of pore and grain boundary, which must be regulated if the theoretical density is to be acquire (41).

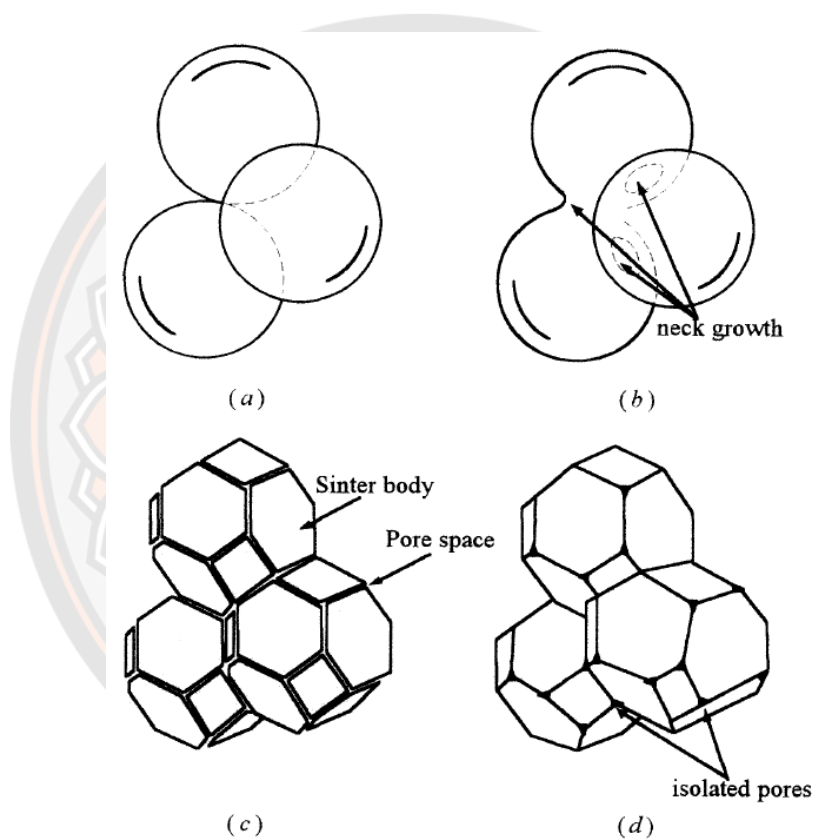


Figure 9 (a) The spheres in tangential contact indicate the initial phase of the sintering model, (b) The spheres have begun to form as the initial phase draws to a close, (c) Intermediate phase; grains adopted shape of dodecahedra, enclosing pore channels at grain boundary, (d) Pores are tetrahedral inclusions in the corners where four dodecahedra converge in the final phase.

A literature reviews

The advancement of piezoelectric materials has resulted in a broad range of applications from regular use to more specialized devices such as sensors, actuators, ultrasound transducers, medical devices, etc (42-45). The perovskite ferroelectric materials are widely recognized for their remarkable piezoelectricity. In 1954, Jaffe B et al. discovered lead-based $\text{Pb}(\text{Zr},\text{Ti})\text{O}_3$ (PZT) piezoelectric ceramics and have been extensively used owing to their large piezoelectric coefficient ($d_{33}\sim 200\text{-}750\text{ pC/N}$) and high Curie temperature ($T_C\sim 180\text{-}320^\circ\text{C}$) (1-4, 45). Unfortunately, lead-based materials are banned by global laws and regulations because of their high toxicity causing a great threat to environmental and human health. Hence, scientists have concentrated their tremendous efforts on the development of lead-free replacements.

Potassium Sodium Niobate; $[(\text{K}, \text{Na}) \text{NbO}_3]$ (KNN) ceramics

Since entering the 21st century, the lead-free KNaNbO_3 perovskite ceramics has become one of the most widely inspected piezoelectric systems because of its large d_{33} and high T_C . KNN solid solution is formed by potassium niobate (KNbO_3) ferroelectric compound having space group a $Cm2m$ and sodium niobate (NaNbO_3) antiferroelectric compound having space group a $Pbma$ with an orthorhombic perovskite phase at room temperature (46-48). Figure 10 displays the single orthorhombic structure at room temperature of KNN ceramics. The composition around $x=0.5$ is of great attention owing to the superior ferroelectric and piezoelectric behaviors. The $\text{K}_{0.5}\text{Na}_{0.5}\text{NbO}_3$ (KNN) ceramic undergoes three phase transitions, from rhombohedral to orthorhombic (T_{R-O}) around -110°C , orthorhombic to tetragonal (T_{O-T}) around 180°C , and tetragonal to cubic (T_{T-C}) around 400°C , as seen in Figure 11. However, the main drawbacks of this ceramic can be attributed to two main factors. First, according to the phase diagram of $\text{KNbO}_3\text{-NaNbO}_3$ (Figure 12), the KNN ceramic is decomposed beyond 1140°C (49). Thus, the high sintering temperature is not appreciated. Second is evaporation of alkali elements (K and Na) at high temperature which makes it is difficult to maintain the proper chemical stoichiometry and obtain high dense of ceramics (50-52).

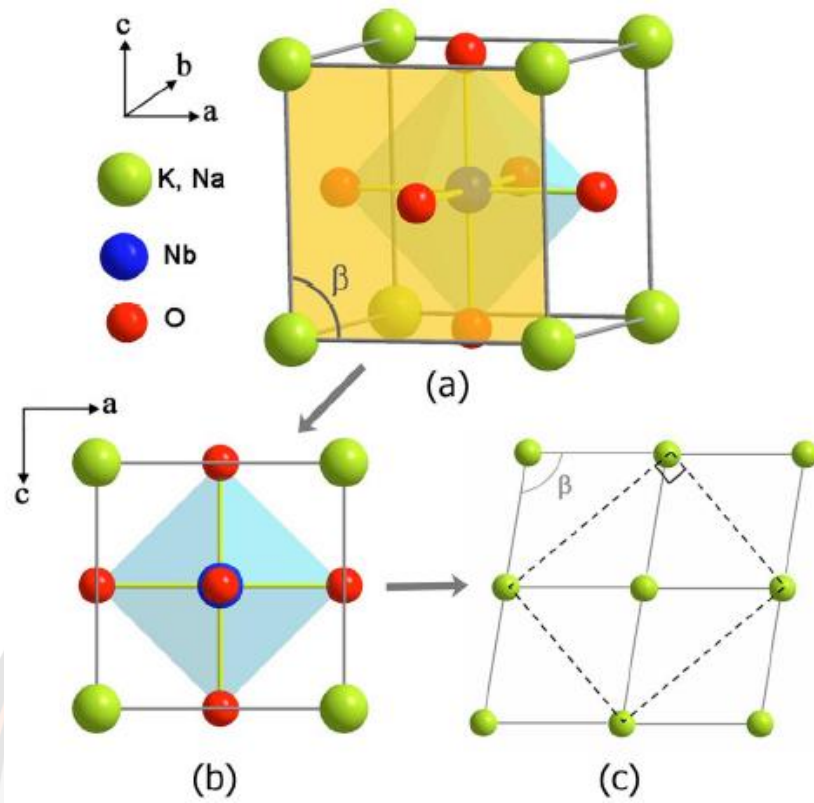


Figure 10 Orthorhombic perovskite structure of KNN ceramic at room temperature.

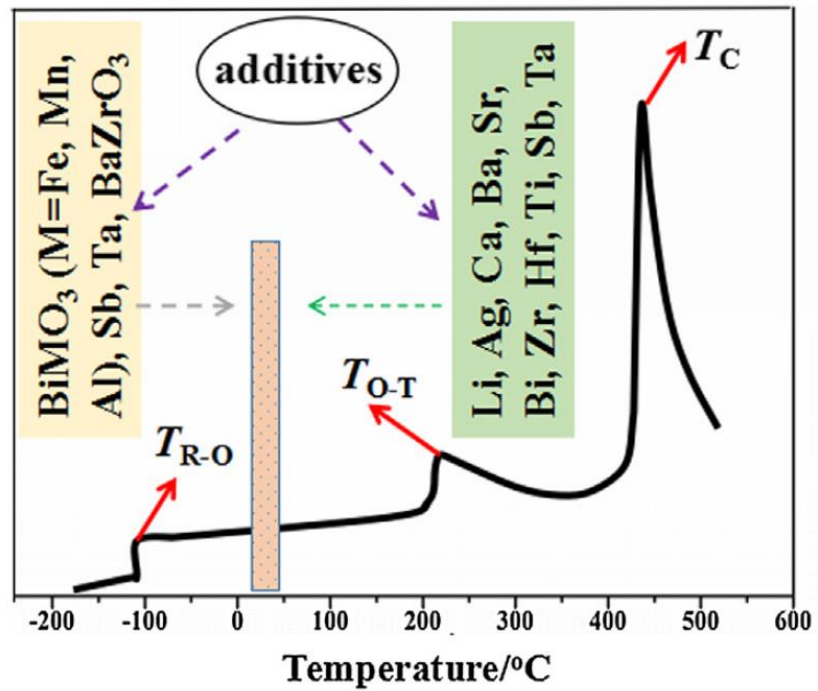


Figure 11 The phase transitions of KNN ceramics.

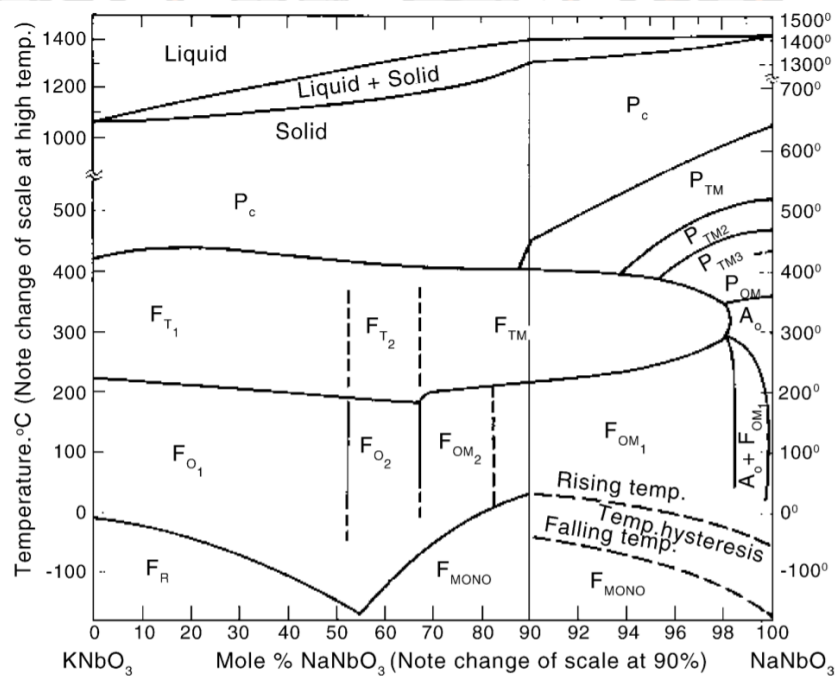


Figure 12 The binary phase diagram of KNbO₃-NaNbO₃.

$(\text{K}_{0.5}\text{Na}_{0.5})(\text{Nb}_{1-x}\text{Ta}_x)\text{O}_3$ (KNNT) ceramics

In 2009, Y.G. Lv et al. (10) prepared $(\text{K}_{0.5}\text{Na}_{0.5})(\text{Nb}_{1-x}\text{Ta}_x)\text{O}_3$ (KNNT) ceramics with $x=0, 0.10, 0.15, 0.20, 0.25$ and 0.30 mol.% using the solid-state reaction method (calcination temperature of 900°C for 5 h and a sintering temperature of $1090\text{-}1180^\circ\text{C}$ for 2 h). The XRD data of the all ceramics showed pure perovskite structure with single orthorhombic phase, as is demonstrated in Figure 13. This implies that Ta is completely diffuse into B-site in the KNNT lattice. SEM image of the KNNT ceramics with different x are indicated in Figure 14 (a-f). The grains of all the ceramics showed quadrate shape. The average grain size of KNN ceramic was about $> 5 \mu\text{m}$, and all the KNNT ceramics have smaller grain sizes than the pure KNN system. The typically temperature dependence of dielectric constant of the KNNT ceramics ($x=0, 0.15$ and 0.30 mol.%) at the measuring frequency of 100 kHz over wide temperatures range between 0 and 500°C are shown in Figure 15. All samples showed three phase transition peaks, associate with the rhombohedral ferroelectric-orthorhombic ferroelectric phase transition ($T_{\text{R-O}}$), the orthorhombic ferroelectric-tetragonal ferroelectric phase transition ($T_{\text{O-T}}$) and tetragonal ferroelectric-cubic paraelectric phase transition (T_{C}), respectively (53). They found that the $T_{\text{R-O}}$ gradually shifted to higher temperatures (see inset Figure 15), while the both $T_{\text{O-T}}$ and T_{C} gradually shifted to lower temperatures with the rising x . The dielectric constant (ε_{C}) tends to decreased when the rising x . Table 1 summarize the data of measured density, relative density, dielectric properties and piezoelectric coefficients at room temperature of KNNT ceramics with different x . With $x=0.30$ mol.%, the sample exhibited highest the density ($\rho \sim 4.92 \text{ g/cm}^3$) and d_{33} ($\sim 205 \text{ pC/N}$).

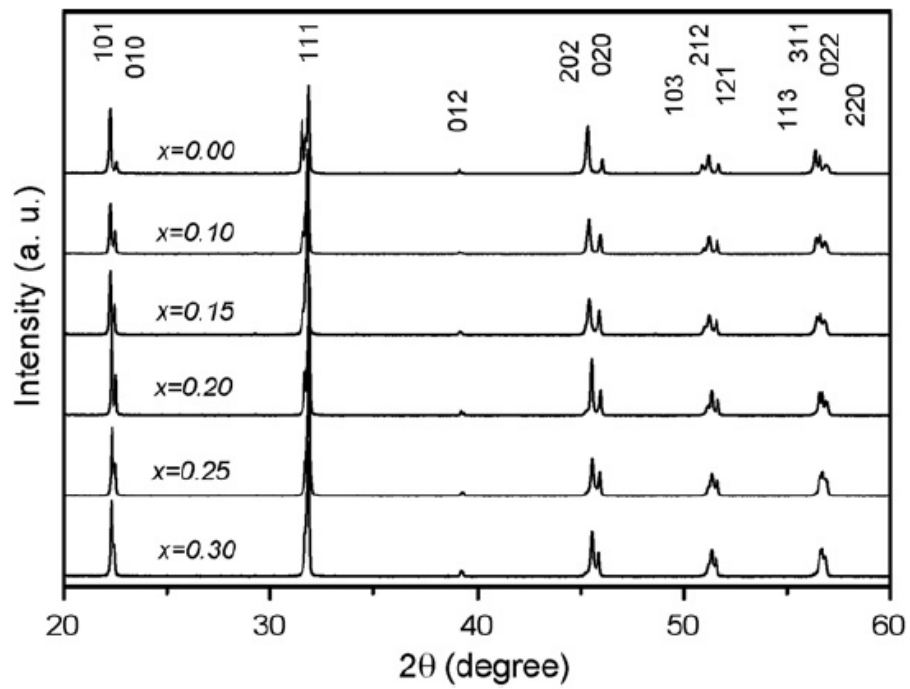


Figure 13 XRD pattern at room temperature of the $\text{K}_{0.5}\text{Na}_{0.5}\text{Nb}_{1-x}\text{Ta}_x\text{O}_3$ ceramics with $x=0-0.30$ mol.%.

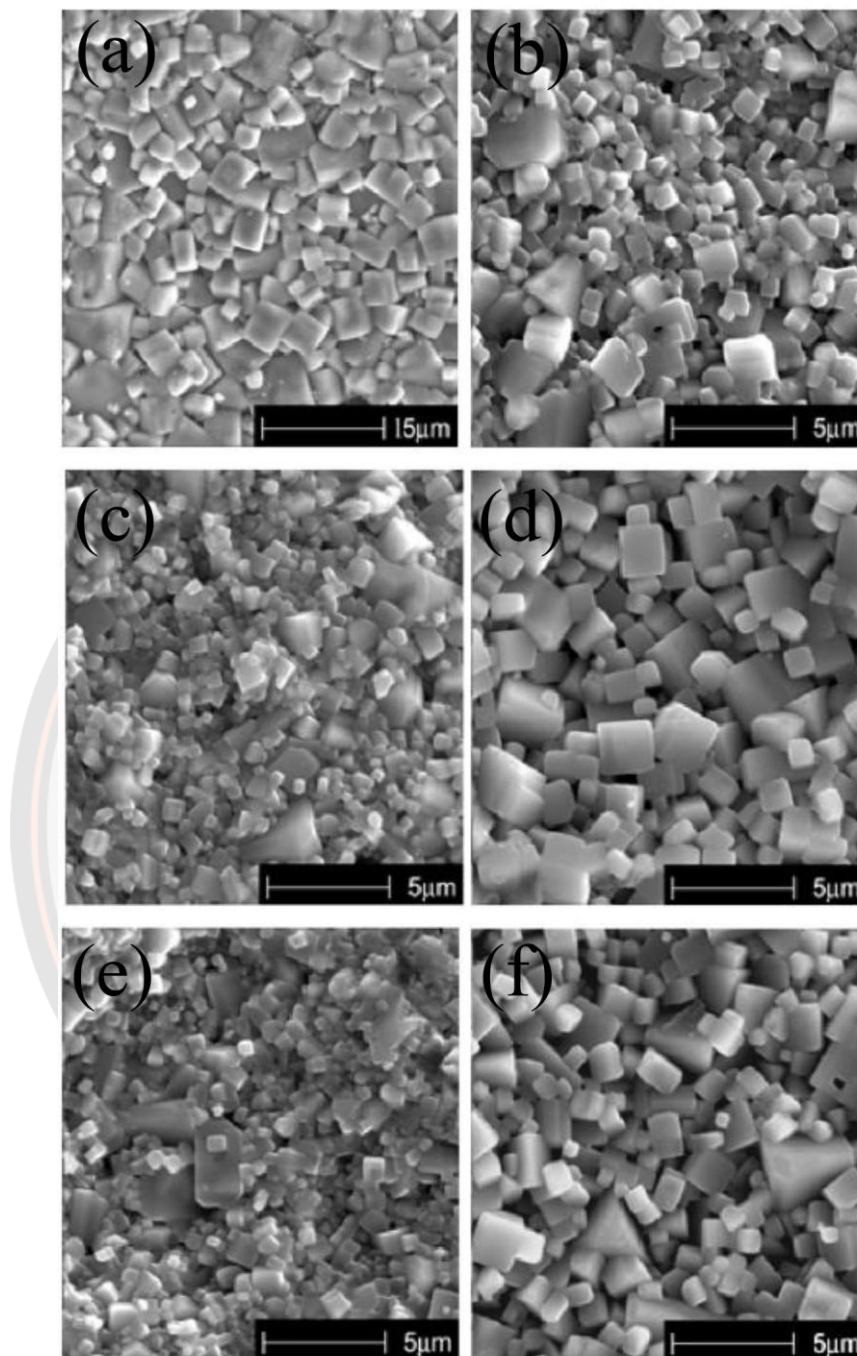


Figure 14 SEM images of $\text{K}_{0.5}\text{Na}_{0.5}\text{Nb}_{1-x}\text{Ta}_x\text{O}_3$ ceramics with different x ; (a) 0.00 mol.%, at 1090°C (b) 0.10 mol.%, at 1110°C , (c) 0.15 mol.%, at 1120°C , (d) 0.20 mol.%, at 1145°C , (e) 0.25 mol.%, at 1150°C and (f) 0.30 mol.%, at 1170°C .

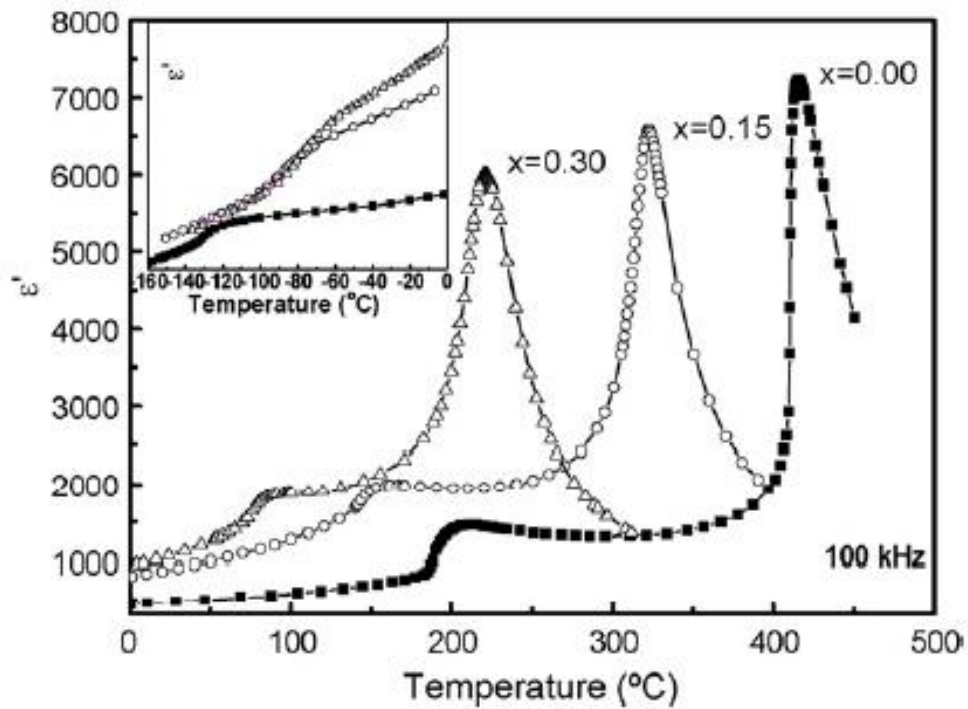


Figure 15 The dielectric constant against temperature of the $K_{0.5}Na_{0.5}Nb_{1-x}Ta_xO_3$ ceramics with various x , measured at 100 kHz.

Table 1 The density values, dielectric properties and piezoelectric coefficient at room temperature of the $K_{0.5}Na_{0.5}Nb_{1-x}Ta_xO_3$ ceramics with different x .

KNNT	x=0.00	x=0.10	x=0.15	x=0.20	x=0.25	x=0.30
ρ (g/cm ³)	4.27	4.44	4.63	4.73	4.86	4.92
ρ (%)	94.21	93.08	95.27	94.04	94.37	94.40
ϵ at 1 kHz	470	507	656	683	889	967
$\tan \delta$ (%)	1.21	1.93	1.92	2.32	2.71	2.53
d_{33} (pC/N)	124	133	151	159	177	205
d_{31} (pC/N)	56	57	65	60	72	81

F. Jean et al. (54) synthesized $(K_{0.5}Na_{0.5})(Nb_{1-x}Ta_x)O_3$ ceramics with $x=0, 0.05, 0.10, 0.20, 0.30, 0.50$ and 1.0 mol.% using the spark plasma sintering method (two calcination temperature of 830°C for 5 h and a sintering temperature of 920°C for 5 h).

980°C for 5-10 min). The evolution of d_{33} of the $\text{K}_{0.5}\text{Na}_{0.5}\text{Nb}_{1-x}\text{Ta}_x\text{O}_3$ ceramics with various x are shown in Figure 16. The d_{33} value tended to increase from ~120 to 160 pC/N upon x increased from 0 to 0.3 mol.% and then dropped.

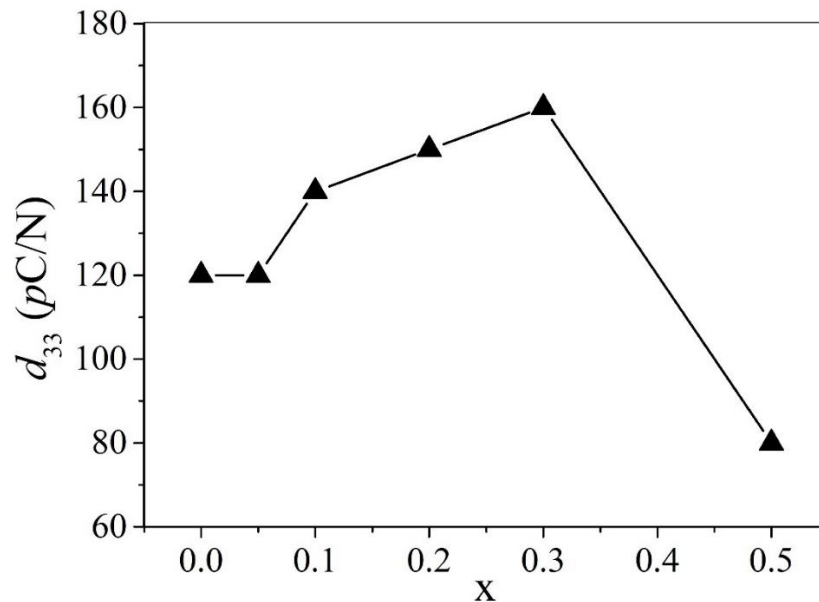


Figure 16 The evolution of d_{33} in $\text{K}_{0.5}\text{Na}_{0.5}\text{Nb}_{1-x}\text{Ta}_x\text{O}_3$ ceramics with different x .

Honghui Gu et al. (55) fabricated KNNT ceramics using the hydrothermal method (sintering temperature of 1160-1200°C for 2 h). Figure 17 depicts the polarization hysteresis (P - E) loops of the KNNT ceramics with different sintering temperature. All compositions exhibited typical and slim P - E loops. The samples showed remnant polarization (P_r) values of 22.91, 19.33, 19.01, 13.64 and 13.00 $\mu\text{C}/\text{cm}^2$ as well as E_C values of 3.7, 4.3, 3.3, 3.4 and 3.5 kV/cm , respectively.

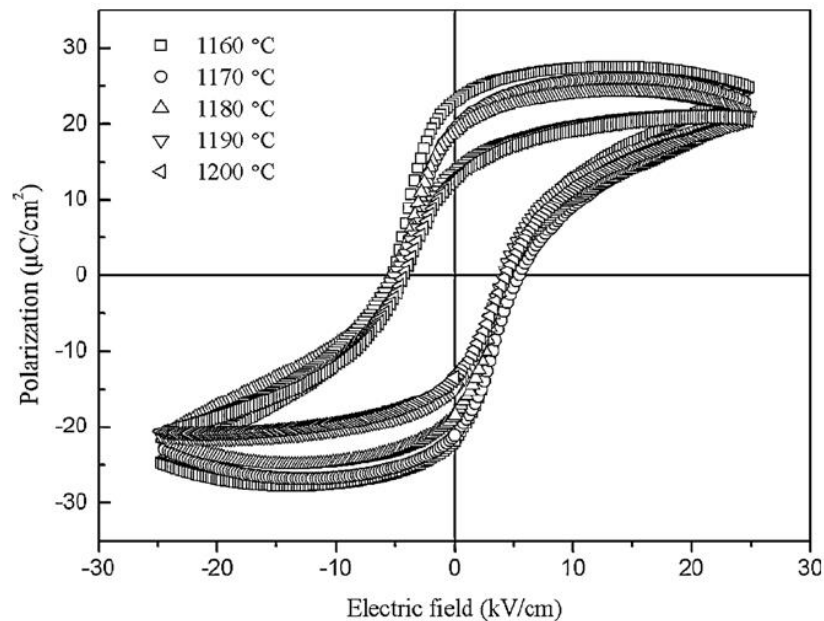


Figure 17 Polarization hysteresis loops of the KNNT ceramics at different sintering temperature.

The improvement in density and electrical properties by additional and/or substitutional doping with elements or compounds in A-site of KNN-based ceramics

1. For the substitutional doping of element or compounds in KNN-based ceramics

Changbai Long et al. (16) prepared $(\text{Na}_{0.5}\text{K}_{0.5})_{1-x}\text{Li}_x\text{NbO}_3$ (KNN-xLi) ceramics with $x=0, 0.055, 0.06, 0.065$ and 0.07 mol.% using the conventional solid-state reaction method (calcination temperature of 800°C for 4 h and a sintering temperature of 1060 and 1100°C for 4 h). The XRD patterns of the KNN-xLi samples with different x are indicated in Figure 18 (a). All samples exhibited a pure perovskite phase and no trace of any secondary phase was identified. For further scrutiny of the phase composition of all samples, enlarged XRD patterns at 2θ around $\sim 31\text{-}47^\circ$ is plotted in Figure 18 (b). According to Figure 18 (b), the intensity of the (220) peak in KNN is much higher than of the (002) one, with $I_{(022)}/I_{(200)}$ value of being around 2, confirming its orthorhombic phase. Moreover, the diffraction peaks of KNN-xLi ceramics shift towards high diffraction angles with the rising x , which pointed out to

shrunk unit cells because of the doping with Li^+ of smaller size [1.15 Å, 12 CN (coordination number)] as compared with those of K^+ (1.64, 12 CN) and Na^+ (1.39 Å, 12 CN) (56, 57). Upon rising x , the (022) peak is suppressed, whereas the relative intensity of the (200) one is increased. In the $x=0.06$ sample, a typical MPB composition can be seen (48, 58). However, further Li^+ substitutional doping inhibited the orthorhombic structure. Tetragonal structure is prominent in the $x=0.07$ sample.

In validate and perfect the XRD studies, Rietveld refinement was done on the samples at $x=0.06$ and 0.07 using the Fullprof software (59, 60). The orthorhombic (space group $Amm2$) and tetragonal (space group $P4mm$) phases of KNbO_3 were selected as the starting models (61). Investigation from Figure 19 (a-b), for each sample, the refined profile well fits to the experimental data. Table 2. lists the reliability factors, lattice parameters and phase percentage of these two compositions. It was found that the calculated quality of the fits was $R_p \leq 0.0384\%$, $R_{wp} \leq 0.0522\%$ and $\chi^2 \leq 1.476$ (Table 2). With $x=0.06$, the sample had a typical two-phase co-existence composition, where the proportions of orthorhombic phase and tetragonal phase are 58.37% and 41.63%. Upon increasing x , the proportions of orthorhombic:tetragonal phases showed an decline of the orthorhombic phase while the tetragonal phase increased.

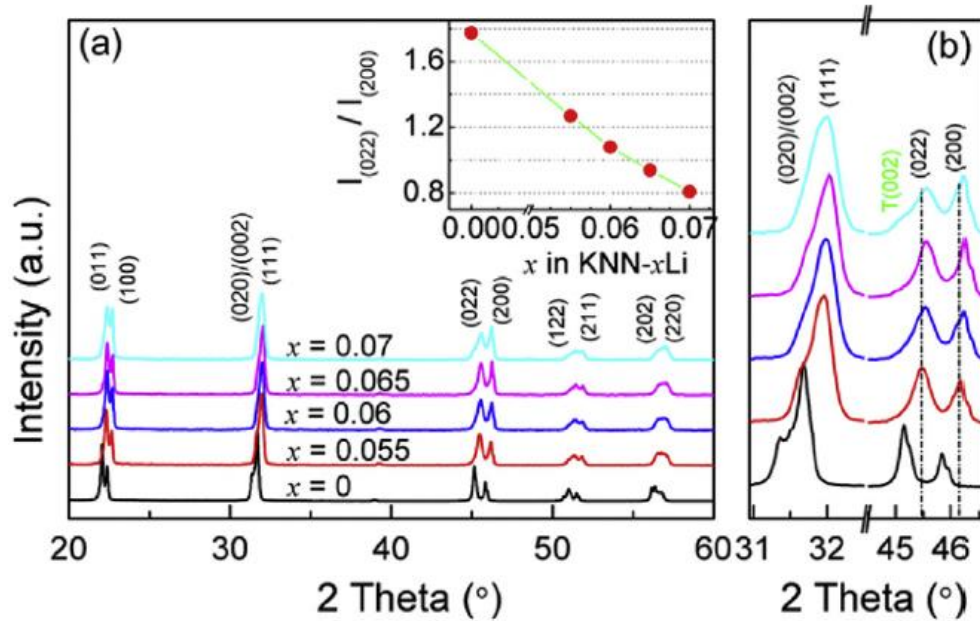


Figure 18 XRD patterns at room temperature of the KNN-xLi ceramics in the 2θ (a) $20\text{-}60^\circ$ and (b) $31\text{-}47^\circ$, and the $I_{(022)}/I_{(200)}$ ratios of all samples as an inset in (a).

Figure 20 (a-e) shows the microstructure of the KNN-xLi samples with different x. The grain of ceramic exhibited square or rectangular shape. When compared to the pure KNN ceramic, there is no significant difference in grain size for the x=0.055 and x=0.06 samples. For x>0.06, the grains of the ceramics grow swiftly, and the average grain sizes of the KNN-0.065Li and KNN-0.07Li samples are nearly twice of KNN. This result can be explained by the appearance of liquid-phase sintering, which facilitated the grain growth. Furthermore, the energy barrier for the jump of the oxygen vacancies in the distorted structure may be higher than in the non-distorted structure (62). So, the transport of oxygen ions in the tetragonal phase may be easier than in the orthorhombic phase. Hence, the oxygen diffusion in the grains and/or grain boundaries was increased in the KNN-0.065Li and KNN-0.07Li ceramics with dominant tetragonal phase.

Figure 21 depicts the temperature dependence of dielectric constant (ϵ) and dielectric loss ($\tan \delta$) of the KNN-xLi samples, which are measured at frequency of 10 kHz over wide temperatures range between 0 and 500°C . All ceramics showed two

phase transition peaks, associate with the orthorhombic ferroelectric-tetragonal ferroelectric phase transition (T_{O-T}) and tetragonal ferroelectric-cubic paraelectric phase transition (T_C), respectively (Figure 21 (a)) (63). The T_{O-T} of the ceramics shifted to low temperature from 197 to 60°C with increasing x from 0 to 0.07. On the contrary, the T_C of ceramics moved to high temperature from 428 to 470°C with rising x from 0 to 0.07. In the inset of Figure. 21 (a), the changes in T_{O-T} and T_C of all compositions can be apparently seen. The increased tetragonal distortion of the ceramics results in T_C rising. The Li^+ substitution can be improved the dielectric constant at Curie temperature (ϵ_C) of the ceramics (Figure 21 (a)). Furthermore, the loss peak at T_C shifted to high temperature upon rising x and the heights of these peaks of the Li substitution were enhanced heavily (Figure 21 (b)). The high loss generated by the Li^+ doping may be ascribed to high concentration flaws due to the appearance of the liquid phase and the over-growth grains. Figure 22 demonstrates the remanent polarization (P_r), field-induced strain (S_{33}) and d_{33} of the KNN-xLi ceramics with different x . The P_r , S_{33} and d_{33} tends to enhanced when x increased up to 0.06, and then dropped. With $x=0.06$, the sample show highest P_r , S_{33} and d_{33} of $\sim 25 \mu\text{C}/\text{cm}^2$, $\sim 0.13\%$ and $\sim 190 \text{ pC}/\text{N}$, respectively. This phenomenon can be explained by the MPB region, resulting in increment of the electrical properties.

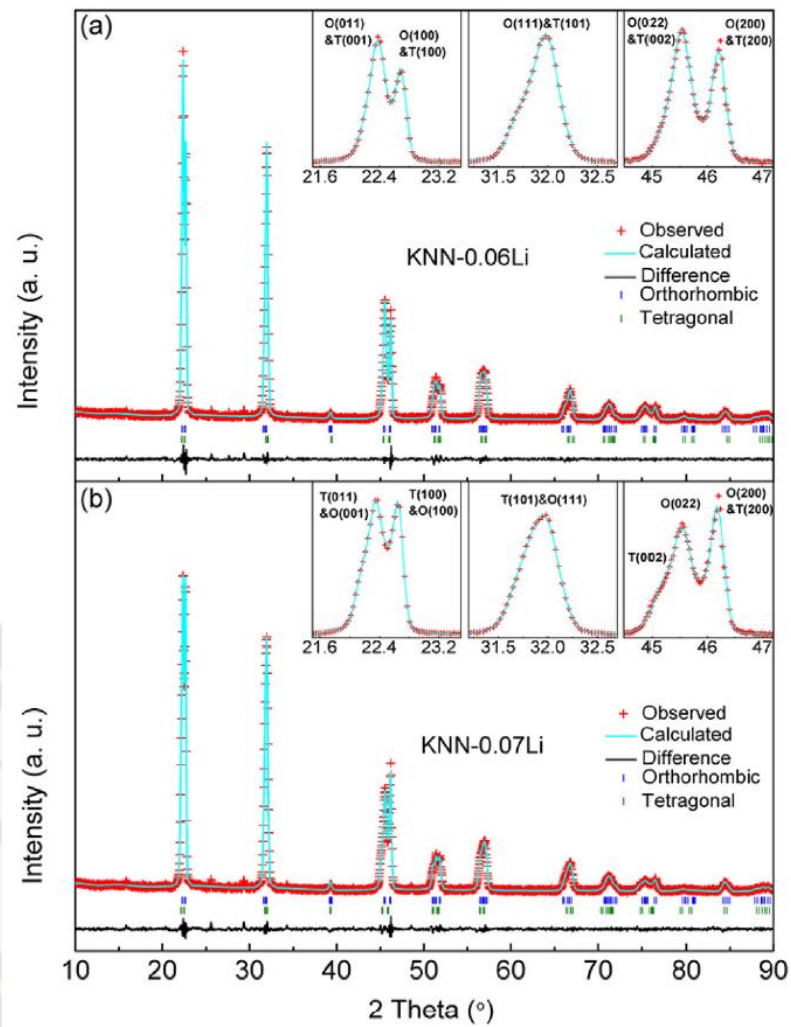


Figure 19 Rietveld refinements on XRD data for (a) the KNN-0.06Li and (b) the KNN-0.07Li ceramics.

Table 2 Crystal data and structure refinement conditions for the KNN-0.06Li and KNN-0.07Li. The distortions for orthorhombic phase and tetragonal phase are designed as $2(c-b)/(c+b)$.

Composition	KNN-0.06Li		KNN-0.07Li	
	Orthorhombic	Tetragonal	Orthorhombic	Tetragonal
Crystal system	Orthorhombic	Tetragonal	Orthorhombic	Tetragonal
Space group	<i>Amm2</i>	<i>P4mm</i>	<i>Amm2</i>	<i>P4mm</i>
Proportion (%)	58.37	41.63	24.43	75.57
<i>a</i> (Å)	3.94306	3.95542	3.93538	3.93538
<i>b</i> (Å)	5.62203	3.95542	5.62135	5.62135
<i>c</i> (Å)	5.67042	4.00699	5.66264	5.66264
<i>V</i> (Å ³)	125.702	62.691	125.270	125.270
Distortion (%)	0.857	1.295	0.732	0.732
<i>R</i> _{wp}	0.0522	-	0.0529	-
<i>R</i> _p	0.0389	-	0.0384	-
Reduced (χ^2)	1.476	-	1.588	-
Goodness of fit	1.21	-	1.26	-

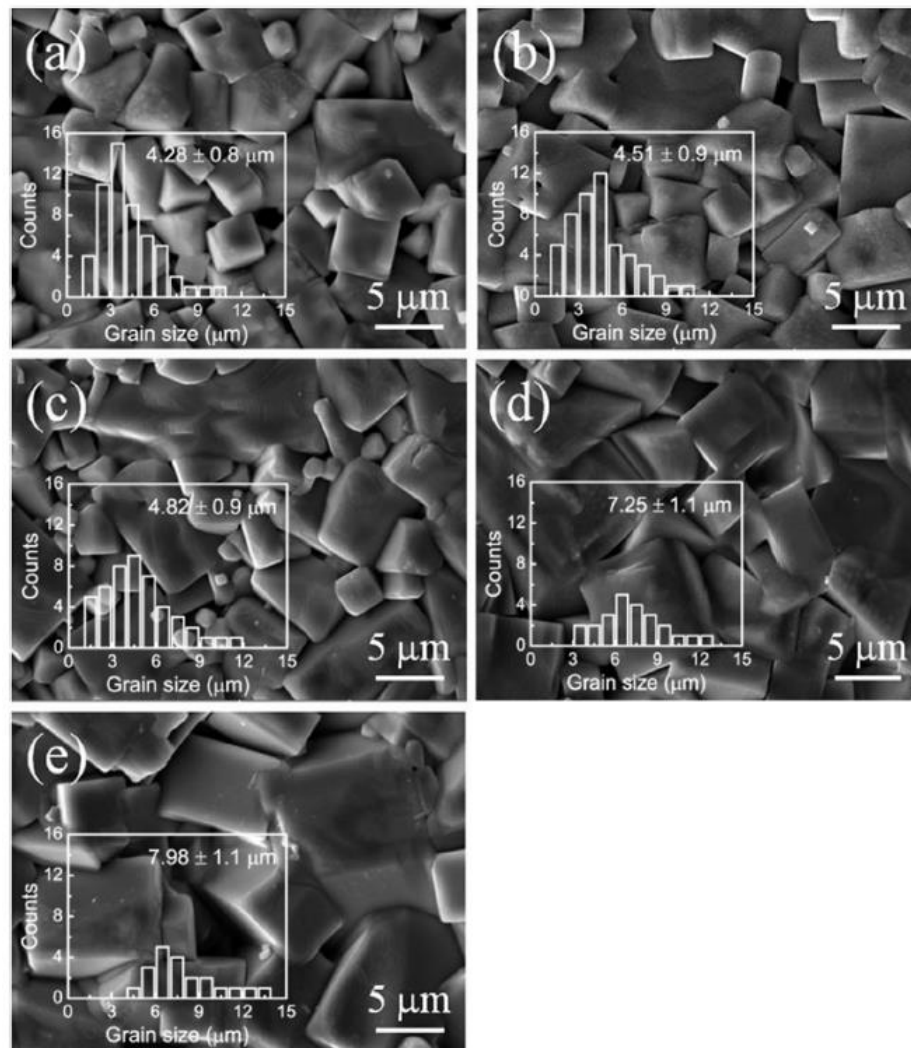


Figure 20 SEM micrographs of KNN-xLi ceramics with different x (a) 0, (b) 0.055, (c) 0.06, (d) 0.065 and (e) 0.07. The insets depict grain size distributions.

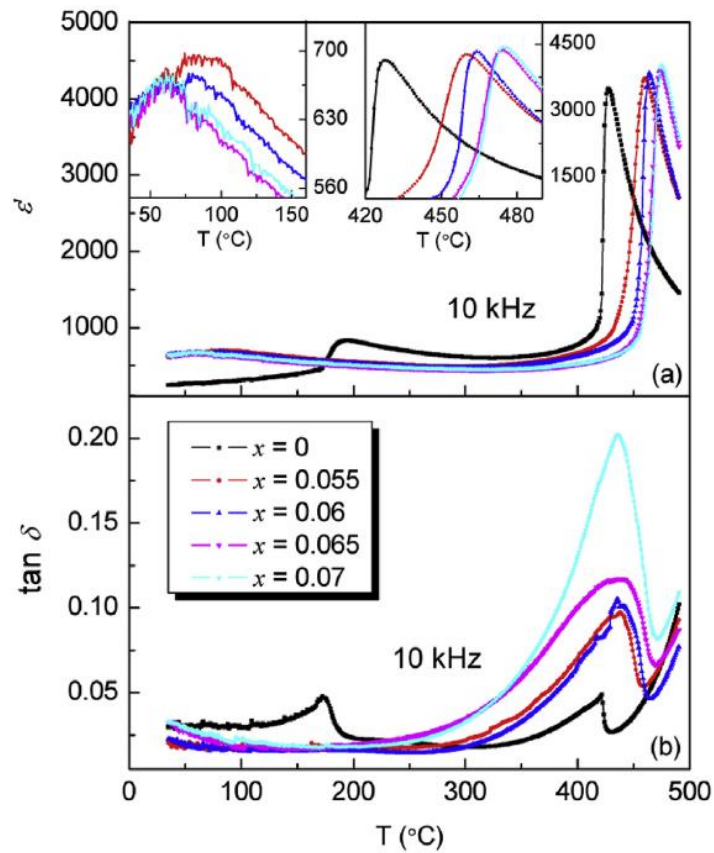


Figure 21 Temperature dependence of (a) dielectric permittivity and (b) dielectric loss of the KNN-xLi samples with different x.

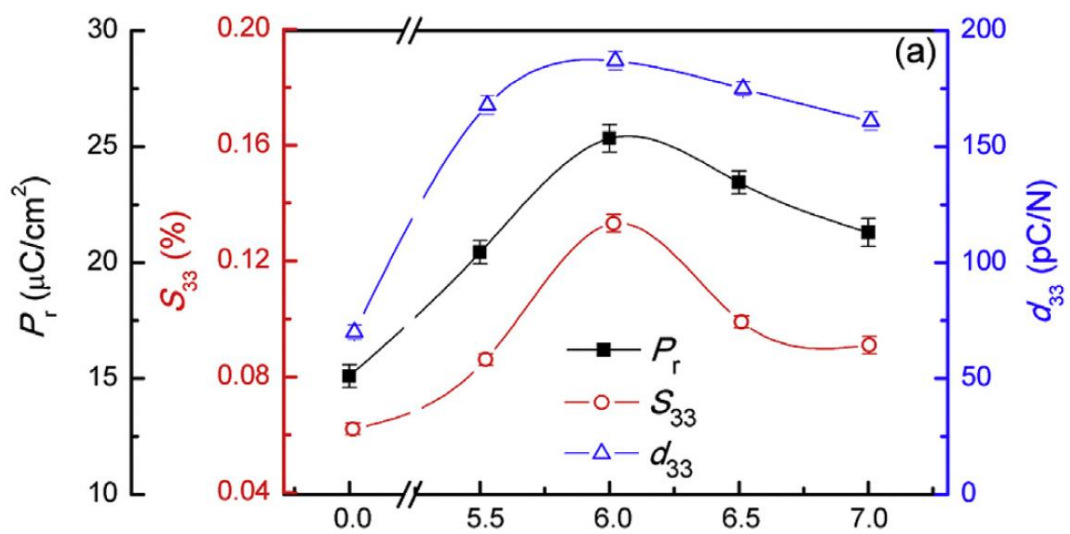


Figure 22 The P_r , S_{33} and d_{33} for the KNN-xLi samples with different x.

2. For the additional doping of element or compounds in KNN-based ceramics

Xiaodan Ren et al. (64) investigated the effect of Li_2O on the structure and electrical properties of $0.93\text{K}_{0.5}\text{Na}_{0.5}\text{NbO}_3\text{-}0.07\text{SrZrO}_3\text{-}x\text{Li}_2\text{O}$; $0.93\text{KNN}\text{-}0.07\text{SZ}\text{-}x\text{Li}$ ceramics ($x=0, 0.03, 0.07, 0.10, \text{ and } 0.13$ wt.%) using the conventional solid-state method (calcination temperature of 850°C for 5 h and a sintering temperature of 1270 and 1280°C for 6-10 h). The XRD patterns at room temperature of $0.93\text{KNN}\text{-}0.07\text{SZ}\text{-}x\text{Li}$ ceramics with various x are exhibited in Figure 23. With $0 \leq x \leq 0.07$, the samples display pure perovskite structure (Figure 23 (a)). When $x \geq 0.07$, the impurity phase of $\text{K}_3\text{Li}_2\text{Nb}_5\text{O}_{15}$ is identified (Figure 23 (a)). For further scrutiny of the phase formation, the diffraction peaks at the 2θ range from $44\text{-}48^\circ$ was amplified (Figure 23 (b)). The ceramics with $x=0$ present orthorhombic phase. After that, the tetragonal phase gradually emerges as x rises from 0.03, 0.07 to 0.10 and ultimately entirely becomes a tetragonal phase with $x=0.13$.

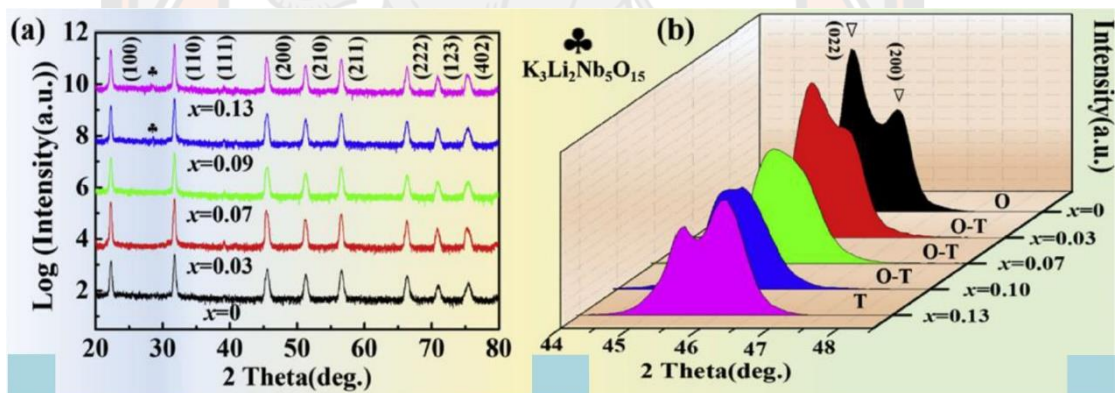


Figure 23 XRD patterns of $0.93\text{KNN}\text{-}0.07\text{SZ}\text{-}x\text{Li}$ ceramics in the 2θ range of (a) $10\text{-}70^\circ$ and (b) $44\text{-}48^\circ$.

Figure 24 (a-e) shows the SEM images of $0.93\text{KNN}\text{-}0.07\text{SZ}\text{-}x\text{Li}$ ceramics. With $x=0$, the morphology of ceramic exhibited small grains and good mass density (Figure 24 (a) and (f)). As x rising, the grains grow significantly and an inhomogeneous grain distribution appears (Figure 24 (a) and (f)). When $x=0.03$, the

sample shows small grains intercalate between large grains, leading to higher bulk density (Figure 24 (f)).

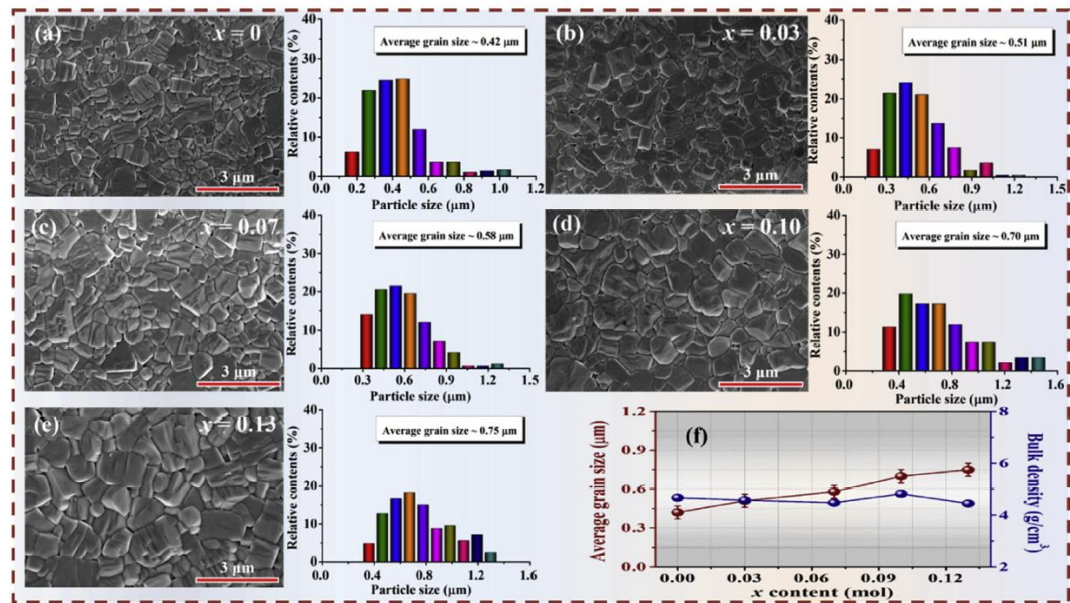


Figure 24 SEM image of 0.93KNN-0.07SZ- x Li ceramics with (a) $x=0$, (b) $x=0.03$, (c) $x=0.07$, (d) $x=0.10$, (e) $x=0.13$ and (f) The average grain size and bulk density of the 0.93KNN-0.07SZ- x Li ceramics with different x .

The temperature dependence of the dielectric constant (ϵ) and loss tangent ($\tan \delta$) of the 0.93KNN-0.07SZ- x Li ceramics at varying frequencies (1-200 kHz) are shown in Figure 25. All ceramics showed two phase transition peaks, associate with the orthorhombic ferroelectric-tetragonal ferroelectric phase transition at $\sim 130^\circ\text{C}$ (T_{O-T}) and tetragonal ferroelectric-cubic paraelectric phase transition at $\sim 280^\circ\text{C}$ (T_m), respectively (Figure 25 (a-e)) (64). The T_m of ceramics tend to enhanced when rising x (Figure 25 (a-e)). The ϵ_r of samples enhanced when x increases from 0 to 0.03, and then dropped (Figure 25 (a-e)). The samples with $x=0.03$ show highest the ϵ as 9643. Figure 25 (f) presents the plot of T_m and ϵ of 0.93KNN-0.07SZ- x Li ceramics with different x .

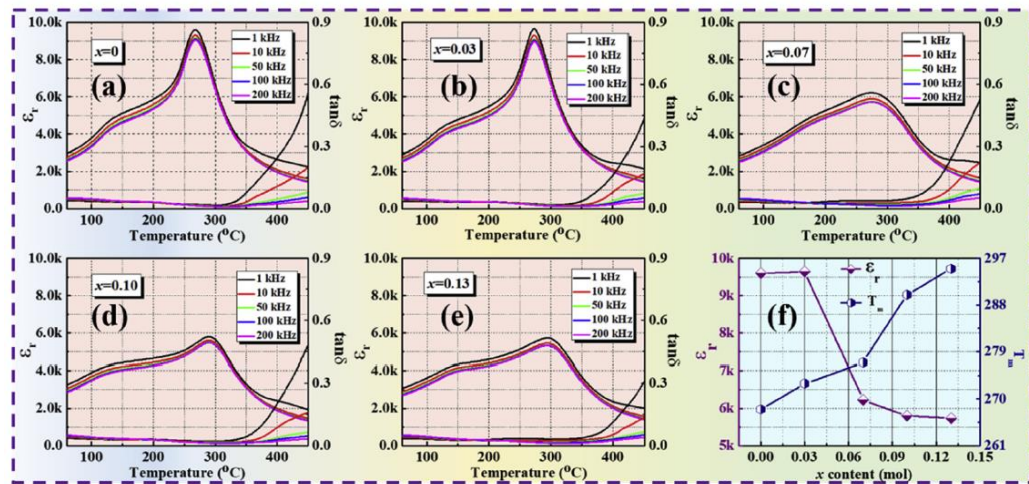


Figure 25 Temperature-dependent dielectric constant and dielectric loss of the 0.93KNN-0.07SZ- x Li ceramics with (a) $x=0$, (b) $x=0.03$, (c) $x=0.07$, (d) $x=0.10$, (e) $x=0.13$ and (f) The T_m and ε of the 0.93KNN-0.07SZ- x Li ceramics with different x .

Figure 26 (a) displays the polarization-electric field (P - E) hysteresis loops of the 0.93KNN-0.07SZ- x Li ceramics with different x . The saturated P - E loops appear in all samples, but the saturation characteristic goes gradually reduced when x rises, indicating a strengthened relaxor behavior. Figure 26 (b) demonstrates the remanent polarization (P_r), d_{33} and k_p of the 0.93KNN-0.07SZ- x Li ceramics with different x . The P_r , d_{33} and k_p tends to enhanced when x increased up to 0.03, and then dropped. The sample with $x=0.03$ shows highest P_r , d_{33} and k_p of $\sim 15 \mu\text{C}/\text{cm}^2$, $\sim 150 \text{ pC}/\text{N}$ and $\sim 0.26\%$, respectively. To feature the thermal stability of the ceramics, the correlation between normalized d_{33} ($d_{33}(T)/d_{33}(\text{RT})$) and annealing temperature (T_a) was inspected, as shown in Figure 26 (c). They reported that d_{33} decrease slightly with T_a increased and then drops swiftly when T_a exceeds T_c . In particular, the piezoelectricity retains 86% ($d_{33} \sim 129 \text{ pC}/\text{N}$) of the room temperature value as T_a goes up to 270°C . Figure 26 (d) displays schematic diagram of the reason for d_{33} increasing at $x=0.03$. It can be seen that introduction of Li^+ cause abnormal grain growth (AGG), while some grains retain their size and occupy the interstitial positions of the large grains, leading to a highest bulk density and d_{33} of the samples.

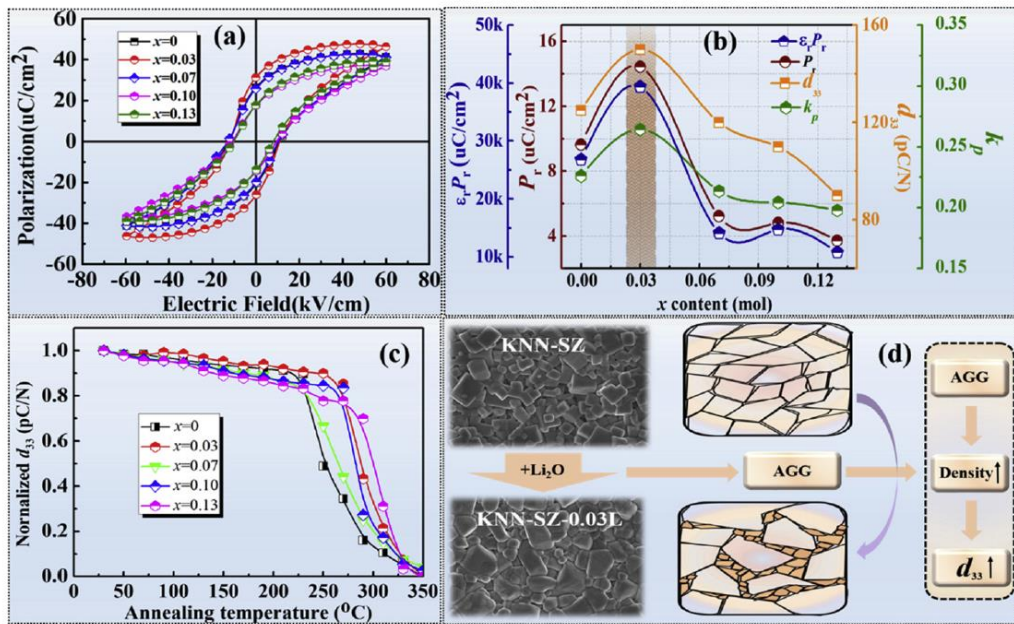


Figure 26 (a) P - E loops and (b) the variation of P_r , d_{33} and k_p ; (c) d_{33} against annealing temperature of the 0.93KNN-0.07SZ- x Li samples with various x ; (d) Schematic diagram explains why the sample with $x = 0.03$ has a high d_{33} .

CHAPTER III

RESEARCH METHODOLOGY

This chapter elaborates the experimental procedure, which contains the samples synthesis and characterization. The $(K_{0.5}Na_{0.5})(Nb_{0.7}Ta_{0.3})O_3$ with different firing conditions, and $K_{0.5-x}Cs_xNNT$, $KNNT-xCs$, $KN_{0.5-x}Li_xNT$ and $KNNT-xLi$ with different x are synthesized using solid-state combustion technique. The details of the experimental procedure are set out in the following sections.

Samples Synthesis

The solid-state combustion method has been broadly used in preparation electro ceramics owing to its reduced firing temperature and soaking time and the production of a pure phase with ultrafine homogeneous particles. The main benefit of this approach results from the release from the ignition of fuel (i.e., glycine), which speeds up the chemical reaction between raw materials and also helps to reduce the reaction temperature. Including, ceramics fabricated by this technique display high density and good electrical behaviors.

The synthesis of powders and ceramics of $KNNT$, $K_{0.5-x}Cs_xNNT$, $KNNT-xCs$, $KN_{0.5-x}Li_xNT$ and $KNNT-xLi$ at $x=0, 0.10, 0.02, 0.03$ and 0.04 mol.%

Analytical-grade metal oxides and carbonate powders of $KHCO_3$ (99.7%, Ajax, NZ), $NaNO_3$ (99%, Ajax, NZ), Nb_2O_5 (99.99%, Eleps, RU), Ta_2O_5 (99%, Sigma, CN), Cs_2CO_3 (99.7%, Ajax, NZ) and Li_2CO_3 (99%, Sigma, CN) were used as the starting materials for synthesizing samples. They were weighed and mixed in proportion the formulae: (8) $[(K_{0.5}Na_{0.5})(Nb_{0.7}Ta_{0.3})O_3$; $KNNT$], (9) $[(K_{0.5-x}Cs_xNa_{0.5})(Nb_{0.7}Ta_{0.3})O_3$; $K_{0.5-x}Cs_xNNT$ ($x=0, 0.01, 0.02, 0.03$ and 0.04 mol.%)], (10) $[(K_{0.5}Na_{0.5})(Nb_{0.7}Ta_{0.3})O_3-xCs_2CO_3$; $KNNT-xCs$ ($x=0, 0.01, 0.02, 0.03$ and 0.04 mol.%)], (11) $[(K_{0.5}Na_{0.5-x}Li_x)(Nb_{0.7}Ta_{0.3})O_3$; $KN_{0.5-x}Li_xNT$ ($x=0, 0.01, 0.02, 0.03$ and 0.04 mol.%) and (12) $[(K_{0.5}Na_{0.5})(Nb_{0.7}Ta_{0.3})O_3-xLi_2CO_3$; $KNNT-xLi$ ($x=0, 0.01, 0.02, 0.03$ and 0.04 mol.%)], where excess $KHCO_3$ and $NaNO_3$ were added 1 wt.% to compensate for the volatility of K and Na during calcination and sintering. The mixed

powders were ball-milled method within a poly bottle with zirconia balls in ethanol for 24 h. The suspensions were dried at a temperature of $\sim 100^\circ\text{C}$ and mixed with glycine in an agate mortar. The KNNT powders were calcined at a temperature between 600 and 800°C for 2 h in air. The $\text{K}_{0.5-x}\text{Cs}_x\text{NNT}$, KNNT-xCs , $\text{KN}_{0.5-x}\text{Li}_x\text{NT}$ and KNNT-xLi powders were calcined at a temperature between 600°C for 2 h in air. Next, the calcined powders were combined with 3 wt.% polyvinyl alcohol (PVA) binder solution followed by ball-milled again for 12 h. The resultant mixtures were dried, sieved, and compacted into pieces at a pressure of 80 MPa with a diameter of ~ 15 mm and a thickness of ~ 1.5 mm using a hydraulic press. After burning off PVA, the KNNT samples were sintered at a temperature between 1150 - 1190°C for 2-5 h in air. For the $\text{K}_{0.5-x}\text{Cs}_x\text{NNT}$ samples were sintered at 1130°C for 4 h in air. In the event of the KNNT-xCs , $\text{KN}_{0.5-x}\text{Li}_x\text{NT}$ and KNNT-xLi samples were sintered at 1150°C for 4 h in air. For the SEM specimen preparation, the polishing with sandpaper and an alumina abrasive on the surface's samples were carried out. Then, they were thermally etched at a temperature 80°C less than the sintering temperature for 30 min to disclose their grain boundaries. To prepare the samples for their electric property measurements, the ceramics were coated with silver paste on both sides, to form electrodes, and then fired at 550°C for 30 min. The diagram of the synthesis process of KNNT, $\text{K}_{0.5-x}\text{Cs}_x\text{NNT}$, KNNT-xCs , $\text{KN}_{0.5-x}\text{Li}_x\text{NT}$ and KNNT-xLi powders and ceramics are shown in the Figure 27, 28, 29, 30 and 31, respectively.

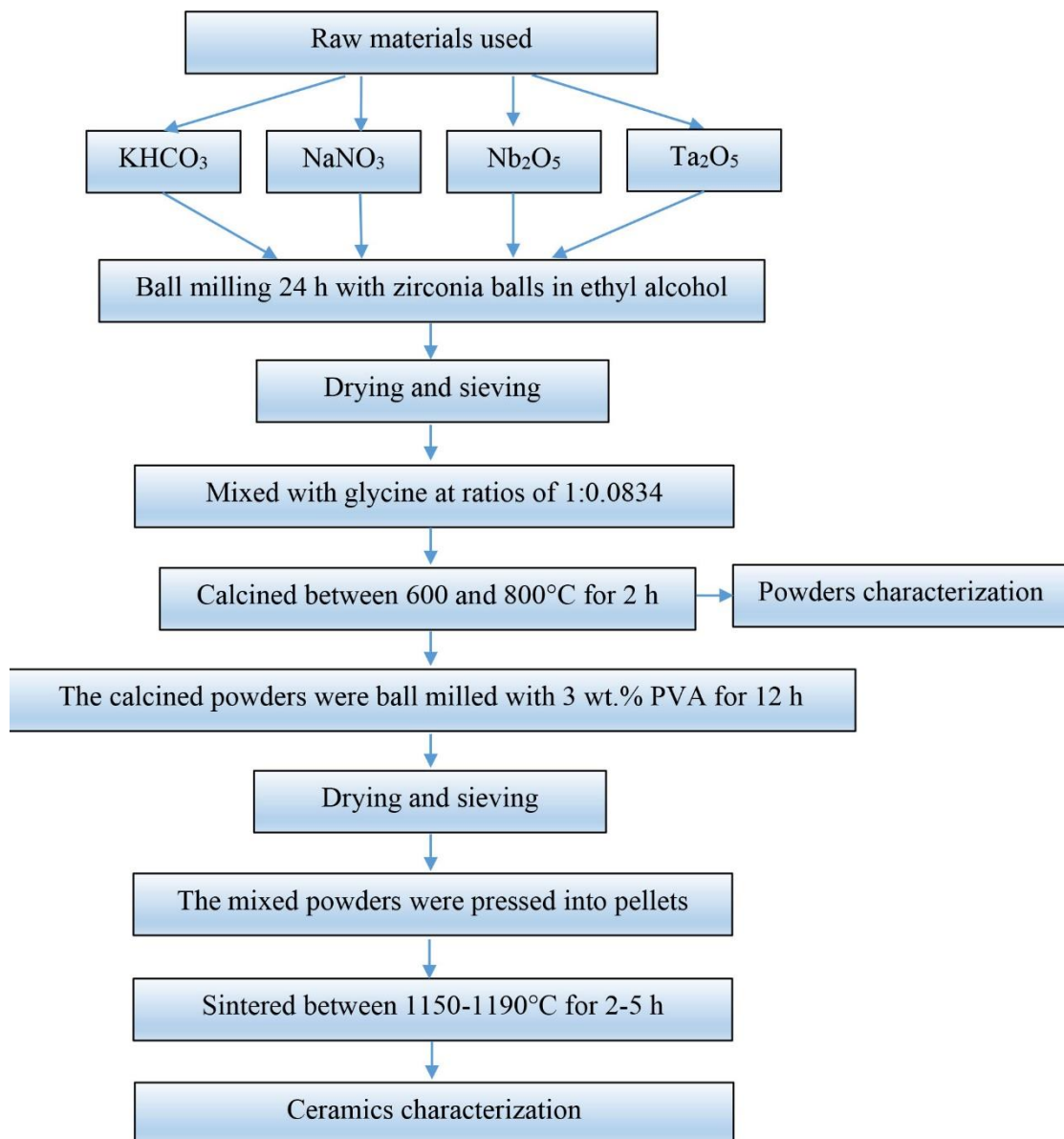


Figure 27 Diagram of the synthesis process of KNNT powders and ceramics.

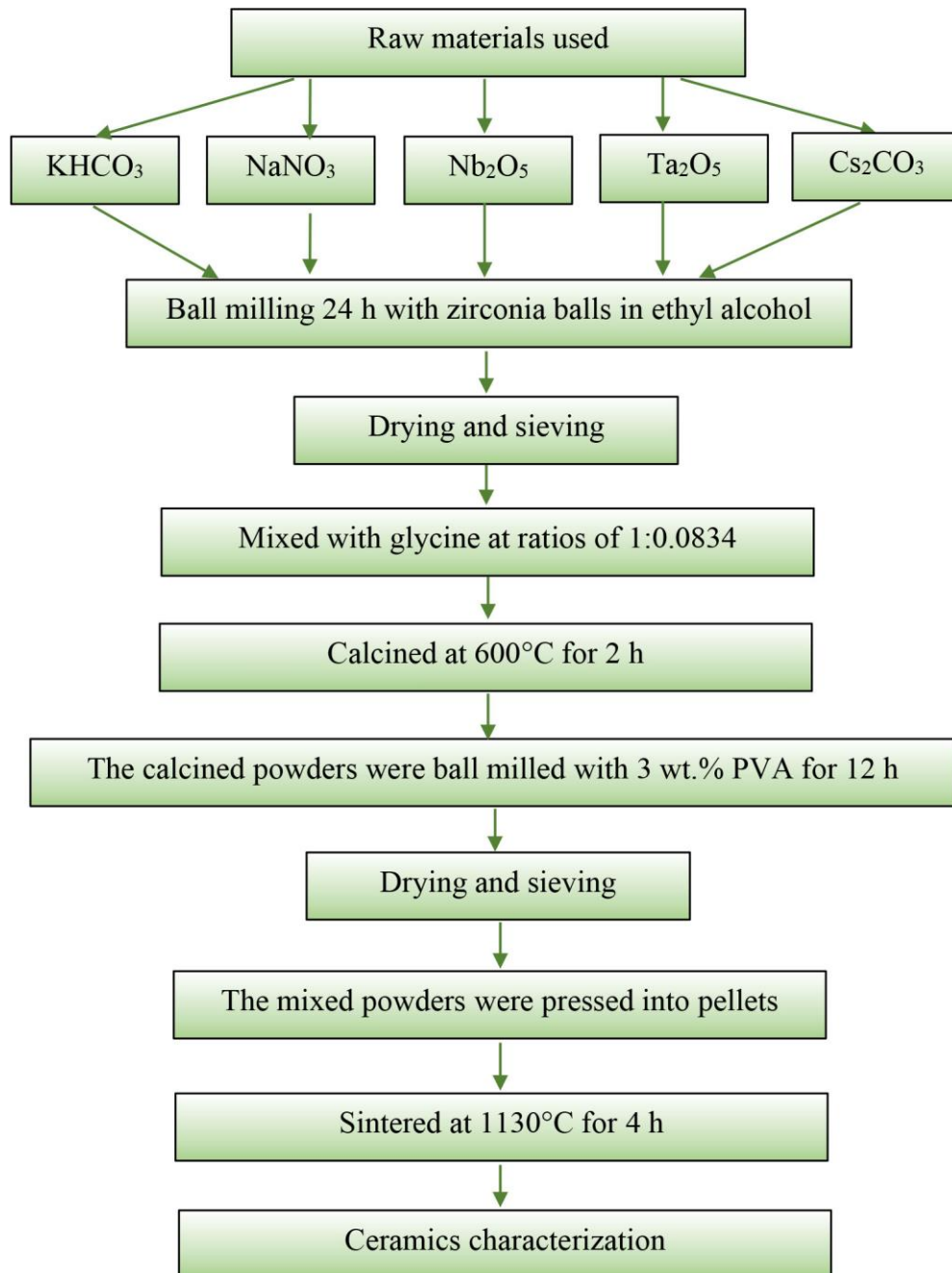


Figure 28 Diagram of the synthesis process of $K_{0.5-x}Cs_xNNT$ powders and ceramics.

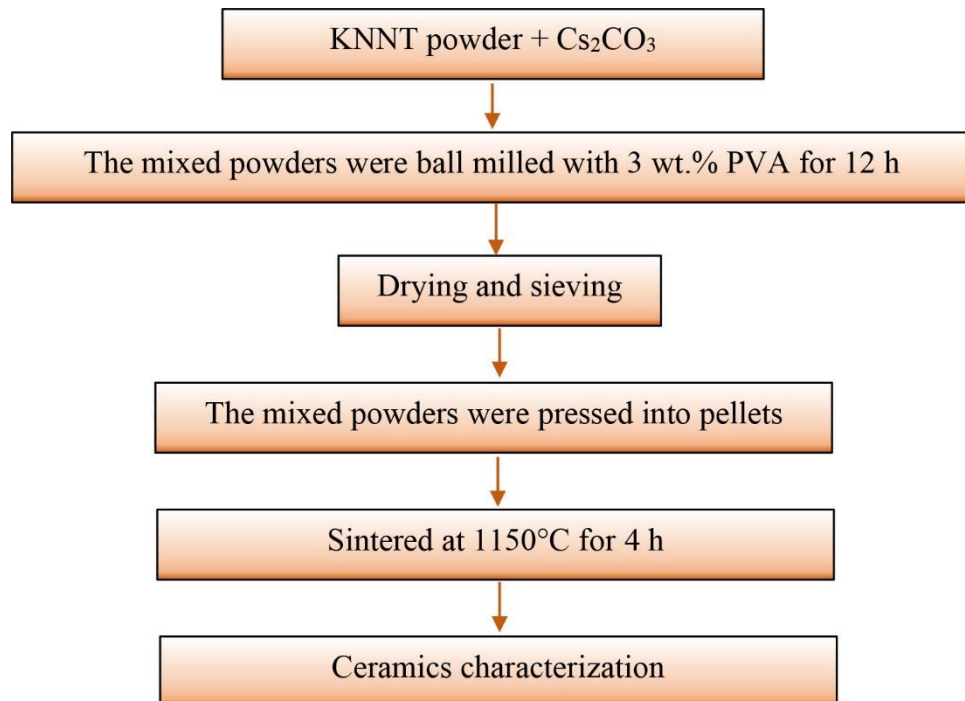


Figure 29 Diagram of the synthesis process of KNNT-xCs ceramics.

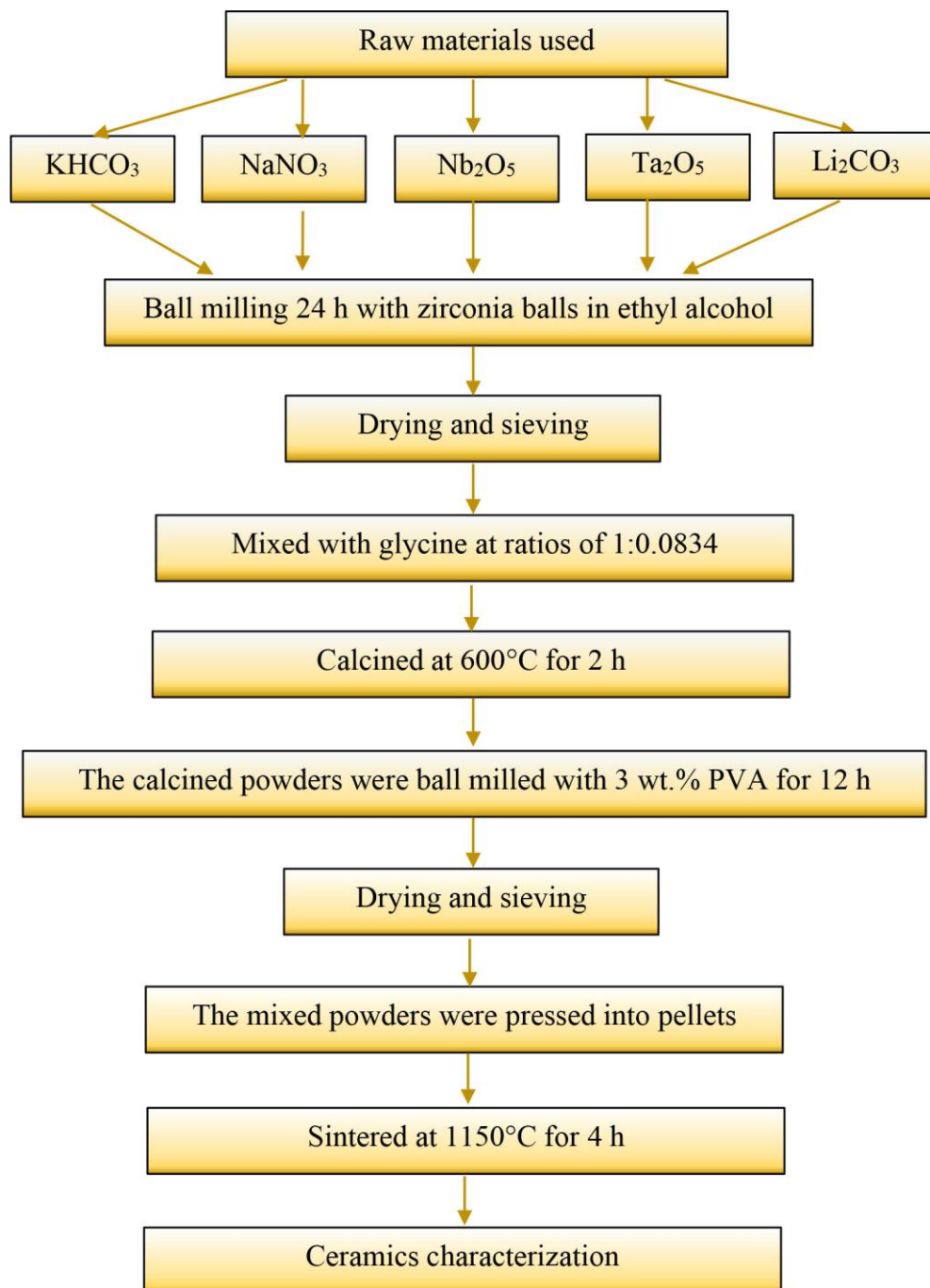


Figure 30 Diagram of the synthesis process of $\text{KN}_{0.5-x}\text{Li}_x\text{NT}$ powders and ceramics.

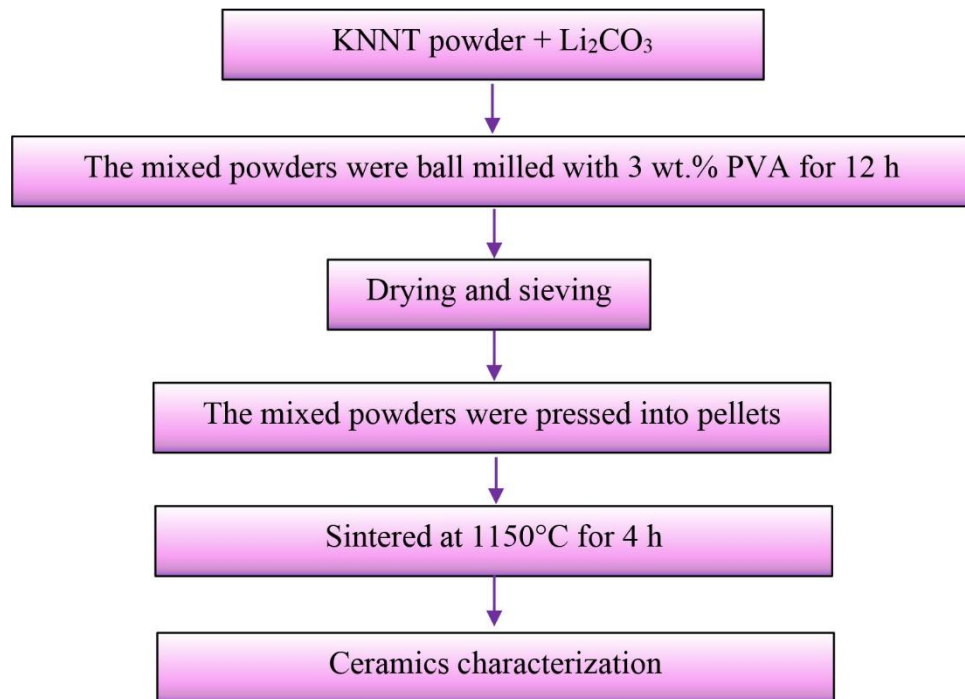


Figure 31 Diagram of the synthesis process of KNNT-xLi ceramics.

Samples Characterization

The KNNT powders were characterized about phase structure and microstructure with different tools, as seen in Figure 32.

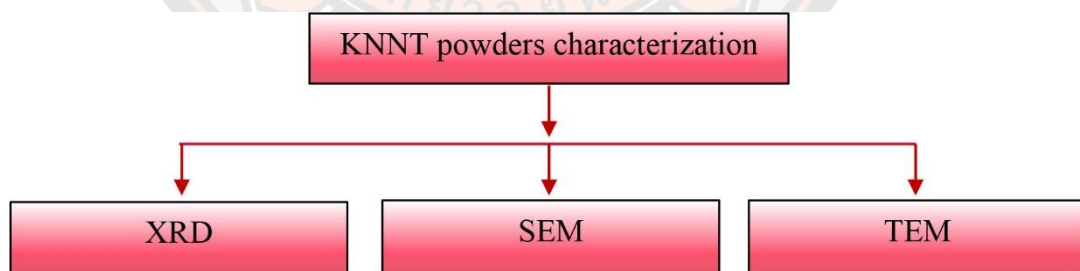


Figure 32 Diagram of samples characterization of KNNT powders.

The K_{0.5-x}Cs_xNNT, KNNT-xCs, KN_{0.5-x}Li_xNT and KNNT-xLi ceramics were characterized about physical and electrical properties with different tools, as seen in Figure 33.

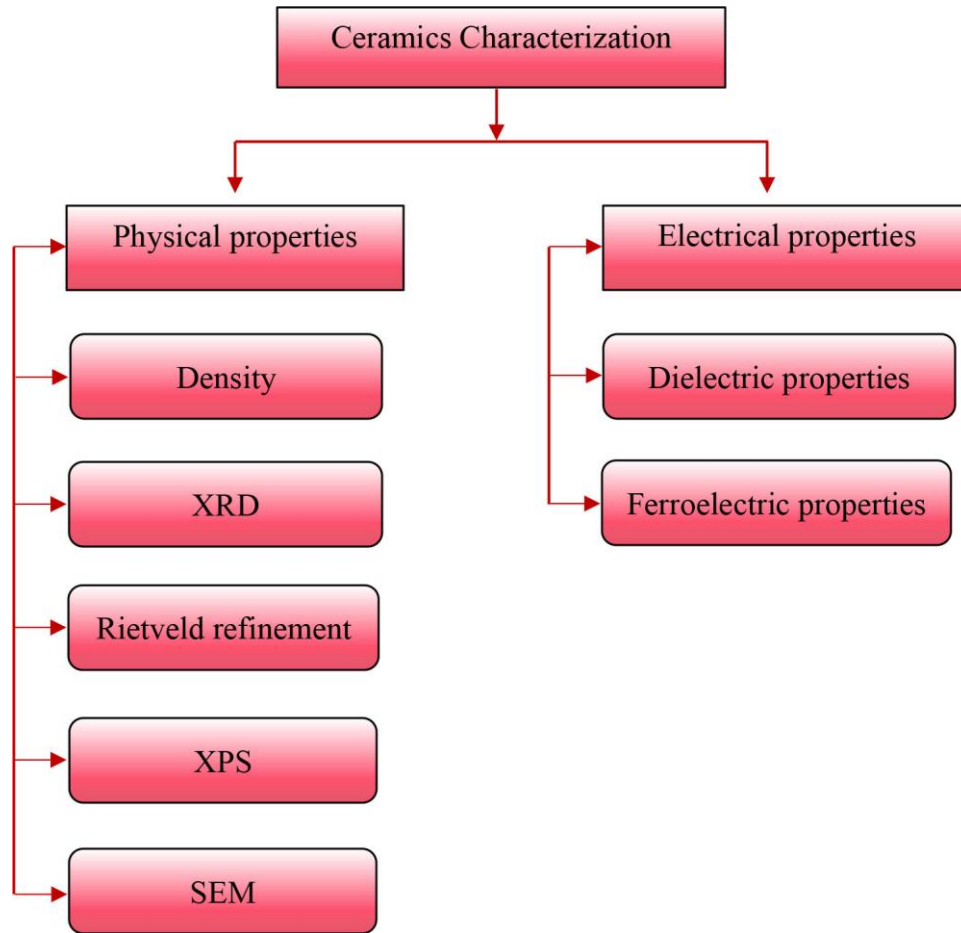


Figure 33 Diagram of samples characterization of $K_{0.5-x}Cs_xNNT$, $KNNT-xCs$, $KN_{0.5-x}Li_xNT$ and $KNNT-xLi$ ceramics.

Physical properties

X-ray diffraction (XRD) technique (65)

X-ray diffraction analysis (XRD) is a technique used in materials science to evaluate the phase formation and phase purity of materials as well as complete information about crystallographic symmetry. In this study, the X-ray diffraction pattern of the samples was recorded using an X-ray diffractometer (XRD, Bruker, D2 Phaser) with Cu-K α radiation ($\lambda = 1.5418 \text{ \AA}$) at room temperature. Figure 34 displays an X-ray diffractometer. For the detection limit, the XRD technique can't identify the deformation of a material substance with less than 5% of deformation in systems. The

percentage purity of the perovskite structure can be calculated following the equation (13)

$$\% \text{ perovskite phase} = \left(\frac{I_{\text{perovskite}}}{I_{\text{perovskite}} + I_{\text{impurity}}} \right) \times 100 \quad (13)$$

Where $I_{\text{perovskite}}$ is the highest intensity of the perovskite peak.

I_{impurity} is the highest intensity of impurity peak.



Figure 34 X-ray diffraction instruments

Rietveld refinement technique (66, 67)

Rietveld refinement technique was used to confirm the phase structure of samples by fitting the XRD information with the Fullprof software. Figure 35 demonstrated windows of the FullProf Suite toolbar. The original values of the cell parameters, lattice constants, space group and atom functional positions were acquired from the relating reference designs determined from the Crystallography Open Database (COD). A structural model based on KaNbNbO_3 with a tetragonal phase (T),

with a $P4mm$ space group, and an orthorhombic phase (O), with an $Amm2$ space group, were used as the initiating models for refining the all ceramics' XRD data. A Chebyshev polynomial function was used to fit the background, and a Pseudo-Voigt function was used to characterize the peak shape. A linear combination of Lorentzian and Gaussian functions is known as the Pseudo-Voigt function. A principle of this program is minimizing the difference between calculated intensities (model data) and the observed intensity points (experimental data). The quality values such as R_p (profile reliability), R_{wp} (weighted pattern reliability), R_{exp} (expected residual) and χ^2 (goodness of fit) was used for the calculation to create the model data which was described below by following equations:

$$R_p = 100 \frac{\sum |y_{oi} - y_{ci}|}{\sum y_{oi}} \quad (14)$$

$$R_{wp} = 100 \left\{ \frac{\sum w_i (y_{oi} - y_{ci})^2}{\sum w_i (y_{oi})^2} \right\}^{1/2} \quad (15)$$

$$R_{exp} = 100 \left\{ \frac{(N - P + C)}{\sum w_i (y_{oi})^2} \right\}^{1/2} \quad (16)$$

$$\chi^2 = \left[\frac{R_{wp}}{R_{exp}} \right] \quad (17)$$

Where: w_i is assigned a statistical weight.

y_{oi} is observed intensities for diffraction angle $2\theta_i$.

y_{ci} is calculated intensities for diffraction angle $2\theta_i$.

N is the total number of data point.

P is the number of parameters adjusted.

C is the number of constraints applied.

According to basic principle, $R < 15\%$ and $\chi^2 < 4$ which is considered acceptable (66-68).

In summary, this technique provides the lattice constants, atomic vibration, fractional occupancy and percentage phase of samples.

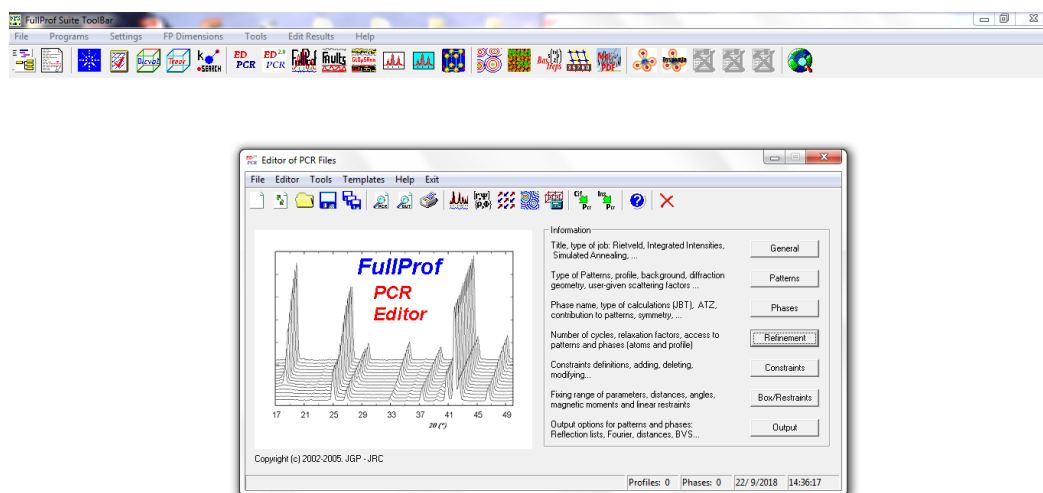


Figure 35 Windows of the FullProf Suite toolbar

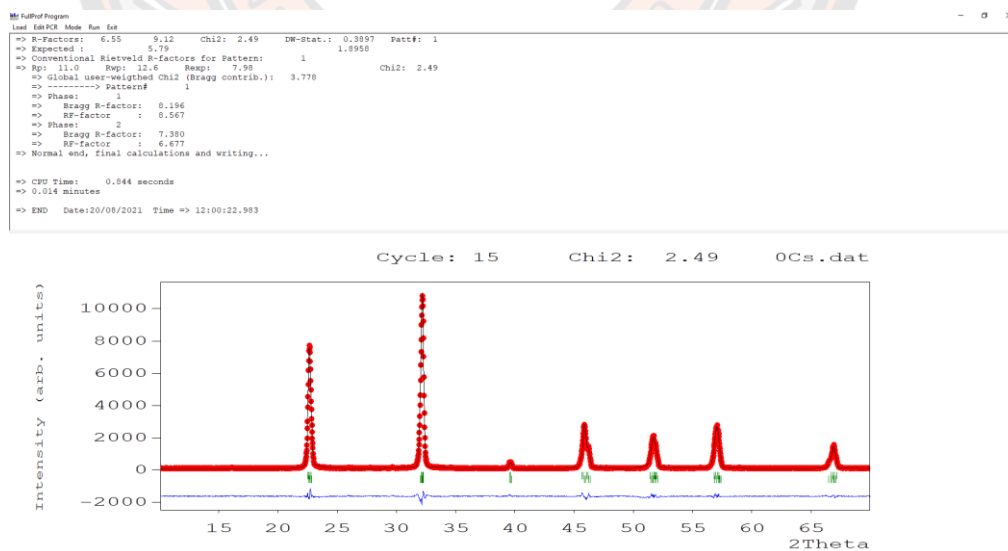


Figure 36 Rietveld refinement on XRD patterns of KNNT ceramic at 1150°C for 4 h.

X-ray photoelectron spectroscopy (XPS)

X-ray photoelectron spectroscopy (XPS) is an instrument used to inspect the chemical state of surface elements and detect chemical contamination of samples (Figure 37). It can analyze a sample to a depth of 2 to 5 nm. XPS is generally performed by exciting a samples surface with monochromatic $Al-K_{\alpha}$ radiation causing releasing of photoelectrons from the sample surface. The energy of the emitted photoelectrons was measured using an electron energy analyzer. From the binding energy and intensity of a photoelectron peak, the elemental identity, chemical state, and quantity of an identified element can be determined (69, 70).

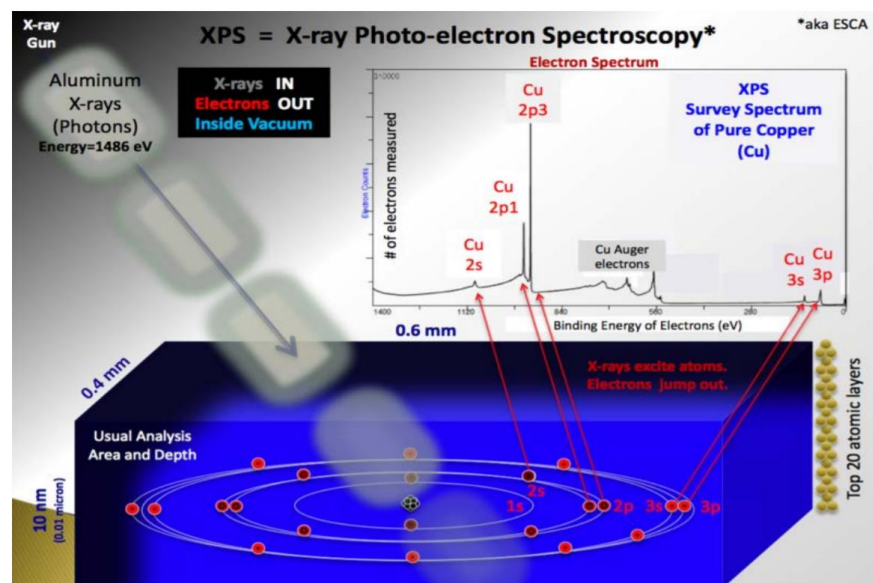


Figure 37 The XPS analysis of surface for pure copper sample.

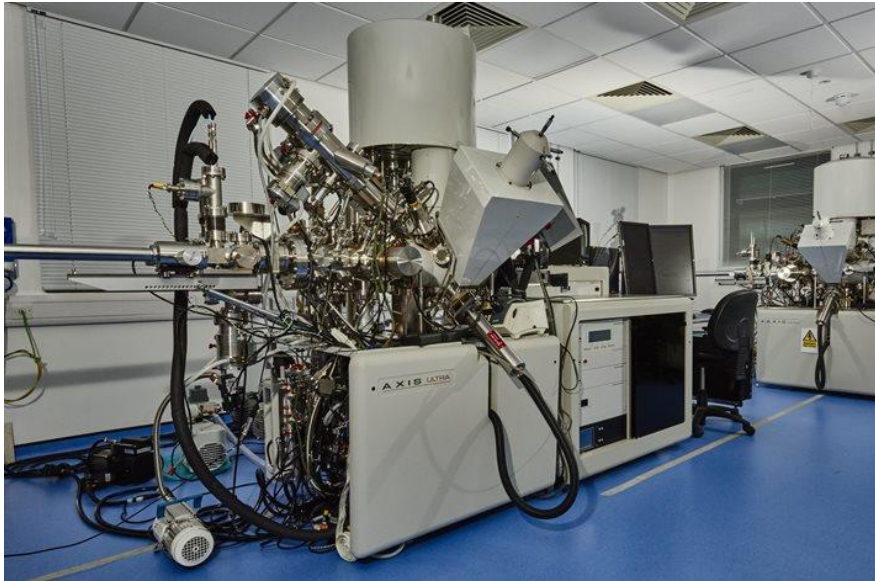


Figure 38 X-ray photoelectron spectroscopy (XPS).

Scanning electron microscopy (SEM) and Energy dispersive spectroscopy (EDS)

Scanning electron microscopy (SEM) is an instrument used to examine the morphology of powders and ceramics, such as size, agglomeration, shape and presence of porosity. Figure 39 demonstrated the basic principle of the SEM machine. The magnification of this camera was in the range of 25,000-100,000x (71). A linear interception technique was used to estimate the average grain size of ceramics. $D=L/N$ is the equation for a linear intercepting technique, where D represents the average grain size, L represents random linear lines on SEM micrograph and N is the total number of grain boundary intersections.

In addition, chemical analysis of the materials was carried out with Energy Dispersive Spectroscopy (EDS). For the principle of this technique, the beam of electrons is focused on the specimens. Atoms contain ground state electrons inside the material, which these electrons reside in discontinuous energy levels from the nucleus. Anywise, the electron beam can eject an electron from an inner shell leaving a hole, which is subsequently filled by the falling of an electron from an outer shell or higher energy level, as seen in Figure 40. The energy difference between these two energy levels was released in the form of an X-ray. The amount and energy of this X-

ray can be determined by a spectrometer. The released X-rays energies are the characteristics of the difference in the energy levels and atomic structure of each element which they were emitted. Therefore, the kind and quantity of the element in specimens can be specified (72). Figure 41 display Scanning Electron Microscope (SEM).

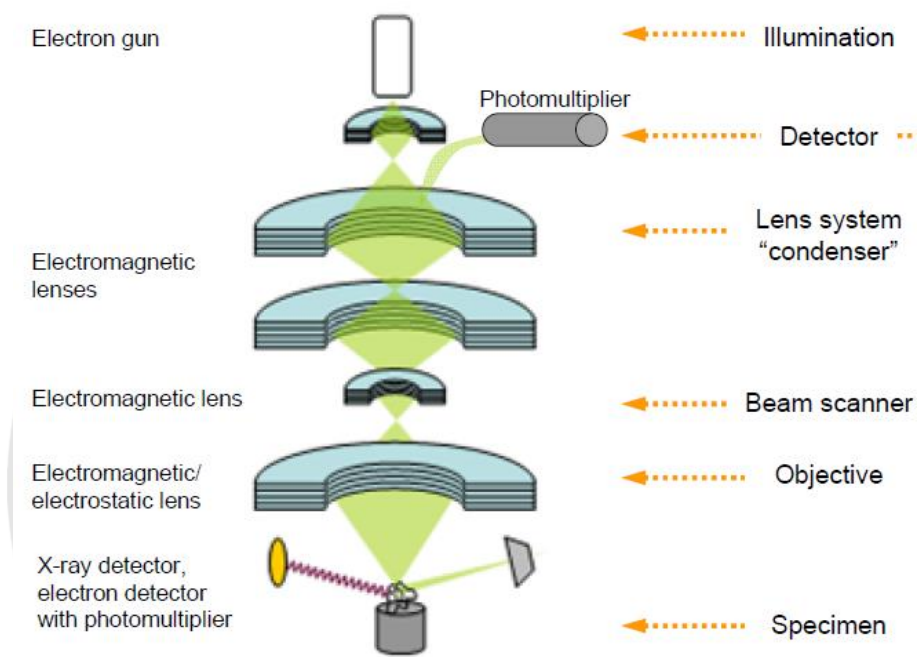


Figure 39 Schematic diagram of typical scanning electron microscope.

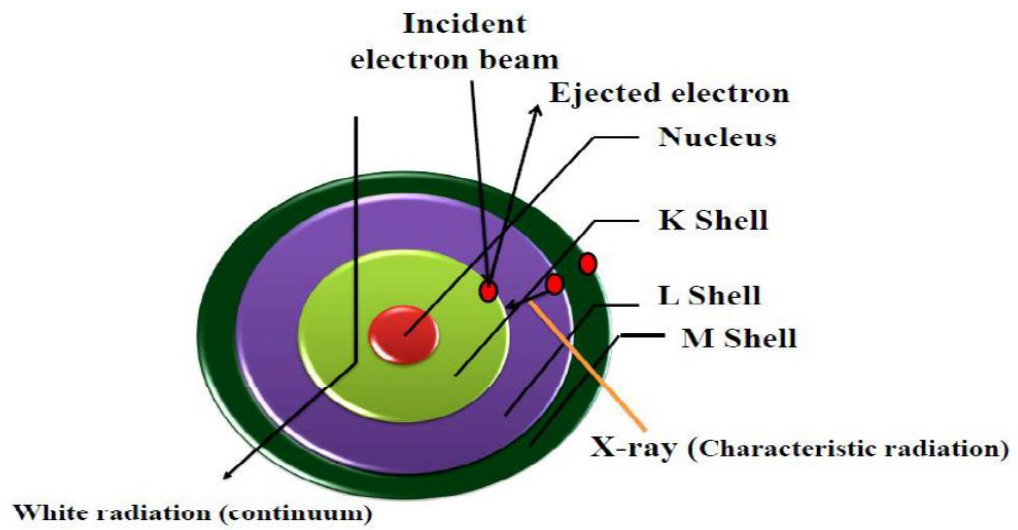


Figure 40 The interaction between an electron beam and electrons inside an atom used in EDS.

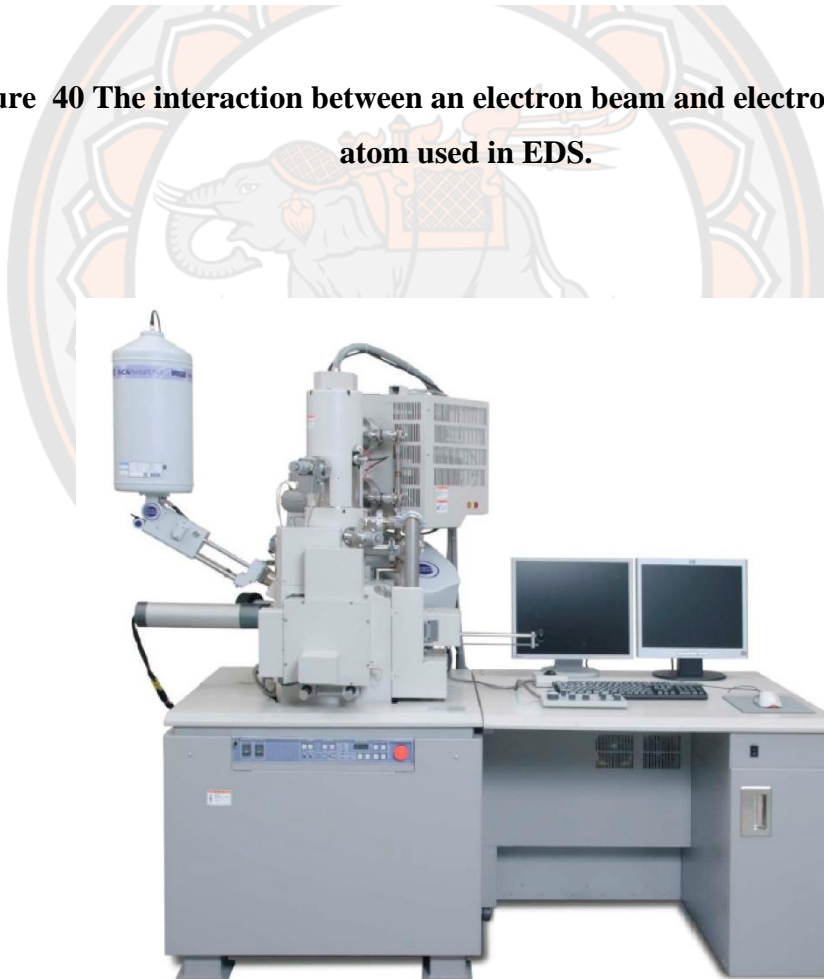


Figure 41 Scanning electron microscope (SEM).

Transmission electron microscopy (TEM) and Selected area electron diffraction (SAED)

Transmission electron microscopy (TEM) is highly powerful instrument in material science. A high-energy beam of electron is shone through a very thin specimen, and the interaction between the electrons and atoms can be used to investigate the surface structure i.e., defects, crystal structure of the atom, shape and size of the particle. The magnification of this camera was in the range of 25,000-700,000x (71, 73). Figure 42 illustrated the basic principle of the TEM machine. Selected area electron diffraction (SAED) pattern was used to study the phase structure and crystalline character of materials. Figure 43 display transmission electron microscopies (TEM).

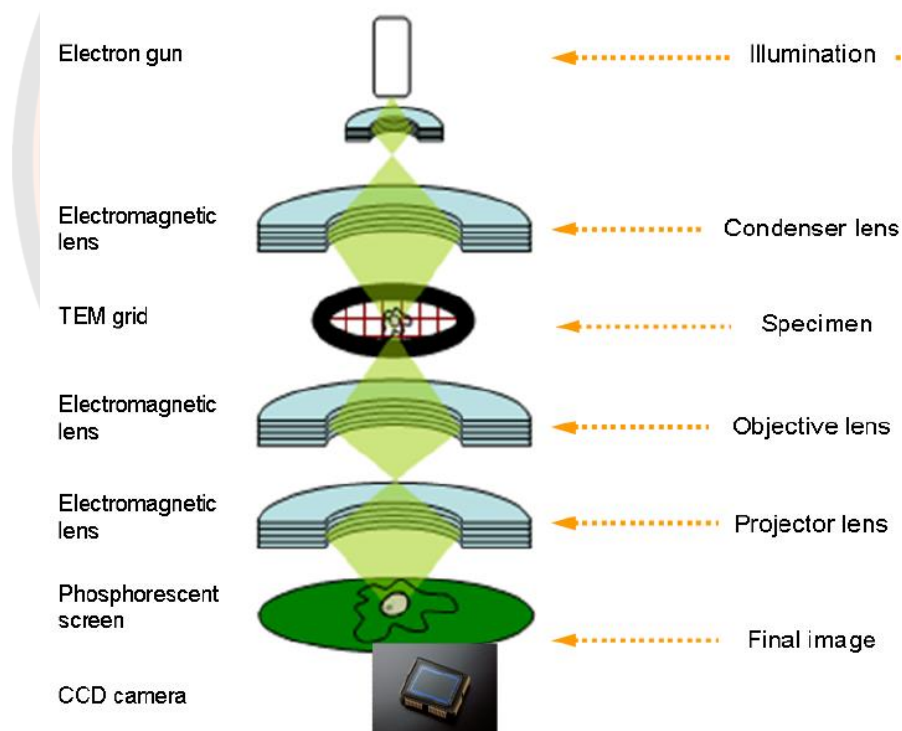


Figure 42 Schematic diagram of typical transmission electron microscopy.



Figure 43 Transmission electron microscopy (TEM).

Densification measurement

The density measurement of the ceramics was evaluated by Archimedes' technique (74) using distilled water as the medium. This concept can be explained that an object totally or partially immersed in a fluid is buoyed up by a force equal to the weight of the fluid that is displaced. It is determined by the following equation 18;

$$\rho_{mea} = \frac{W_1}{W_1 - W_2} \times \rho_w \quad (18)$$

Where ρ_{mea} denotes the measured density of the samples (g/cm^3).

W_1 denotes the dry weight of the samples (g).

W_2 denotes the weight immersed in the water of the samples (g).

ρ_w denotes the density of water for immersion the samples (g/cm^3).

Electrical properties

Dielectric measurement

The dielectric behaviors of the ceramics were evaluated at a frequency of 1, 10 and 100 kHz over a temperature range of 30-400°C. Figure 44 display the computer-controlled dielectric measurement system consists of an LCR-meter (Agilent 4263B), a temperature chamber and a computer system. The dielectric constant can be described by the following equation 19: (75, 76)

$$\varepsilon_r = \frac{Ct}{\varepsilon_0 A} \quad (19)$$

where ε_r represents the dielectric constant.

ε_0 represents the permittivity of free space.

C represents the capacitance.

t represents the thickness of the ceramics.

A represents the area of the ceramics.



Figure 44 The LCR meter at Naresuan University.

Ferroelectric properties measurements

The ferroelectric hysteresis loops (P - E) of samples were carried out at room temperature and frequency of 1 Hz using a computer controlled modified Sawyer Tower circuit (Radiant, PLC2-1014346), which was measured under electrical field of 40-45 kV/cm. Figure 45 display the computer controlled modified Sawyer Tower circuit (77-79).



Figure 45 The computer controlled modified Sawyer Tower circuit.

CHAPTER IV

RESULTS AND DISCUSSION

1. Effect of firing conditions on phase formation, microstructure, and electrical properties of $(\text{K}_{0.5}\text{Na}_{0.5})(\text{Nb}_{0.7}\text{Ta}_{0.3})\text{O}_3$ ceramics synthesized by solid-state combustion method

Figure 46 presents the X-ray diffraction pattern revealing the phase content of the KNNT powders after calcination at temperatures in the range from 600°C to 800°C for 2 h. It was found that all the samples exhibited pure perovskite structure resembling Joint Committee on Powder Diffraction Standards (JCPDS) files no. 01-071-0946 (orthorhombic phase) and 01-071-0945 (tetragonal phase). For comparison, the pure perovskite phase was obtained from the samples calcined at 600°C for 2 h, which is 300°C less than that reported for the solid-state reaction technique, which used 900°C and 3 h (10). This reduction in temperature and time is a result of the liquid medium, when glycine melts, and the energy released from the combustion of glycine (80).

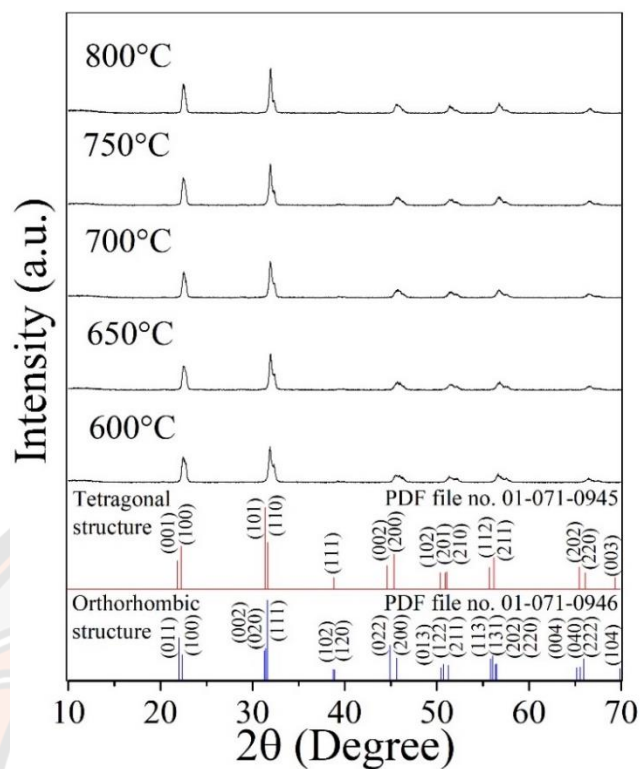


Figure 46 X-ray diffraction patterns of KNNT powders calcined at temperatures between 600 and 800°C for 2 h in the 2θ range of 10-70°.

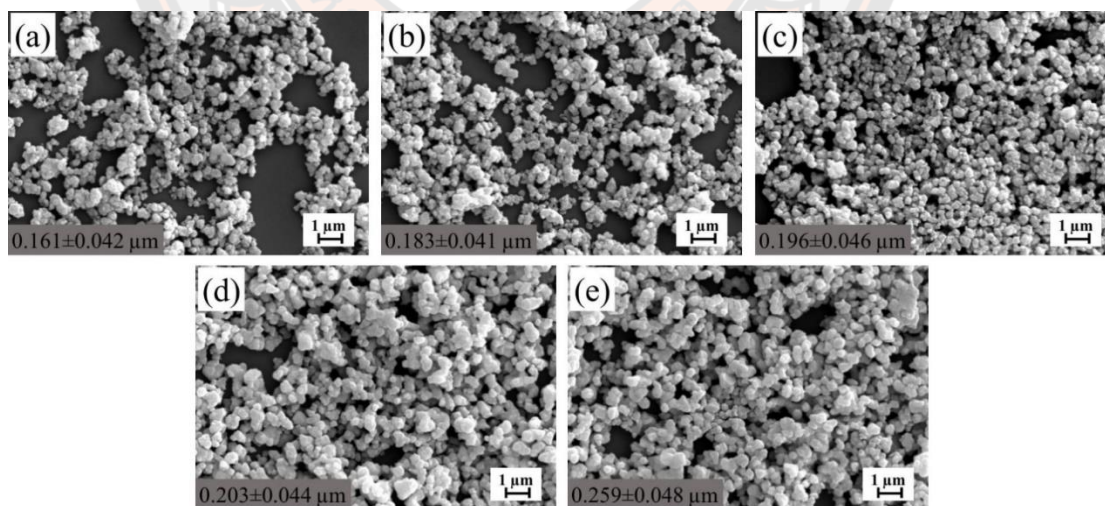


Figure 47 SEM images of KNNT powders calcined at the temperatures of: (a) 600, (b) 650, (c) 700, (d) 750 and (e) 800°C for 2 h.

Figure 47 (a-e) shows SEM images of the KNNT powders calcined at different temperatures between 600 and 800°C for 2 h. It was observed that all the calcined KNNT powders exhibited fine particles and rather spherical morphology. The particle agglomerations in the powders increased when the calcination temperature was increased (Figure 47 (a-e)). The average particle size of the KNNT powders increased from 0.161 ± 0.042 to 0.259 ± 0.048 μm when the calcination temperature was increased from 600 to 800°C. The morphology and crystallinity of the powder calcined at 600°C for 2 h were studied by TEM (Figure 48 (a-d)). Figure 48 (a) shows a TEM image at low magnification, where thickly agglomerated particles can be observed. At high magnification (Figure 48 (b)), rather square shapes were revealed, and particle sizes of ~ 160 nm could be measured. This value is close to the particle size measured by SEM. Figure 48 (c) shows the selected-area electron diffraction (SAED) pattern, revealing spotty ring patterns that indicate a polycrystalline character (81). The ring patterns observed by SAED demonstrate the coexistence of orthorhombic and tetragonal phases, in correspondence with the XRD results described above.

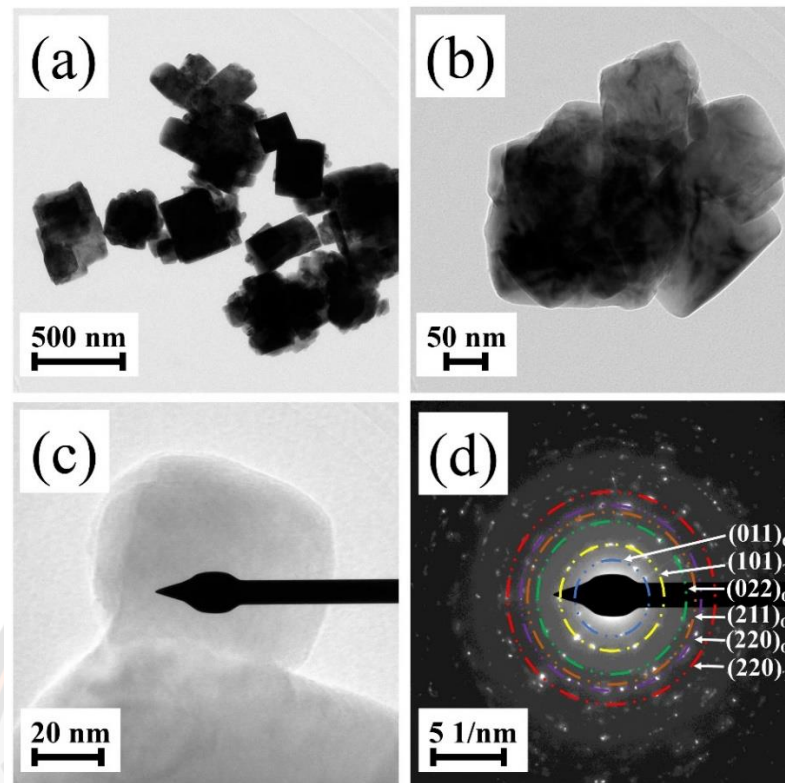


Figure 48 (a-c) TEM micrograph and (d) SAED pattern of KNNT powders calcined at temperature of 600°C for 2 h.

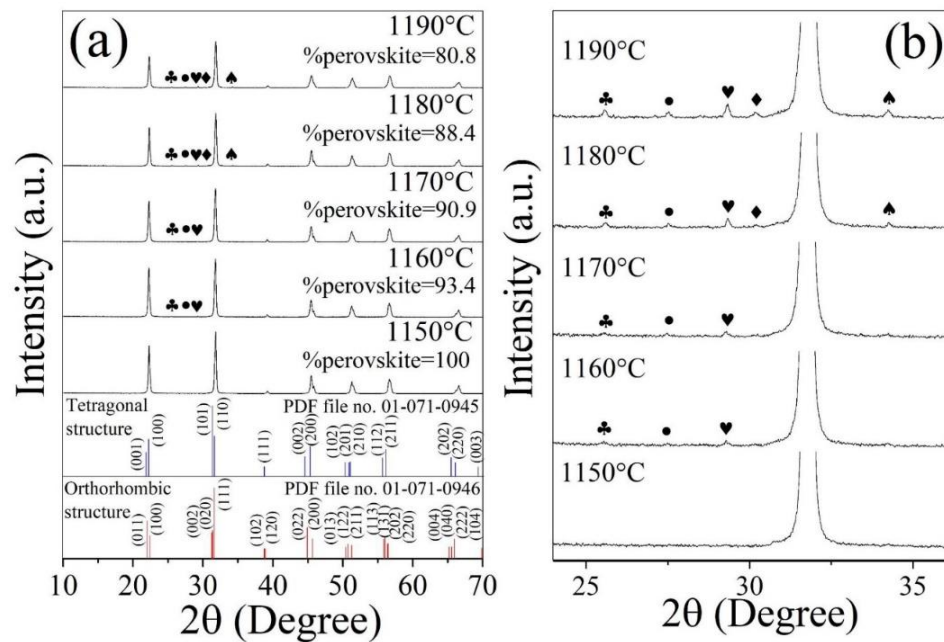


Figure 49 X-ray diffraction patterns of KNNT ceramics with various sintering temperatures in the 2θ range of (a) 10-70° and (b) 24-36°; filled club, Nb_2O_5 ; filled circle, KNO_3 ; filled heart, KO_2 ; filled diamond, NaNO_2 ; filled spade, KNaO .

The XRD patterns of the ceramics sintered at temperatures between 1150 and 1190°C for 2 h are shown in Figure 49 (a-b). A pure perovskite structure in the KNNT ceramics was obtained after sintering at 1150°C for 2 h. After sintering at temperatures >1150°C for 2 h, secondary phases such as Nb_2O_5 , KNO_3 , and KO_2 were detected. After sintering at 1180 and 1190°C for 2 h, impurity peaks corresponding to NaNO_2 and KNaO also appeared. The quantity of perovskite phase was defined by measuring the major XRD peak intensity for the perovskite structure. The percentage purity of the perovskite structure in the sintered KNNT ceramics was calculated using Eq. 20,

$$\text{Perovskite} = \left(\frac{I_{\text{perov}}}{I_{\text{perov}} + I_{\text{Nb}_2\text{O}_5} + I_{\text{KNO}_3} + I_{\text{KO}_2} + I_{\text{NaNO}_2} + I_{\text{KNaO}}} \right) \times 100 \quad (20)$$

This equation can be used to compute the purity percentage of the perovskite-structured materials, (82, 83) where I_{perov} is the maximum intensity of the perovskite peak and $I_{\text{Nb}_2\text{O}_5}$, I_{KNO_3} , I_{KO_2} , I_{NaNO_2} , and I_{KNaO} are the highest-intensity peaks of the impurities. The perovskite percentage of all the sintered KNNT ceramics is presented in Figure 49 (a). The presence of impurity phases after sintering at temperatures $>1150^\circ\text{C}$ can be explained by the volatilization of Na_2O and K_2O during the sintering process (84, 85). Moreover, previous research has reported that different dwell times affect the densification, microstructure, and electric properties of ceramics (86, 87). It may thus be essential to examine the effect of dwell time during sintering on the density value, microstructure, and electrical properties of the ceramics with a sintering temperature of 1150°C .

Figure 50 shows the room-temperature XRD patterns in the 2θ range of 10° to 70° for all the ceramics sintered at 1150°C with different dwell times. All the ceramics possessed pure perovskite structure, and no secondary impurity could be detected. The phase structure of all the ceramics corresponded to JCPDS files no. 01-071-0946 (orthorhombic phase) and 01-071-0945 (tetragonal phase), in accordance with previous reports (9).

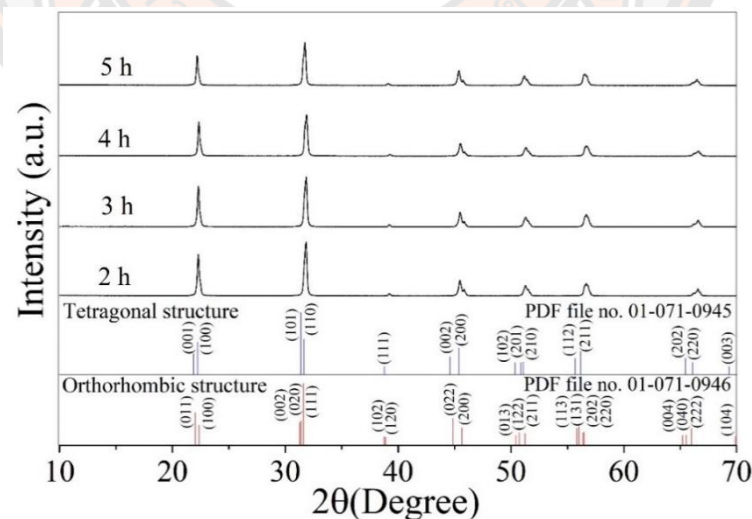


Figure 50 X-ray diffraction patterns of KNNT ceramics at a sintering temperature of 1150°C for the different dwell times of 2-5 h in the 2θ range of $10-70^\circ$.

Table 3 Goodness of fit parameters, lattice parameters, atomic information and the percentage of phases for KNNT ceramics with different dwell times during sintering.

Dwell time (h)	Goodness of fit	Phase structures	Profile parameters	Atoms information					The percentage of phase					
				Label	x	y	z	Occ.						
2	$\chi^2=2.15$ $R_p=13.8\%$ $R_w=14.8\%$ $R_{exp}=10.07\%$	<i>Amm2</i>	$a=3.954 \text{ \AA}$	Na	0	0	0.0453	0.60479	68					
			$b=5.626 \text{ \AA}$	K	0	0	0.0453	0.50137						
			$c=5.645 \text{ \AA}$	Nb	0.5	0	0.5251	0.61646						
			$u=0.011$	Ta	0.5	0	0.5251	0.30270						
			$v=0.024$	O1	0	0	0.4727	1.22985						
			$w=0.009$	O2	0.5	0.7535	0.2285	1.03943						
			$a=3.990 \text{ \AA}$	Na	0	0	0	0.45192						
		<i>P4mm</i>	$c=3.965 \text{ \AA}$	K	0	0	0	0.49912		32				
			$c/a=0.993$	Nb	0.5	0.5	0.492	0.64531						
			$u=0.508$	Ta	0.5	0.5	0.492	0.30086						
			$v=-0.168$	O1	0.5	0.5	0.038	1.21856						
			$w=0.072$	O2	0.5	0	0.539	2.30511						
			3	$\chi^2=2.05$ $R_p=14.0\%$ $R_w=14.9\%$ $R_{exp}=10.40\%$	<i>Amm2</i>	$a=3.956 \text{ \AA}$	Na	0			0	0.0453	0.59231	58
						$b=5.628 \text{ \AA}$	K	0			0	0.0453	0.63951	
$c=5.647 \text{ \AA}$	Nb	0.5				0	0.5251	0.60684						
$u=0.012$	Ta	0.5				0	0.5251	0.24258						
$v=0.021$	O1	0				0	0.4727	1.17772						
$w=0.010$	O2	0.5				0.7535	0.2285	1.28250						
$a=3.996 \text{ \AA}$	Na	0				0	0	0.42083						
<i>P4mm</i>	$c=3.974 \text{ \AA}$	K			0	0	0	0.49908	42					
	$c/a=0.994$	Nb			0.5	0.5	0.492	0.65182						
	$u=0.524$	Ta			0.5	0.5	0.492	0.24041						
	$v=-0.242$	O1			0.5	0.5	0.038	2.10799						
	$w=0.071$	O2			0.5	0	0.539	2.73110						
	4	$\chi^2=2.52$ $R_p=16.2\%$ $R_w=17.9\%$ $R_{exp}=11.26\%$			<i>Amm2</i>	$a=3.958 \text{ \AA}$	Na	0		0	0.0453	0.60479	50	
						$b=5.646 \text{ \AA}$	K	0		0	0.0453	0.50137		
$c=5.644 \text{ \AA}$			Nb	0.5		0	0.5251	0.64397						
$u=0.018$			Ta	0.5		0	0.5251	0.27500						
$v=0.092$			O1	0		0	0.4727	1.27997						
$w=0.002$			O2	0.5		0.7535	0.2285	1.64498						
$a=3.984 \text{ \AA}$			Na	0		0	0	0.45192						
<i>P4mm</i>			$c=3.987 \text{ \AA}$	K	0	0	0	0.49912	50					
			$c/a=1.000$	Nb	0.5	0.5	0.492	0.80114						
			$u=0.388$	Ta	0.5	0.5	0.492	0.31699						
			$v=0.233$	O1	0.5	0.5	0.038	2.18147						
			$w=0.102$	O2	0.5	0	0.539	1.07654						

5	$\chi^2=2.02$	<i>Amm2</i>	$a=3.953 \text{ \AA}$	Na	0	0	0.0453	0.66039	79
	$R_p=16.6\%$		$b=5.630 \text{ \AA}$	K	0	0	0.0453	0.53941	
	$R_w=15.9\%$		$c=5.640 \text{ \AA}$	Nb	0.5	0	0.5251	0.57574	
	$R_{exp}=11.17\%$		$u=0.076$	Ta	0.5	0	0.5251	0.29641	
			$v=0.053$	O1	0	0	0.4727	1.07713	
			$w=0.003$	O2	0.5	0.7535	0.2285	2.26191	
		<i>P4mm</i>	$a=3.997 \text{ \AA}$	Na	0	0	0	0.59858	21
			$c=3.962 \text{ \AA}$	K	0	0	0	0.59284	
			$c/a=0.991$	Nb	0.5	0.5	0.492	0.62353	
			$u=0.442$	Ta	0.5	0.5	0.492	0.20655	
			$v=-0.374$	O1	0.5	0.5	0.038	1.98580	
			$w=0.092$	O2	0.5	0	0.539	1.45685	

To confirm and complete the XRD analyses, Rietveld refinement was performed on all the ceramics to analyze the ratio of the *O* and *T* phases by fitting the XRD data using the FullProf program. The initial values of the cell parameters, lattice constants, space group, and atom functional positions were taken from corresponding reference patterns calculated from the Crystallography Open Database (COD). A structural model based on KaNbNbO_3 in tetragonal phase and space group *P4mm* and orthorhombic phase in space group *Amm2* were used as starting models for refining the XRD data of the KNNT ceramics. The background was fit using a Chebyshev polynomial function, and the peak shape was described by a pseudo-Voigt function, (67) which is a linear combination of Lorentzian and Gaussian functions. To judge the quality of fit of the refinement, various parameters were calculated, including the profile reliability R_p , the weighed pattern reliability R_{wp} , the expected residual R_{exp} , and the goodness of fit χ^2 . Figure 51 (a)-(d) shows the Rietveld refinement of the XRD patterns of all the KNNT ceramics in the 2-5 h range from 10 to 70°. As presented in Figure 51 (a)-(d), observational data (I_{obs}) is defined by red hollow symbol, calculated pattern (I_{cal}) is defined black solid line and different between (I_{obs}) and (I_{cal}) is defined by blue solid line. The quality of the fits was calculated as $R_p \leq 16.6\%$, $R_{wp} \leq 17.9\%$, $R_{exp} \leq 11.26\%$, and $\chi^2 \leq 2.52$, indicating good agreement between the observed and calculated intensity profiles of all the ceramics. The fitting results confirm that all the ceramics had two phases in coexistence, the orthorhombic and tetragonal phases. Table 3 presents the goodness-of-fit parameters, lattice parameters, atomic information, and percentage of each phase for all the ceramics sintered with different dwell times. The *O:T* ratio results reveal an increase of the

tetragonal phase and a decrease in the orthorhombic phase with increasing dwell time from 2 to 4 h. When using a dwell time of 4 h, the $O:T$ ratio was 50:50. The phase fraction obtained in this ceramic lies in the morphotropic phase boundary (MPB) zone, which is crucial to achieve good electrical properties.

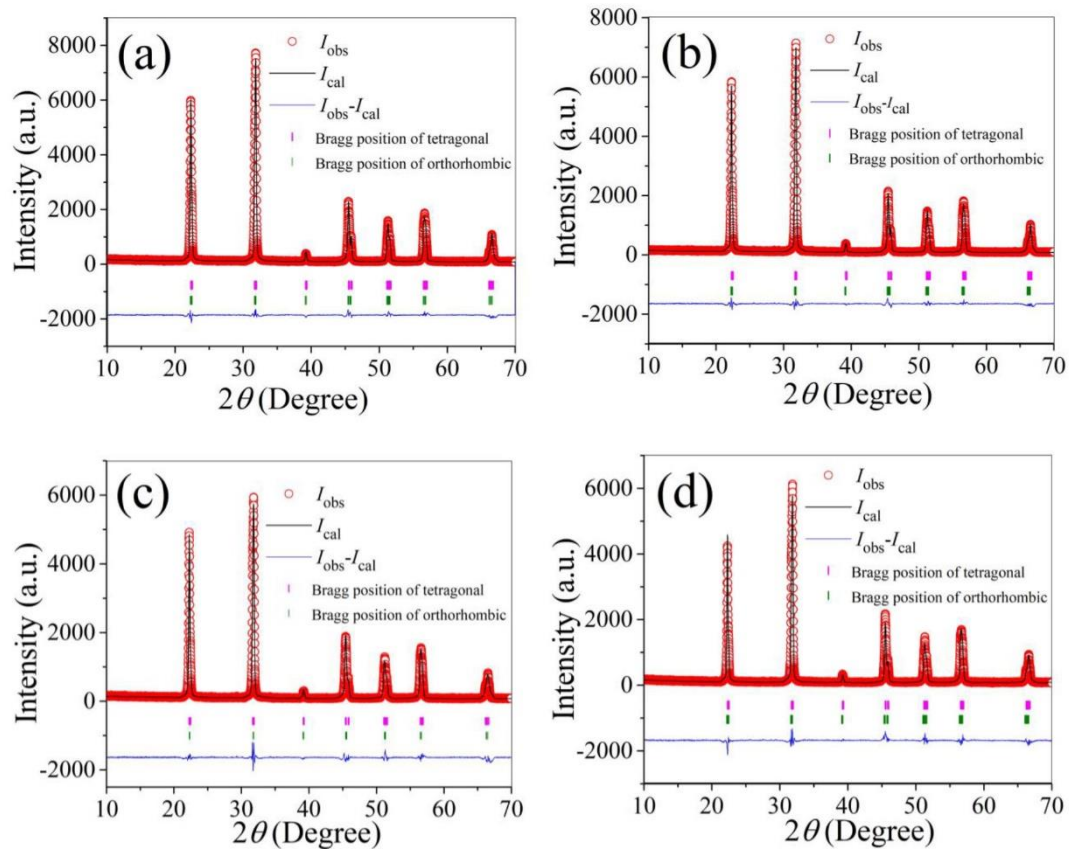


Figure 51 Typical Rietveld refinement analysis for KNNT ceramics at different dwell times: (a) 2, (b) 3, (c) 4 and (d) 5 h.

Figure 52 (a-d) presents the XPS spectra in the binding energy range from 0 to 1200 eV for the KNNT ceramics obtained using different dwell times. The standard C 1s signal (~ 285.0 eV) was applied to calibrate all the binding energies. The survey XPS spectrum shown in Figure 52 (a) reveals that all the ceramics were composed of K, Na, Nb, Ta, and O, confirming that KNNT ceramics were obtained. The high-resolution Nb 3d spectra for all samples (Figure 52) consisted of two wide peaks of Nb 3d_{5/2} and Nb 3d_{3/2}, corresponding to binding energy of ~ 209.67 and ~ 206.94 eV,

respectively. The structural splitting distance for all the compositions was ~ 2.73 eV, while the ratio of the Nb $3d_{5/2}$ to Nb $3d_{3/2}$ peak areas was ~ 1.53 , indicating Nb⁵⁺ (88, 89). Figure 52 (c) shows the high-resolution Ta $4f$ spectrum for all the samples. Two major characterized peaks corresponding to Ta $4f_{5/2}$ and Ta $4f_{7/2}$ were found at binding energy of ~ 27.63 eV and ~ 25.75 eV, respectively. The structural splitting distance for all the compositions was ~ 1.88 eV, and the ratio of the Ta $4f_{7/2}$ and Ta $4f_{5/2}$ peak areas was ~ 1.16 , corresponding to Ta⁵⁺ (89, 90). These results provide evidence that the use of different dwell times did not change the valence states of the constituent elements of the KNNT ceramics. Next, the high-resolution O $1s$ spectra of all the samples are shown in Figure 52 (d), being fit with three peaks at binding energy of ~ 529.88 eV, ~ 531.62 eV, and ~ 533.52 eV, attributed to lattice oxygen (Nb-O), oxygen vacancies, and absorbed H₂O, respectively (89, 91). Moreover, the concentration of oxygen vacancies for all the compositions was calculated from the area ratio $II/(I + II + III)$ of the three peaks *I*, *II*, and *III* (Figure 52 (d)), (89, 92) yielding values of 33, 20, 25, and 29% for the dwell times of 2, 3, 4, and 5 h, respectively. The formation of oxygen vacancies can be explained by the volatilization of alkali-metal ions (positive charges) from the KNNT ceramics during sintering, leading to loss of oxygen (negatively charged ions) to maintain charge neutrality (93).

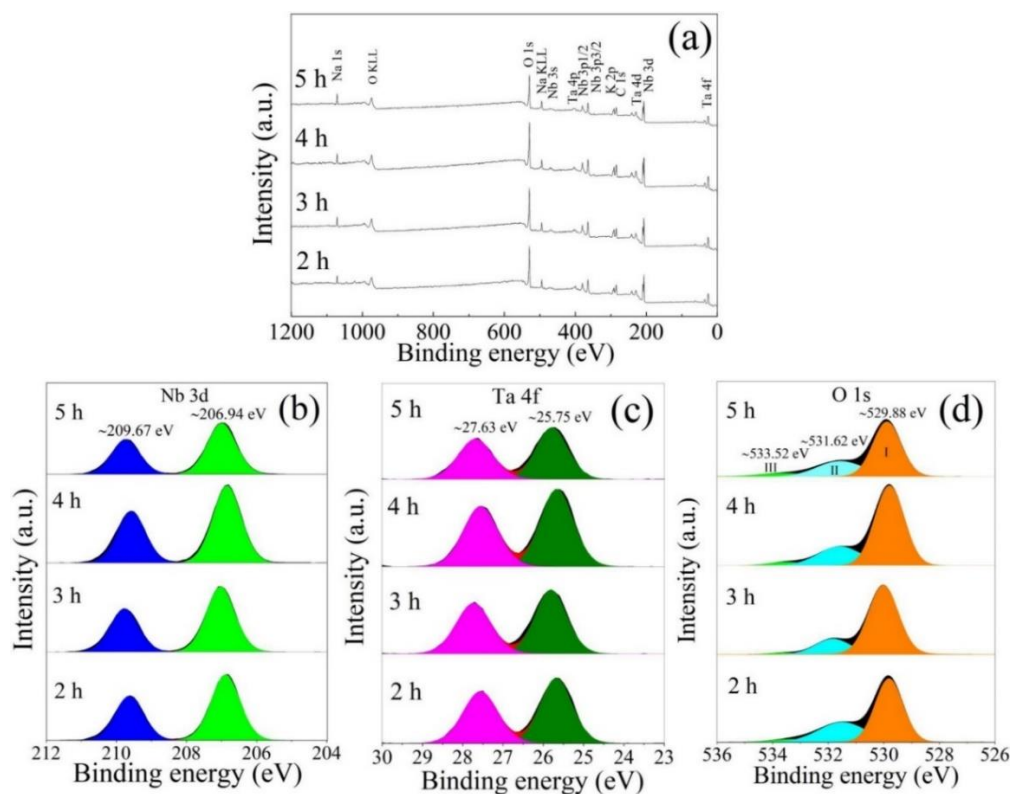


Figure 52 (a) The wide-range, high-resolution XPS spectrum of (b) Nb 3d, (c) Ta 4f, and (d) O 1s of KNNT ceramics as a function of dwell times.

Table 4 The ratio of all element spectrums of the KNNT ceramics with different dwell times.

Dwell time	Element (wt.%)						
	(h)	C	O	Na	Ta	Nb and Au	K
2		03.41	09.68	04.39	35.23	40.28	07.00
3		03.55	08.27	03.93	33.94	42.89	07.42
4		03.88	09.14	03.89	36.56	39.53	07.00
5		02.51	08.14	03.88	33.29	44.84	07.33

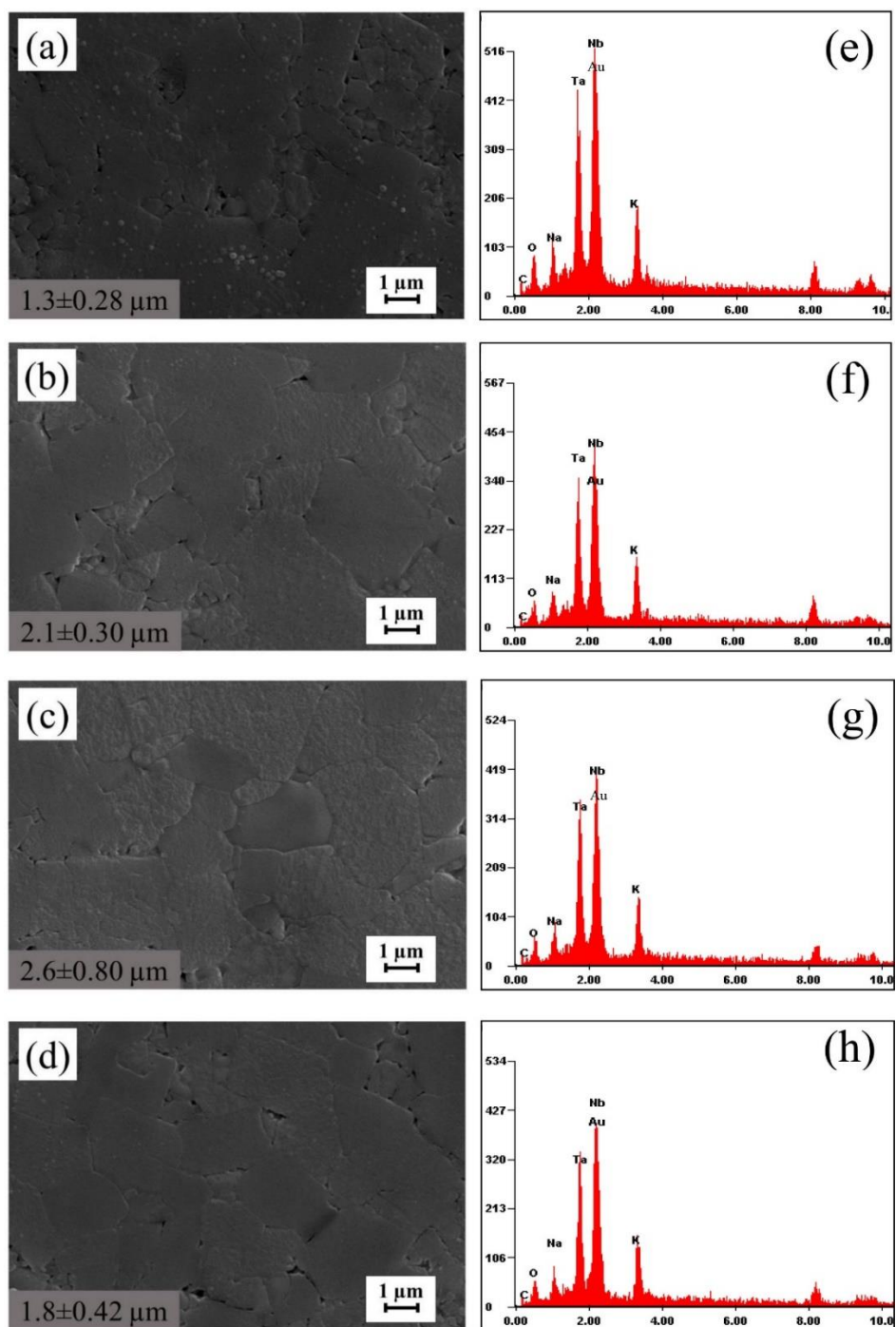


Figure 53 SEM images and EDS spectrums of KNNT ceramics sintered at 1150°C for different dwell times: (a), (e) 2 h, (b), (f) 3 h, (c), (g) 4 h and (d), (h) 5 h.

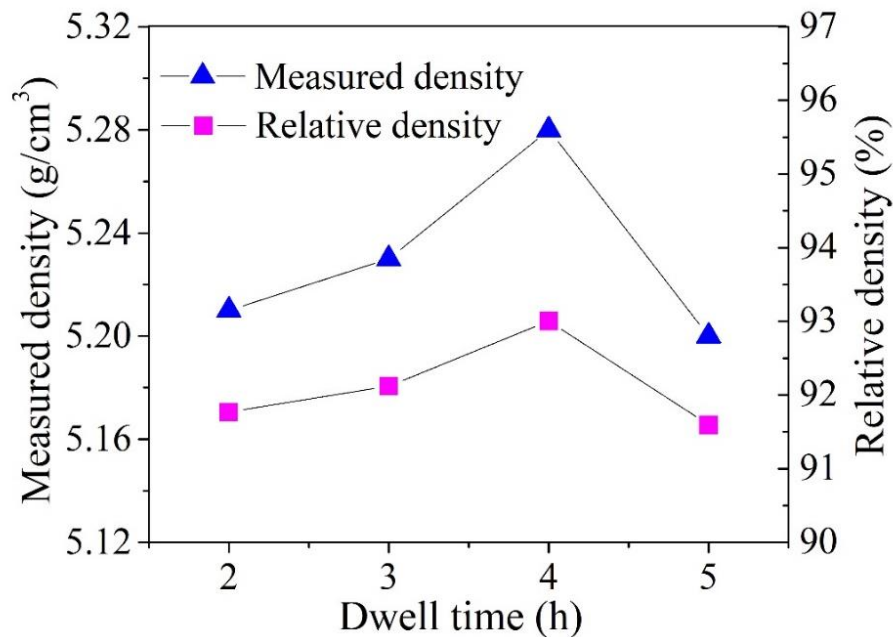


Figure 54 The measured and relative density of KNNT ceramics at a sintering temperature of 1150°C for the different dwell times.

SEM images of the KNNT ceramics obtained using different dwell times are shown in Figure 53 (a-d). The grains of all the ceramics showed irregular polyhedron shape, and the grain growth tended to be anisotropic. The average grain size of the ceramics gradually increased from 1.3 ± 0.28 to 2.6 ± 0.80 μm with increasing dwell time from 2 to 4 h but then dropped, as shown in Figure 53. On the other hand, the porosity tended to decrease when the dwell time was increased from 2 to 4 h but then started to increase (Figure 53 (a-d)). Figure 53 (e-h) shows the energy-dispersive spectrometry (EDS) spectra of the KNNT ceramics obtained using different dwell times. C, O, Na, Ta, Nb, K, and Au elements were detected in all the ceramics. The Au signal resulted from the sample coating process applied for EDS. Table 4 presents the amount of each element calculated from their spectra for the KNNT ceramics obtained using different dwell times. Note that the quantity of Na continuously decreased as the dwell time was increased, while the other elements fluctuated but showed no upward or downward trend. Figure 54 shows the measured and relative density of the KNNT ceramics as a function of dwell time. Both values continuously increased with increasing dwell time from 2 to 4 h but then dropped. When using a

dwel time of 4 h, the ceramics exhibited the highest measured density and relative density of 5.28 g/cm³ and 93.0%, respectively. It is well known that an optimal amount of oxygen vacancies and decreasing the number of pores leads to enhanced mass transport, resulting in increased grain size and density of the ceramics. The decrease in the average grain size and the density can be explained by the increase in the amount of pores, which hinder mass transfer and densification during the sintering process (94). For comparison, the density values of the KNNT ceramics (sintered at 1150°C for 4 h) obtained by this method are higher than values reported for hydrothermal approaches (90.5%) (50). The density results for the ceramics corresponded well with the SEM results.

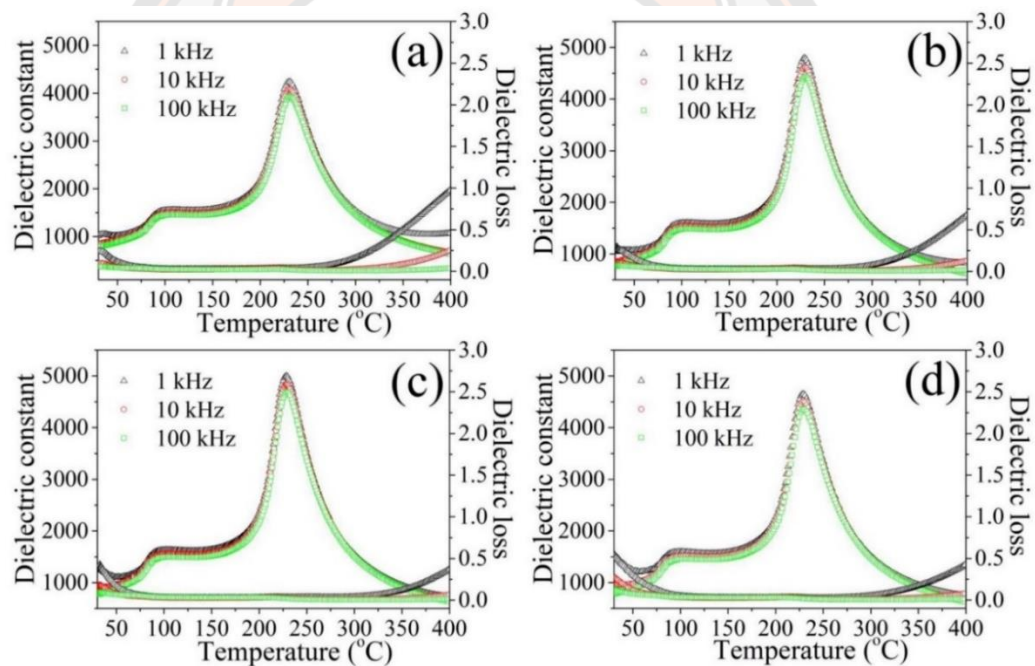


Figure 55 Temperature dependent of the dielectric constant and loss of KNNT ceramics at a sintering temperature of 1150°C for the different dwell times: (a) 2, (b) 3, (c) 4 and (d) 5 h.

Figure 55 (a-d) shows the temperature dependence of the dielectric constant and dielectric loss for the KNNT ceramics obtained using different dwell times, measured in the temperature range from 30 to 400°C and at frequencies of 1, 10, and 100 kHz. A frequency-independent response was observed for all the ceramics. Note

that all the ceramics displayed two obvious phase-transition peaks above room temperature, corresponding to the orthorhombic-tetragonal ferroelectric phase transition (T_{O-T}) and tetragonal-cubic paraelectric phase transition (T_C), respectively. The T_{O-T} and T_C values for the ceramics decreased from 94 to 89°C and from 230 to 228°C as the dwell time was increased, as seen in Table 5. The reduction of T_{O-T} and T_C can be explained by distortions in the structure, corresponding to previous reports (95). The dielectric constant at room temperature (ϵ_R) rise from 1041 to 1512 with increasing dwell time (Table 5). For, the dielectric constant at Curie temperature (ϵ_C) increased from 4237 to 5002 on increasing the dwell time from 1 to 4 h but then decreased for the dwell time of 5 h (Table 5). The values of the dielectric loss ($\tan \delta$) at room temperature (T_R) and at the Curie temperature (T_C) are presented in Table 5. When using a dwell time of 4 h, the KNNT ceramics showed the highest dielectric constant ($\epsilon_C = 5002$) and low dielectric loss ($\tan \delta$ at $T_R = 0.032$ and $\tan \delta$ at $T_C = 0.035$). This result may be explained by the large grain size, which increases the domain size and facilitates domain wall motion, (96) resulting in an increased dielectric constant for the KNNT ceramics obtained with a dwell time of 4 h. On the other hand, when the grain size becomes smaller, the grain boundaries thicken and the surface charge compensation layer increases, leading to a decrease of the dielectric constant (96, 97).

A modified Curie-Weiss law is proposed herein to explain the diffuseness of the ferroelectric phase transition (98) according to Eq. 21:

$$\frac{1}{\epsilon} - \frac{1}{\epsilon_C} = (T - T_C)^\gamma / C \quad (21)$$

where ϵ is the temperature-dependent dielectric constant, C is a Curie-like coefficient, and γ is the degree of diffuseness, having a value in the range from 1 to 2; $\gamma = 1$ represents a normal ferroelectric whereas $\gamma = 2$ describes a completely diffuse phase transition (98). The slopes of the fit curves of $\ln(1/\epsilon - 1/\epsilon_C)$ versus $\ln(T - T_C)$ at 1 kHz for the ceramics obtained using each dwell time were used to calculate the γ values, as shown in Figure 56 (a-d). The γ values gradually increased from 1.550 to 1.655 with increasing dwell time (Figure 56), suggesting that the phase transition of these

ceramics becomes more diffuse with increasing dwell time. The increase of the diffuseness of the phase transition in the samples may be caused by an increase in lattice disorder.

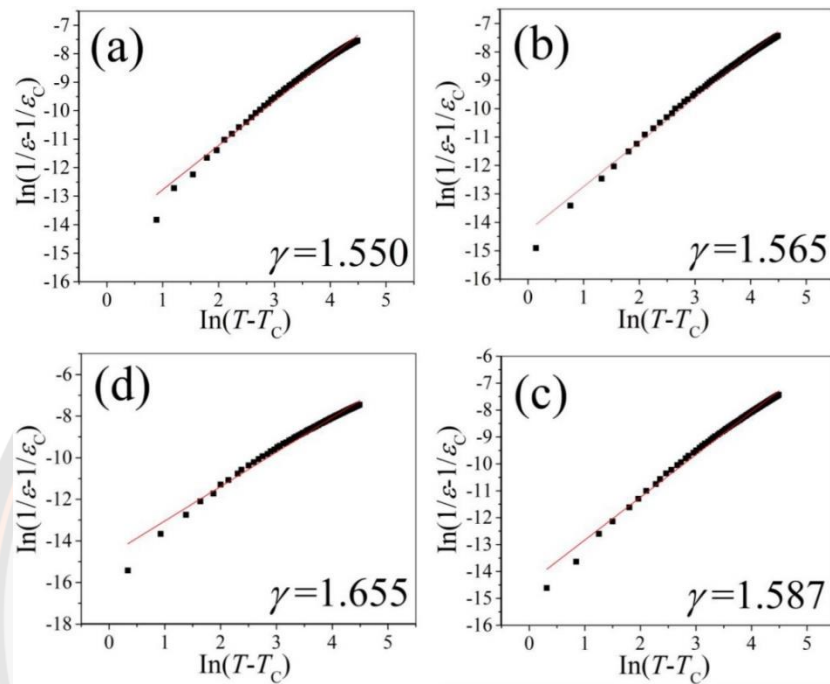


Figure 56 The plot of $\ln(1/\varepsilon - 1/\varepsilon_C)$ versus $\ln(T - T_C)$ at 1 kHz for the KNNT ceramics at a sintering temperature of 1150°C for the different dwell times: (a) 2, (b) 3, (c) 4 and (d) 5 h.

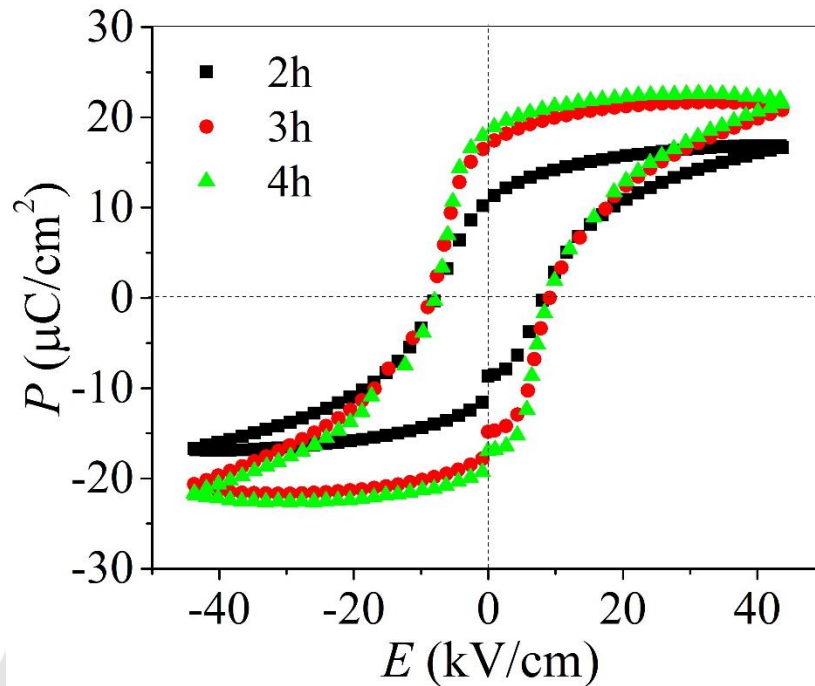


Figure 57 Polarization versus electric field (P - E) loops at room temperature for KNNT ceramics at a sintering temperature of 1150°C for 2-4 h.

Table 5 Dielectric and ferroelectric properties of the KNNT ceramics sintered at 1150°C with the different dwell times.

Dwell time (h)	T_{O-T} ($^{\circ}\text{C}$)	T_C ($^{\circ}\text{C}$)	$\tan \delta$ at		P_r ($\mu\text{C}/\text{cm}^2$)	E_C (kV/cm)	R_{sq}		
			ϵ_R	ϵ_C				T_R	T_C
2	94	230	1041	4237	0.030	0.038	10.81	8.07	0.78
3	92	229	1132	4786	0.037	0.035	17.00	9.13	0.91
4	91	228	1305	5002	0.032	0.035	18.50	9.04	0.96
5	89	228	1512	4654	0.068	0.029	-	-	-

Figure 57 shows the polarization-electric field (P - E) hysteresis loops of the KNNT ceramics obtained using different dwell times, measured under an electrical field of $45\text{ kV}/\text{cm}$ and at a frequency of 1 Hz . Saturated P - E hysteresis loops were found for all the KNNT ceramics. It is seen that, with increasing dwell time, the P_r values increased from 10.81 to $18.50\ \mu\text{C}/\text{cm}^2$, while the E_C values changed only slightly. The remnant polarization (P_r) and coercive field (E_C) are presented as

functions of dwell time in Table 5. The increase of P_r at the dwell time of 4 h can be attributed to reaching the MPB and it's having the largest grain size, which makes the ferroelectric domains rotate more easily (99, 100). However, the ceramic obtained using a dwell time of 5 h could not be measured. This was mainly due to the high leakage current due to the porous microstructure and low density (101).

To analyze the ferroelectric characteristics of the KNNT ceramics, the degree of squareness (R_{sq}) of the P - E loops (102) was calculated using Eq. 22:

$$R_{sq} = \frac{P_r}{P_s} + \frac{P_{1.1E_c}}{P_r} \quad (22)$$

where P_s is the saturation polarization and $P_{1.1EC}$ is the polarization corresponding to $1.1E_c$. Theoretically, R_{sq} should be equal to 2. This ideal R_{sq} value indicates better homogeneity, uniformity in grain size, and good switching behavior of the ceramics (102). In this work, the R_{sq} values increased when the dwell time was increased, as seen in Table 5. The highest R_{sq} value of 0.96 was obtained for the ceramics with a dwell time of 4 h, suggesting that the use of an optimum dwell time during sintering can improve the microstructure and electrical properties of KNNT ceramics. According to the discussion above, the KNNT ceramics obtained using the optimum firing condition (1150°C for 4 h) exhibited good electrical performance. This phenomenon can be attributed to two main factors. First, the occurrence of a morphotropic phase boundary (MPB) zone of coexisting $O + T$ phases at a ratio of $O:T$ of 50:50, resulting in instability of the polarization state, so the polarization direction can be easily rotated by an electric field. Second, this ceramic had a well-developed microstructure, the highest density, and large grain size, which enhance the domain variants, while the trapped space charges at grain boundaries were reduced (14). The deterioration of the electrical properties of the ceramics produced under the other conditions was caused by low density and porous structures forming at grain boundaries, leading to high electrical conductivity.

2. The influences of Cs⁺ substitution and direct doping on the phase evolution, microstructure and electrical properties of KNNT ceramics

Figure 58 shows the XRD patterns of the $K_{0.5-x}Cs_xNNT$ (Figure 58 a(I-III)) and $KNNT-xCs$ ceramics (Figure 58 b(I-III)). It can be observed that all compositions exhibited a pure perovskite phase and no trace of any secondary phase was detected. To determine the phase formation, the XRD patterns of all samples at 2θ around $\sim 39^\circ$ and $\sim 45^\circ$ were zoomed and shown in Figure 58 a(II-III) - b(II-III). Generally, an orthorhombic (O) structure (JCPDS file no 01-071-0946) exhibits characteristic of dual $(102)/(120)_O$ peaks around $\sim 39^\circ$ and dual $(022)/(200)_O$ peaks around $\sim 45^\circ$. In the case of a tetragonal (T) structure (JCPDS file no 01-071-0945), there is a characteristic of a single $(111)_T$ peak around $\sim 39^\circ$ and dual $(002)/(200)_T$ peaks around $\sim 45^\circ$. The undoped KNNT ceramic with $x=0$ showed a diffraction peak with a broad and non-symmetry peak around $\sim 39^\circ$ (Figure 58 a(II) - b(II)) and dual peaks around $\sim 45^\circ$ (Figure 58 a(III) - b(III)). Compared with the undoped KNNT ceramic, the ceramics with Cs⁺ had peaks that became more sharp and non-symmetrical around $\sim 39^\circ$ (Figure 58 a(II) - b(II)) and showed three peaks around $\sim 45^\circ$ (Figure 58 a(III) - b(III)) for both the $K_{0.5-x}Cs_xNNT$ and $KNNT-xCs$ ceramics with $x=0.01-0.04$. This indicated that the phase formation in all samples had coexisting O and T phases. Moreover, it can be seen that the diffraction peaks at $\sim 39^\circ$ and $\sim 45^\circ$ of $K_{0.5-x}Cs_xNNT$ ceramics moving slightly to lower 2θ angles with increasing x doping (Figure 58 a(II-III)), because of the substitution of K⁺ (ionic radius 1.64 Å) by the larger Cs⁺ (ionic radius 1.88 Å) in the ABO_3 structure lead to expansion of the crystal lattice (103, 104). While the $KNNT-xCs$ ceramics diffraction peaks at $\sim 39^\circ$ and $\sim 45^\circ$ moving to lower 2θ angles as the x content increased up to 0.01 (Figure 58 b(II-III)), and then returned to positions close to the peaks at $x=0$, indicating the limits of solubility of Cs⁺ in the KNNT lattice.

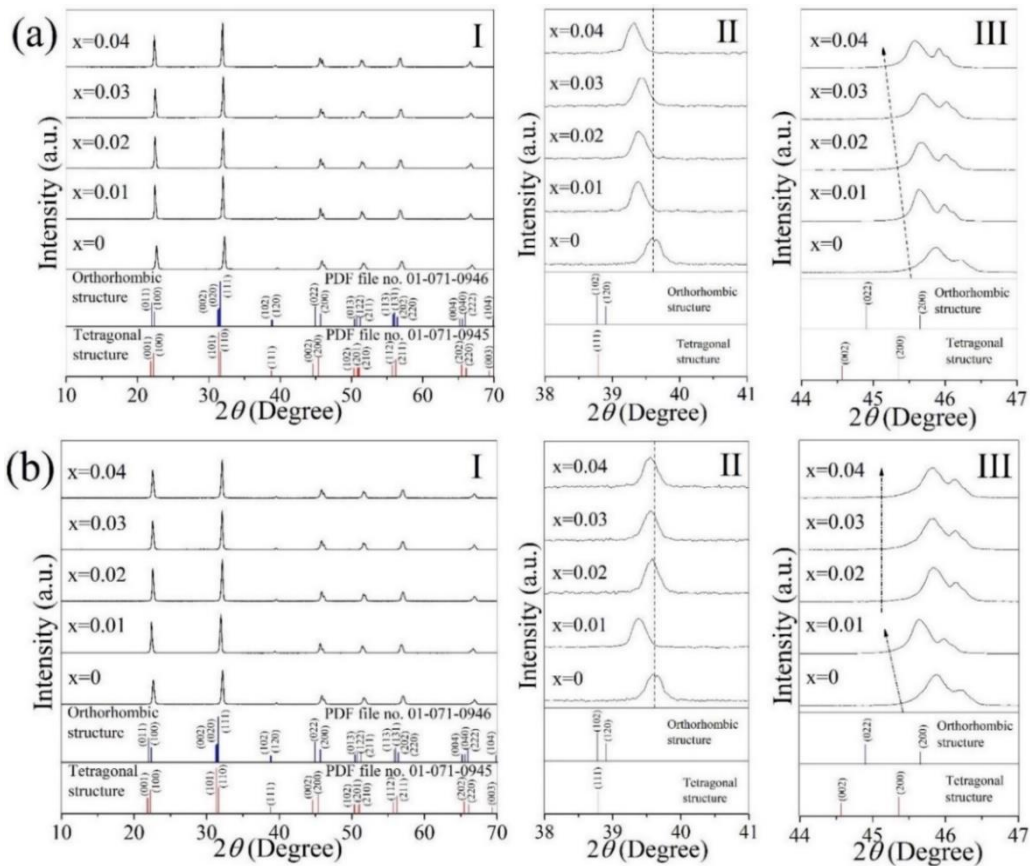
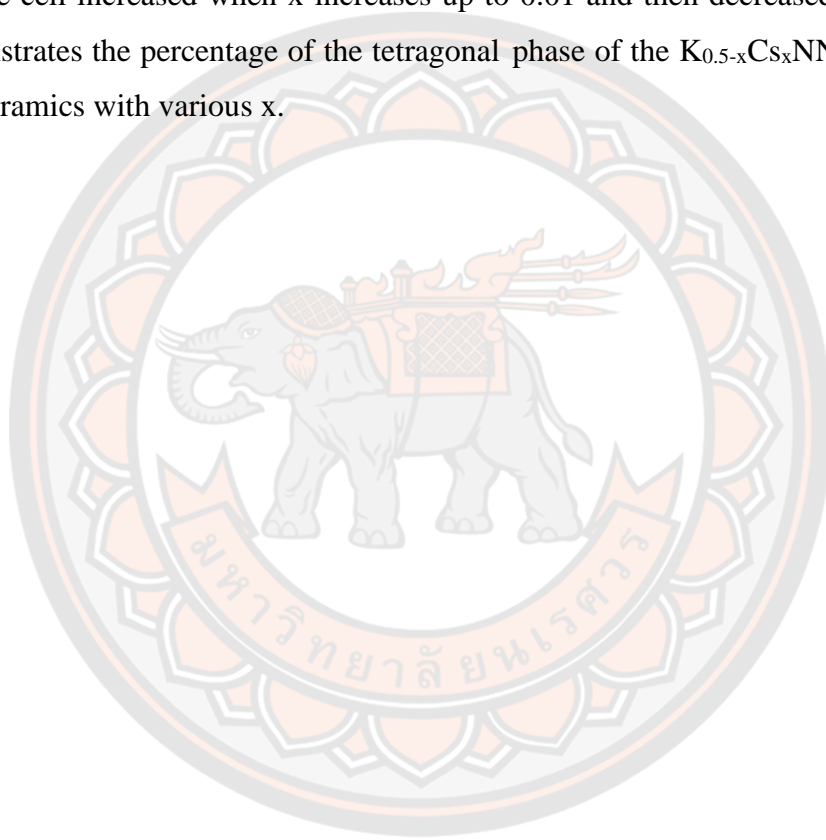


Figure 58 XRD patterns of the (a) $K_{0.5-x}Cs_xNNT$ and (b) $KNNT-xCs$ ceramics with different x .

In order to confirm and complete the XRD analyses, Rietveld refinement was performed on all the ceramics by fitting the XRD data with the Fullprof program. The initial values of the cell parameters, lattice constants, space group and atom functional positions were taken from the corresponding reference patterns calculated from the Crystallography Open Database (COD). A structural model based on $KaNbO_3$ with a tetragonal phase (T), with a $P4mm$ space group, and an orthorhombic phase (O), with an $Amm2$ space group, were used as the starting models for refining the $K_{0.5-x}Cs_xNNT$ and $KNNT-xCs$ ceramics' XRD data. The examples of the final output from the Rietveld refinement are displayed in Figure 59 (a)-(e). As presented in Figure 59 (a)-(e), observational data (I_{obs}) is defined by red hollow symbol, calculated pattern (I_{cal}) is defined black solid line and different between (I_{obs}) and (I_{cal}) is defined by blue solid line. It was found that the calculated quality of the fits were $R_p \leq 12.10\%$,

$R_{wp} \leq 12.90\%$, $R_{exp} \leq 7.99\%$ and $\chi^2 \leq 2.72$ (Table 6), suggesting fine agreement between the observed and refined intensity profiles for all compositions. The fitting outcome approved that all ceramics include coexisting *O* and *T* phases. For both the $K_{0.5-x}Cs_xNNT$ and $KNNT-xCs$ ceramics, the proportion of *O*:*T* showed an increase of the *O* while the *T* reduced with rising *x*. The volume cell and phase percentage of all compositions are listed in Table 6. The average volume cell of $K_{0.5-x}Cs_xNNT$ ceramics tends to increase when increasing *x*. While for the $KNNT-xCs$ ceramics, the average volume cell increased when *x* increases up to 0.01 and then decreased. Figure 59 (f) demonstrates the percentage of the tetragonal phase of the $K_{0.5-x}Cs_xNNT$ and $KNNT-xCs$ ceramics with various *x*.



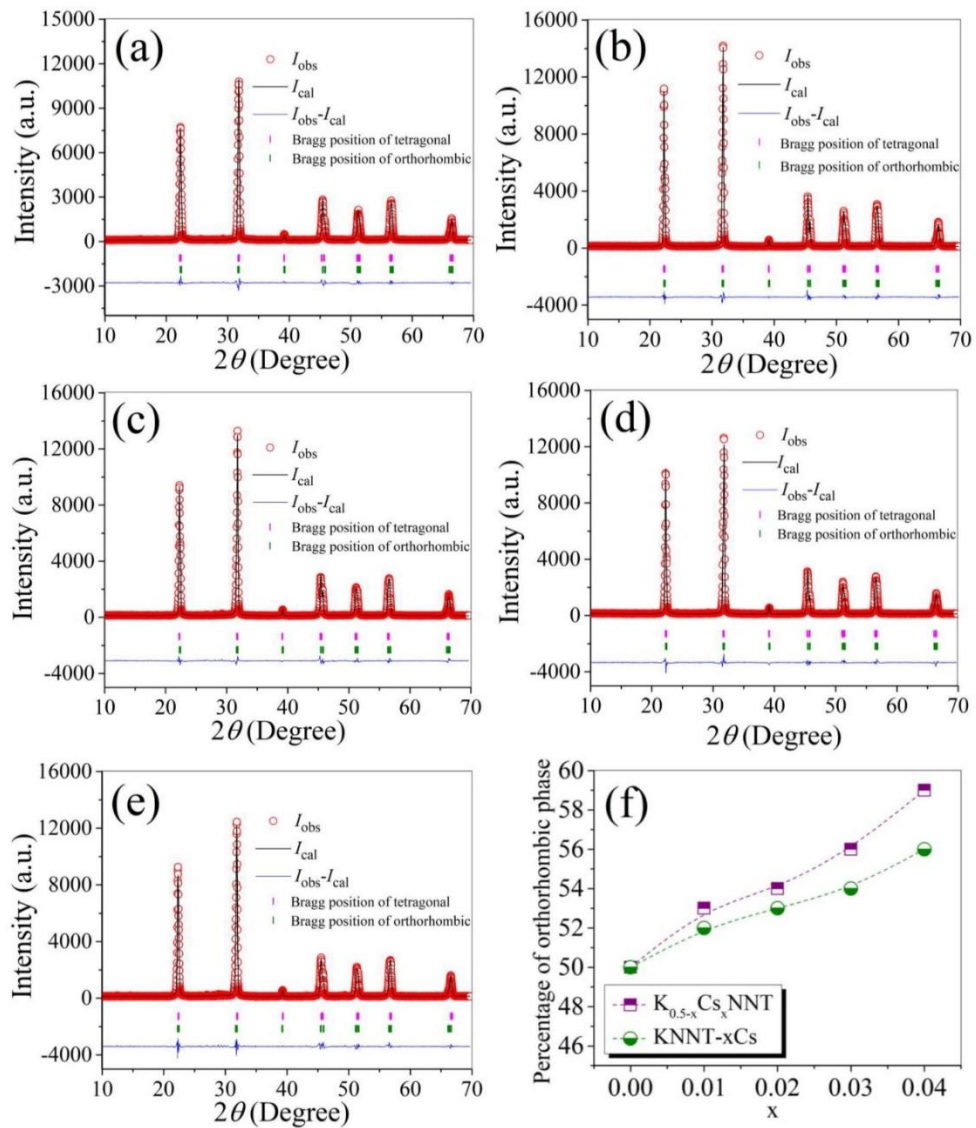


Figure 59 Rietveld refinement on XRD patterns of the KNNT (a), the $K_{0.5-x}Cs_xNNT$ with $x=0.01$ (b) and $x=0.03$ (c), and the $KNNT-xCs$ ceramics with $x=0.01$ (d) and $x=0.03$ (e); (f) the percentage of orthorhombic phase of the samples with different x .

Table 6 Goodness of fit, volume cell and phase percentage of the KNNT ceramics with different Cs⁺ substitutional and additional doping.

Sample	Refine parameters	Volume cell (Å ³)		Phase percentage (%)	
		<i>Amm2</i>	<i>P4mm</i>	<i>Amm2</i>	<i>P4mm</i>
KNNT	$\chi^2=2.49$, $R_p=11.0\%$ $R_{wp}=12.6\%$, $R_{exp}=7.98\%$	126.22	63.30	50	50
K _{0.49} Cs _{0.01} NNT	$\chi^2=1.85$, $R_p=9.62\%$ $R_{wp}=10.7\%$, $R_{exp}=7.83\%$	126.39	63.40	53	47
K _{0.48} Cs _{0.02} NNT	$\chi^2=1.91$, $R_p=9.26\%$ $R_{wp}=10.9\%$, $R_{exp}=7.86\%$	126.47	63.44	54	46
K _{0.47} Cs _{0.03} NNT	$\chi^2=2.23$, $R_p=10.2\%$ $R_{wp}=11.8\%$, $R_{exp}=7.89\%$	126.48	63.57	56	44
K _{0.46} Cs _{0.04} NNT	$\chi^2=1.72$, $R_p=9.31\%$ $R_{wp}=10.1\%$, $R_{exp}=7.71\%$	126.48	63.75	59	41
KNNT-0.01Cs	$\chi^2=2.32$, $R_p=11.4\%$ $R_{wp}=12.2\%$, $R_{exp}=7.99\%$	126.31	63.44	52	48
KNNT-0.02Cs	$\chi^2=2.54$, $R_p=11.1\%$ $R_{wp}=12.3\%$, $R_{exp}=7.73\%$	126.15	62.56	53	47
KNNT-0.03Cs	$\chi^2=2.72$, $R_p=12.1\%$ $R_{wp}=12.9\%$, $R_{exp}=7.81\%$	126.03	62.52	54	46
KNNT-0.04Cs	$\chi^2=2.19$, $R_p=9.91\%$ $R_{wp}=11.3\%$, $R_{exp}=7.64\%$	124.98	62.60	56	44

The SEM images of the K_{0.5-x}Cs_xNNT and KNNT-xCs ceramics with x=0-0.04 are shown in Figure 60 (a)-(i). The grains of all the ceramics exhibited a rather rectangular shape. As seen in Figure 60 (a), it was found that the undoped KNNT ceramic showed very dense, unclear grain boundaries and small pores. When doped with both substitutional and additional Cs⁺, the grain boundaries become clear and pores were observed. The porosity of both the K_{0.5-x}Cs_xNNT and KNNT-xCs ceramics increased as x increased. The average grain size of the KNNT ceramic was about 2.3±0.49 μm (Figure 60 (a)). For the K_{0.5-x}Cs_xNNT ceramics, the average grain size decreased to about 1.3±0.24 μm when x increased up to 0.04 (Figure 60 (b)-(e)). Similarly, the average grain size of the KNNT-xCs ceramics decreased to about 1.5±0.14 μm when x = 0.04 (Figure 60 (b)-(f-i)). Figure 61 shows the measured density of the K_{0.5-x}Cs_xNNT and KNNT-xCs ceramics as a function of x. The density value of both the K_{0.5-x}Cs_xNNT and KNNT-xCs ceramics decreased upon increasing

x. Comparing the results of Figure 61, it was observed that the KNNT-xCs ceramics had a higher density than that of $K_{0.5-x}Cs_x$ NNT ceramics. The reduction in the average grain size and the density can be explained by the increasing number of pores, which hinders mass transfer and densification during the sinter process (94, 105). In addition, it is well known that the alkaline elements (K and Na) in KNN-based ceramics are volatilized during the sintering process, due to their low boiling points, which results in deterioration of the sample density (104, 106). The energy dispersive X-ray spectrometer (EDS) technique was used to investigate the amount of each element for both the $K_{0.5-x}Cs_x$ NNT and KNNT-xCs ceramics with $x=0.01$ and 0.04 , as seen in Figure 62 (a)-(d). O, Na, Ta, Nb, K, Cs and Au elements were detected in all compositions. The Au spectrum is due to the sample coating process of the EDS. It was found that the quantity of Na and K in the $K_{0.5-x}Cs_x$ NNT ceramics with $x=0.01$ was about 4.57 and 7.80 wt.%, and at $x=0.04$, it was about 4.63 and 6.88 wt.% (Figure 62 (a)-(b)). In the case of KNNT-xCs ceramics with $x=0.01$, the amount of Na and K was about 5.25 and 7.72 wt.%, and at $x=0.04$ it was about 5.74 and 8.03 wt.% (Figure 62 (c)-(d)). Here it can be seen that K and Na elements in the ceramics with Cs^+ substitutional doping is less than for the additional doping samples, which might be the reason for the $K_{0.5-x}Cs_x$ NNT ceramics lower density, than of KNNT-xCs ceramics. To inspect the distribution of each element in the specimens, the surface element mapping of both the $K_{0.5-x}Cs_x$ NNT and KNNT-xCs ceramics with $x=0.04$ were carried out, as seen in Figure 63 (a)-(b). It was observed that K, Na, Nb, Ta, O and Cs elements of both substitutional and additional doping ceramics were uniformly distributed throughout the microstructure.

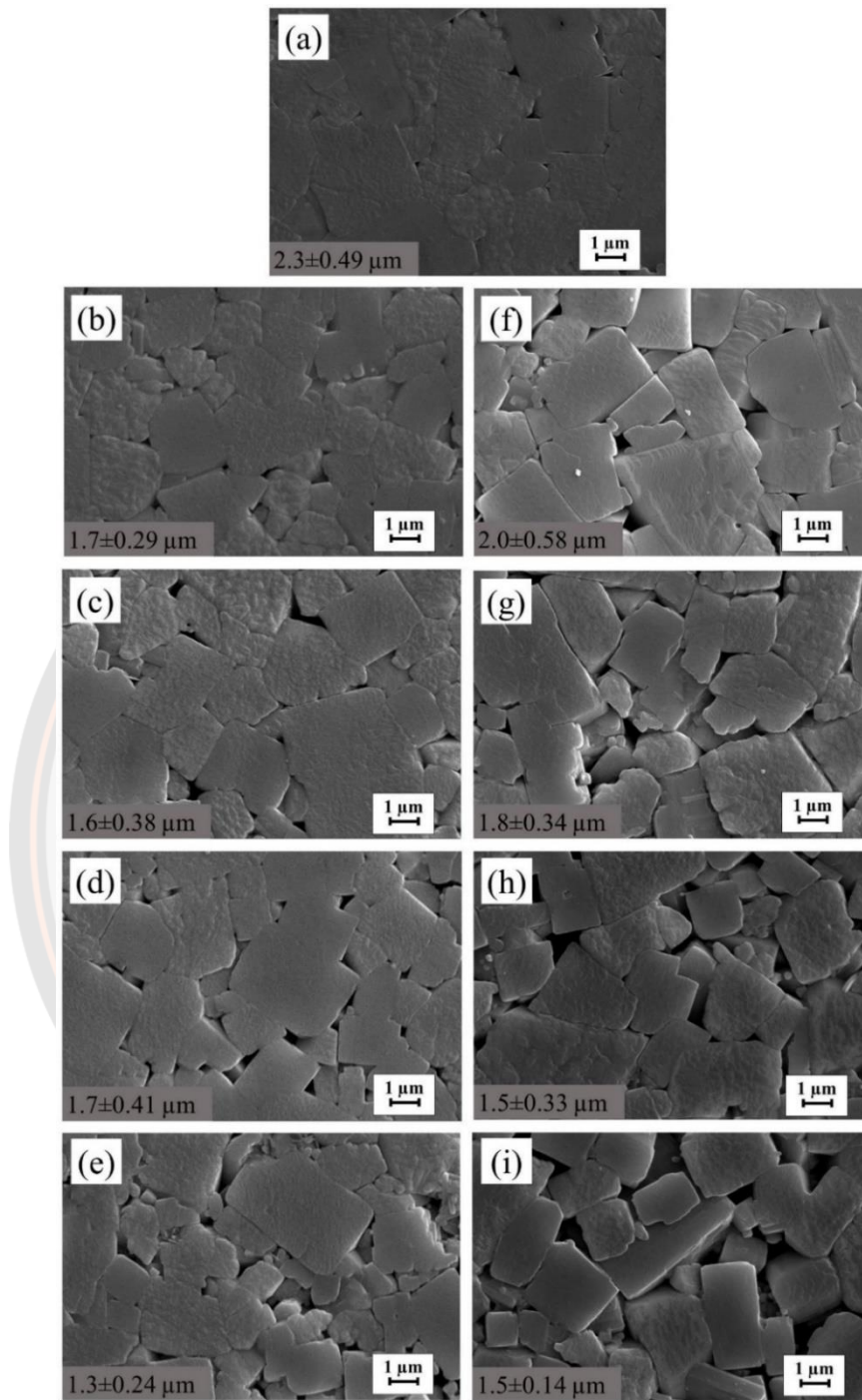


Figure 60 SEM images of the (a) KNNT ceramic, (b-e) K_{0.5-x}Cs_xNNT ceramics with x=0.01-0.04 and (f-i) KNNT-xCs ceramics with x=0.01-0.04.

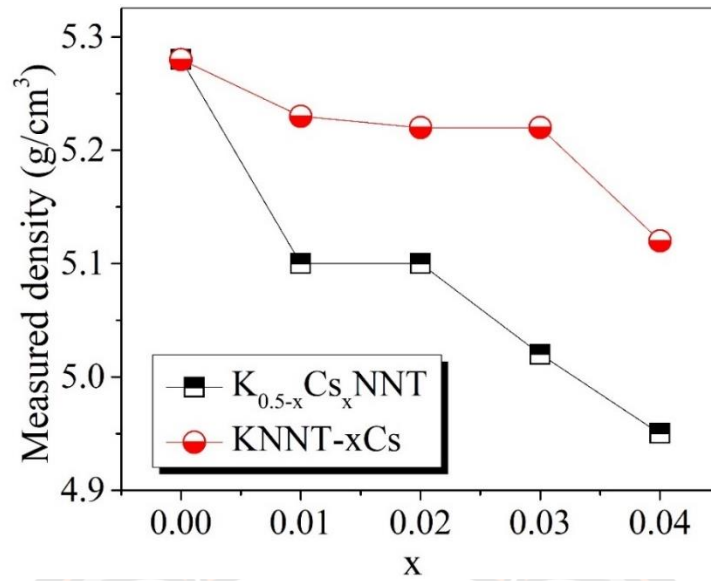


Figure 61 Measured density of the $K_{0.5-x}Cs_xNNT$ and $KNNT-xCs$ ceramics as a function of x .

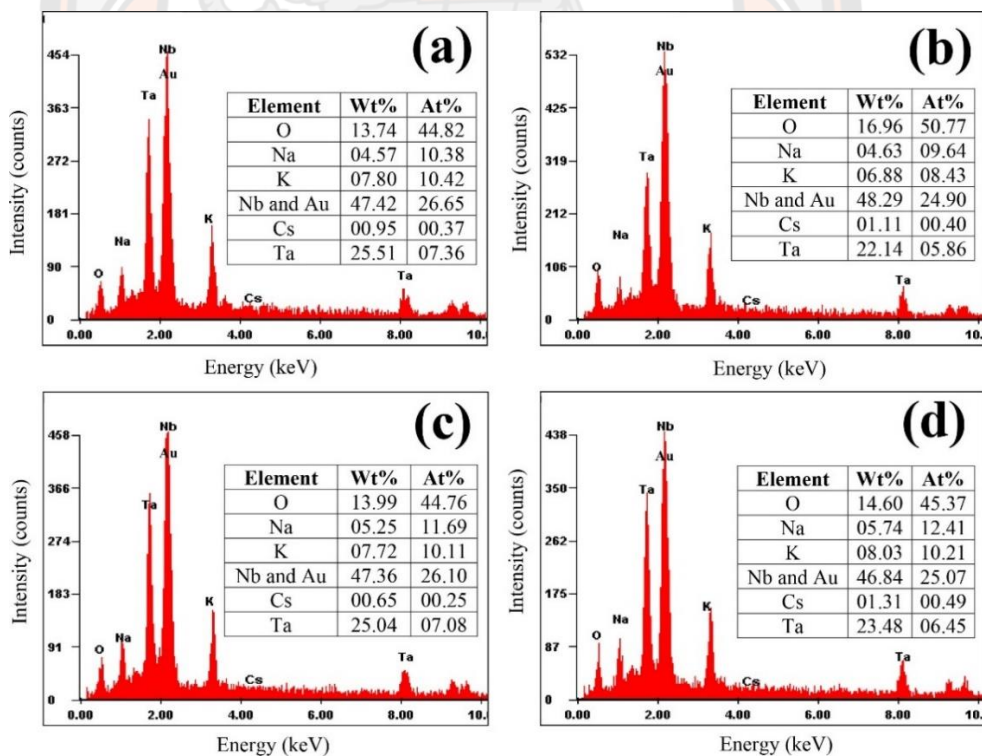


Figure 62 EDS spectra of the $K_{0.5-x}Cs_xNNT$ ceramics with (a) $x=0.01$, (b) $x=0.04$ and the $KNNT-xCs$ ceramics with (c) $x=0.01$ and (d) $x=0.04$.

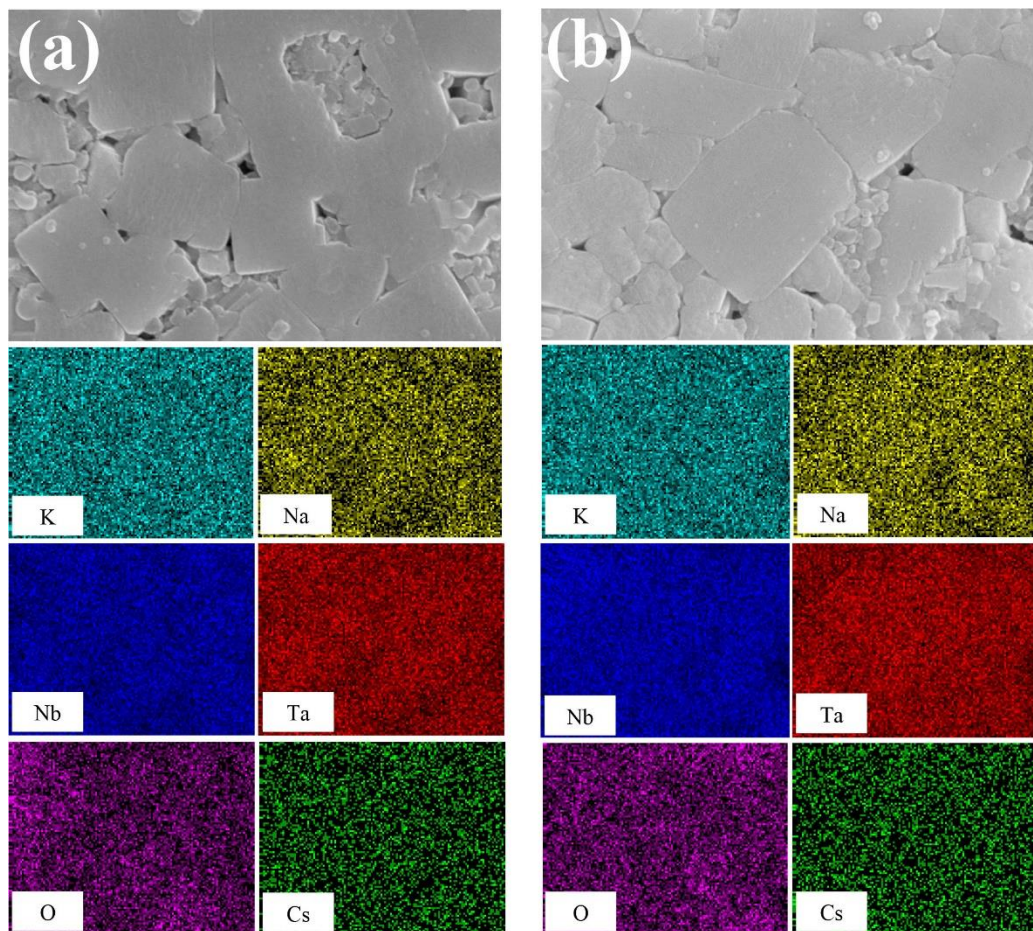


Figure 63 Elemental mapping of (a) the $K_{0.5-x}Cs_xNNT$ ceramic with $x=0.04$ and (b) the $KNNT-xCs$ ceramic with $x=0.04$.

The dielectric constant and dielectric loss of the $K_{0.5-x}Cs_xNNT$ and $KNNT-xCs$ ceramics with different x , measured at 1 kHz are displayed in Figure 64 (a)-(b). Two phase transitions were observed in all samples, which corresponded to the orthorhombic ferroelectric-tetragonal ferroelectric phase transition at $\sim 85^\circ\text{C}$ (T_{O-T}) and the tetragonal ferroelectric-cubic paraelectric phase transition at $\sim 220^\circ\text{C}$ (T_C). T_{O-T} and T_C were determined using the interception of the two tangents on both sides of the peak and the temperature at the maximum value of the dielectric constant, respectively. For, both the $K_{0.5-x}Cs_xNNT$ and $KNNT-xCs$ ceramics, T_{O-T} and T_C tended to decrease with increasing x , as seen in Table 7. Generally, changes in T_{O-T} and T_C can be explained by lattice distortions in the crystal structure, corresponding to previous reports (95, 107). The dielectric constant at room temperature (ϵ_R) and at the

Curie temperature (ε_C) of all compositions are listed in Table 7. The ε_R and ε_C of the undoped KNNT ceramic were around 1372 and 5115. Cs^+ doping, either substitutional and additional doping, strongly decreased the ε_R and ε_C . As shown in Figure 64 (a) and (b), higher x results in lower ε_R and ε_C . The highest of the ε_R and ε_C values in undoped KNNT ceramic can be explained by well-developed microstructure, high density, and the optimum proportion of $O:T$ phases (50:50) leading to enhanced the polarization within the material (108). While, the deterioration of the dielectric properties of the ceramics with Cs^+ was caused by the low density and porous structures forming at the grain boundaries, leading to a high electrical conductivity (109). For comparison in Table 7, one can see that ε_C values of the $\text{K}_{0.5-x}\text{Cs}_x\text{NNT}$ ceramics with $x=0.01-0.04$ were only about 4746-3423, but that of the KNNT-xCs ceramics with $x=0.01-0.04$ were about 4797-4118. Thus, KNNT-xCs ceramics had much higher dielectric constants than $\text{K}_{0.5-x}\text{Cs}_x\text{NNT}$ ceramics, which may be attributed to the higher density value of KNNT-xCs ceramics (Figure 61). The dielectric loss ($\tan \delta$) at T_R and T_C of the KNNT ceramics with Cs^+ substitutional and additional doping are shown in Table 7.

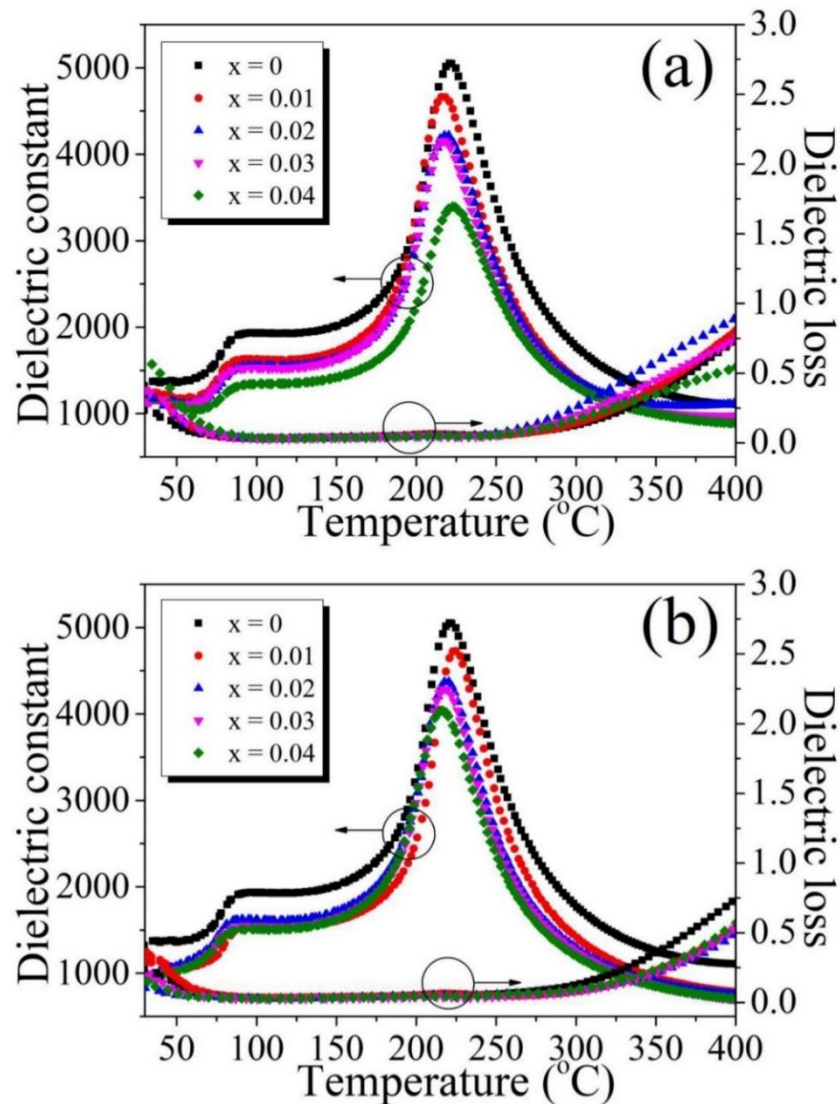


Figure 64 Temperature dependence of the dielectric constant and dielectric loss for the (a) $K_{0.5-x}Cs_xNNT$ and (b) $KNNT-xCs$ ceramics with different x .

Figure 65 (a-b) illustrates the polarization-electric field (P - E) hysteresis loops of the $K_{0.5-x}Cs_xNNT$ and $KNNT-xCs$ ceramics with different x , measured under an electrical field of 20 kV/cm and at a frequency of 1 Hz. The normal P - E hysteresis loop was found only in the undoped KNNT composition, while the rest were lossy loops. The undoped KNNT ceramic showed a well-saturated P - E hysteresis loop. When doped both substitutional and additional with Cs^+ , a leakage current was created. Both $K_{0.5-x}Cs_xNNT$ and $KNNT-xCs$ ceramics showed the leakage current that

increased as x increased from 0.01 to 0.03. The remnant polarization (P_r) and coercive field (E_c) of $K_{0.5-x}Cs_xNNT$ and $KNNT-xCs$ ceramics with different x are listed in Table 7. The P_r and E_c values of KNNT ceramics were $\sim 9.7 \mu C/cm^2$ and $\sim 7.6 kV/cm$. For the $K_{0.5-x}Cs_xNNT$ ceramics, the P_r and E_c increased to $40.3 \mu C/cm^2$ and $14.0 kV/cm$ when x increased up to 0.03. Likewise, the P_r and E_c of $KNNT-xCs$ ceramics tended to increase, up to $39.6 \mu C/cm^2$ and $13.7 kV/cm$ when x increased up to 0.03. Except for the undoped KNNT composition, all P_r and E_c values were incorporated with the results of leakage current, not only from their ferroelectric domain responses. However, both the $K_{0.5-x}Cs_xNNT$ and $KNNT-xCs$ ceramics at $x=0.04$ could not be measured. This was mainly due to the high leakage current caused from the porous microstructure and low density.

Table 7 Dielectric and ferroelectric properties of KNNT ceramics as a function of Cs^+ additional and substitutional doping.

samples	T_{O-T}	T_C	ϵ_R	tan δ at		tan δ at	P_r	E_c
	(°C)	(°C)		T_R	ϵ_C			
KNNT	90	221	1372	0.23	5115	0.06	9.7	7.6
$K_{0.49}Cs_{0.01}NNT$	83	217	1246	0.36	4746	0.07	23.7	10.4
$K_{0.48}Cs_{0.02}NNT$	85	216	1148	0.32	4284	0.04	33.5	14.0
$K_{0.47}Cs_{0.03}NNT$	83	216	1138	0.36	4242	0.05	40.3	14.0
$K_{0.46}Cs_{0.04}NNT$	84	220	1179	0.54	3423	0.05	-	-
KNNT-0.01Cs	89	224	1122	0.33	4797	0.06	32.6	12.5
KNNT-0.02Cs	83	218	988	0.10	4441	0.05	31.3	14.2
KNNT-0.03Cs	81	217	995	0.17	4374	0.05	39.6	13.7
KNNT-0.04Cs	80	215	946	0.13	4118	0.05	-	-

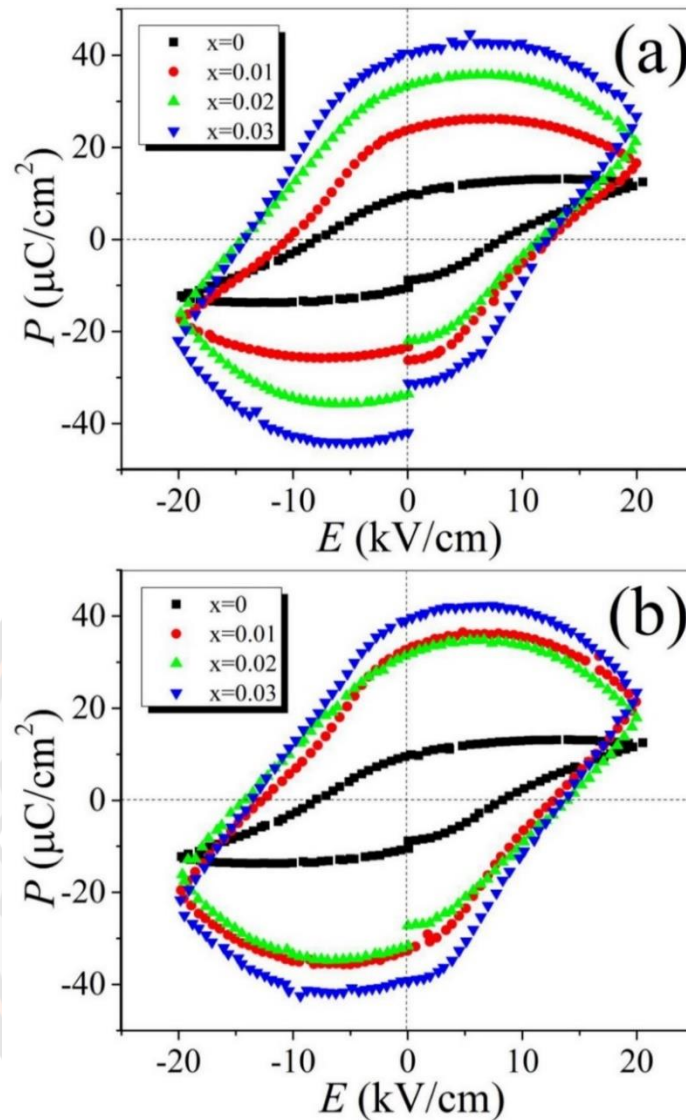


Figure 65 Ferroelectric hysteresis (P - E) loops at room temperature for the (a) $\text{K}_{0.5-x}\text{Cs}_x\text{NNT}$ and (b) KNNT-xCs ceramics with different x .

In summary, it is pointed out that the monitoring of phase evolution, density and electric behaviors for both $\text{K}_{0.5-x}\text{Cs}_x\text{NNT}$ and KNNT-xCs ceramics lead to the similar trend. The density and electrical properties of the KNNT-xCs samples were greater than the $\text{K}_{0.5-x}\text{Cs}_x\text{NNT}$ samples. Many studies have revealed that direct doping of element or compounds into KNN-based ceramics causes increment of liquid phase and oxygen vacancy, leading to enhance mass transport, resulting in improved density and electric behaviors of samples (84, 110).

3. The phase evolution, microstructure and electrical response of KNNT ceramics with Li⁺ substitution and doping

Figure. 66 depicts the XRD patterns of the surface region of the KN_{0.5-x}Li_xNT (Figure. 66 a(I-III)) and KNNT-xLi ceramics (Figure. 66 b(I-III)) with different x. All compositions exhibited a pure perovskite phase and no trace of any secondary phase was identified. This suggests that Li⁺ has fully diffused into the KNNT lattice, to form solid solution. Further scrutiny of the phase composition is seen in the enlarged XRD diagrams at 2θ around ~39° and ~45° in Figure. 66 a(II-III) - b(II-III). Ceramics with an orthorhombic (*O*) structure (JCPDS file no 01-071-0946) exhibits traits of dual (102)/(120)_{*O*} peaks around 39° and dual (022)/(200)_{*O*} peaks around 45°. In the event of a tetragonal (*T*) structure (JCPDS file no 01-071-0945), there is a single (111)_{*T*} peak around 39° and dual (002)/(200)_{*T*} peaks around 45°. In this experiment, the undoped KNNT ceramic with x=0 showed a diffraction peak with a broad and non-symmetry peak around 39° (Figure. 66 a(II) - b(II)) and dual peaks around 45° (Figure. 66 a(III) - b(III)). For the ceramics with Li⁺ doping (x=0.01-0.04), the peaks around 39° became sharper and non-symmetrical (Figure. 66 a(II) - b(II)) and three peaks appeared around 45° (Figure. 66 a(III)-b(III)). This indicated that the phase structure in all samples had coexisting *O* and *T* phases, a behavior similar to Li doped KNN ceramics [16]. Moreover, the diffraction peaks at ~39° and ~45° (Figure. 66 a(II-III)) of the KN_{0.5-x}Li_xNT ceramics moving slightly to higher 2θ angles as x increases from 0 to 0.02, indicating the contraction of the crystal lattice. This can be attributed to the small ionic radii of Li⁺ (1.15 Å) replacing larger Na⁺ (1.39 Å) in the ABO₃ structure. After that, the 2θ angles of the diffraction peaks shifted lower when the x increased up to 0.04 (Figure. 66 a(II-III)). The increasing of the unit cell volume can be caused by the Li⁺ ions partially entering the B-sites [Nb⁵⁺ (0.64 Å) or Ta⁵⁺ (0.64 Å)], this may be caused by the solubility limits of Li⁺ ions in A-sites (111). For the KNNT-xLi ceramics, the diffraction peaks at ~39° and ~45° (Figure. 66 b(II-III)) moving slightly to lower 2θ angles with rising x, indicating that the Li⁺ substituted into B-sites and the unit cell of the structure expands.

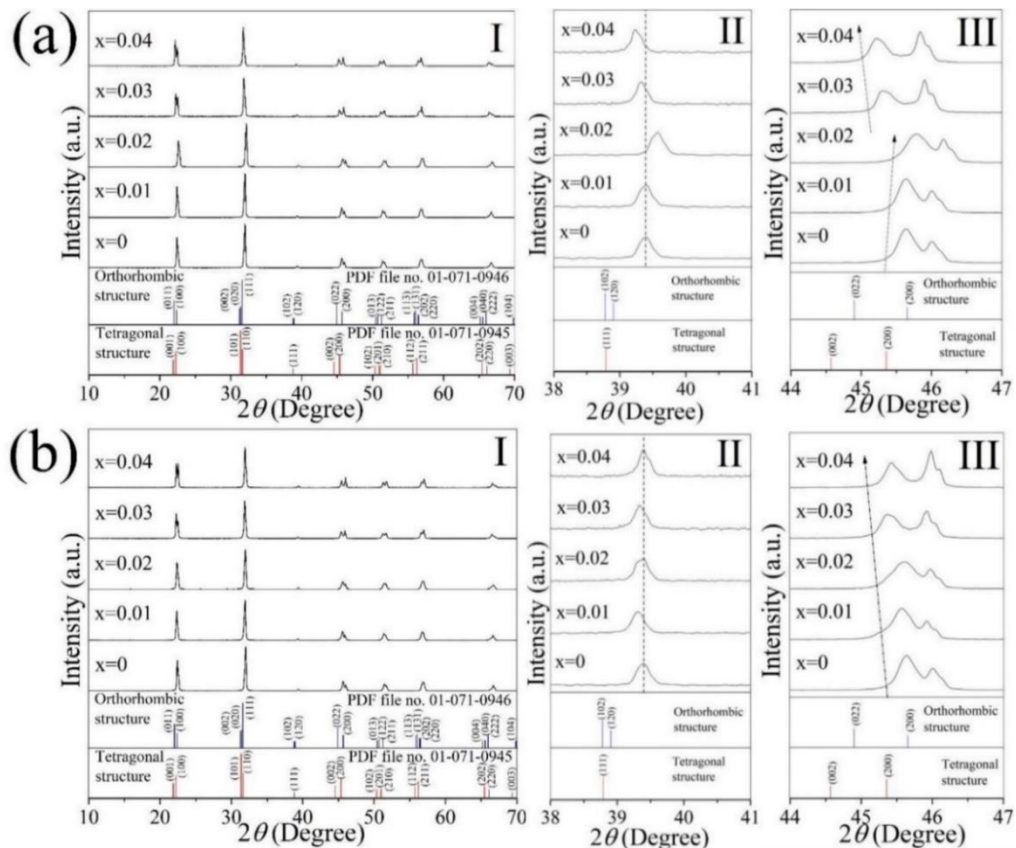


Figure 66 Room temperature XRD patterns of the (a) $\text{KN}_{0.5-x}\text{Li}_x\text{NT}$ and (b) KNNT-xLi ceramics with various x .

To further inspected the XRD analysis, Rietveld refinement was used on all the ceramics to fit the XRD data using the Fullprof software. The Crystallography Open Database (COD) is the standard information source for the initial values for space groups, lattice constants and atom functional positions. The XRD data of the $\text{KN}_{0.5-x}\text{Li}_x\text{NT}$ and KNNT-xLi ceramics were refined using a structural model based on KaNbO_3 with a tetragonal phase (T), with a $P4mm$ space group, and an orthorhombic phase (O), with an $Amm2$ space group. Figure. 67 (a)-(e) depicts the final output from the Rietveld refinement. As shown in Figure. 67 (a)-(e), observational data (I_{obs}), represented by the red hollow symbol, calculated patterns (I_{cal}) are represented by the black solid line and the different (I_{obs}) and (I_{cal}) is presented by the blue solid line. The quality values, lattice parameters, volume cell and phase percentage of all compositions are listed in Table 8. It was found that the

calculated quality of the fits were $R_p \leq 11.70\%$, $R_{wp} \leq 12.60\%$, $R_{exp} \leq 7.98\%$ and $\chi^2 \leq 2.62$ (Table 8), indicating fine agreement between the observed and calculated intensity profiles for all compositions. The fitting outcome showed that all ceramics had two phases in coexistence, the tetragonal and orthorhombic phases. For both the $\text{KN}_{0.5-x}\text{Li}_x\text{NT}$ and KNNT-xLi ceramics, the proportion of $T:O$ showed an increase of the T while the O declined with rising x (Table 8). Figure 67 (f) demonstrates the percentage of the tetragonal phase of the $\text{KN}_{0.5-x}\text{Li}_x\text{NT}$ and KNNT-xLi ceramics with various x .

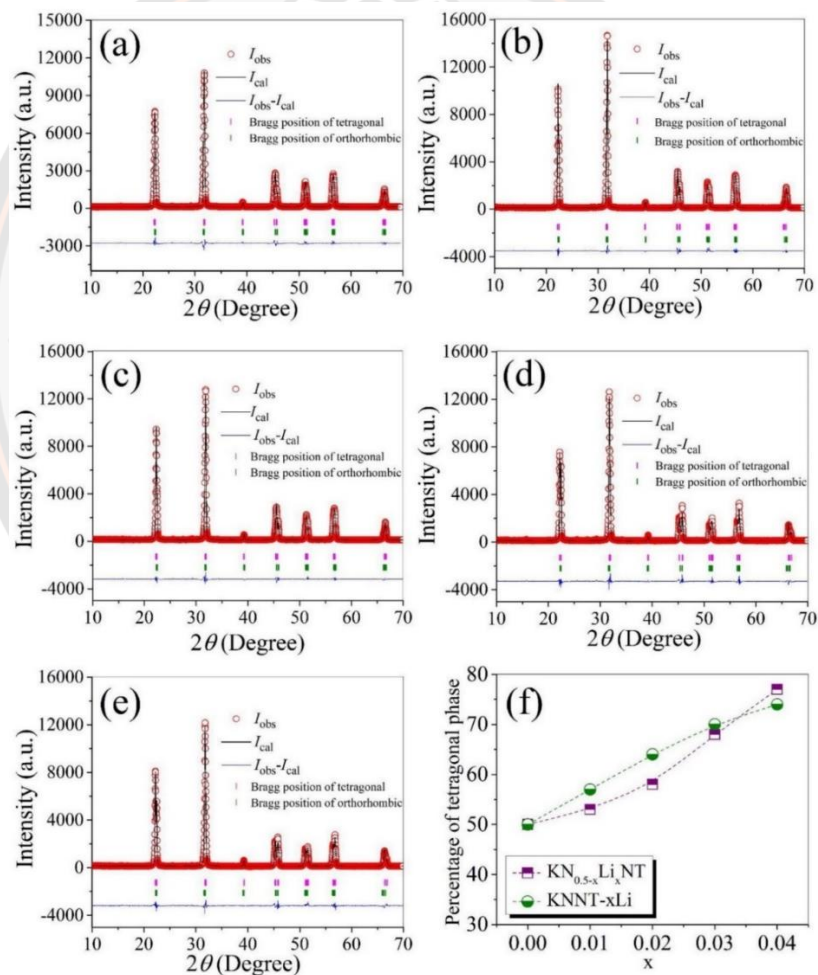


Figure 67 Rietveld refinement on XRD patterns of the KNNT (a), the $\text{KN}_{0.5-x}\text{Li}_x\text{NT}$ with $x=0.01$ (b) and $x=0.03$ (c), and the KNNT-xLi ceramics with $x=0.01$ (d) and $x=0.03$ (e); (f) the percentage of tetragonal phase of the samples with various x .

Table 8 The goodness of fit parameters, lattice parameters and the percentage of phases for the $\text{KN}_{0.5-x}\text{Li}_x\text{NT}$ and KNNT-xLi ceramics as a function of x .

Samples	Refine parameters	Lattice parameters		Phase percentage (%)	
		<i>P4mm</i>	<i>Amm2</i>	<i>P4mm</i>	<i>Amm2</i>
KNNT	$\chi^2=2.49$, $R_p=11.0\%$	$a=3.974 \text{ \AA}$,	$a=3.961 \text{ \AA}$,	50	50
	$R_{wp}=12.60\%$,	$c=4.008 \text{ \AA}$,	$b=5.656 \text{ \AA}$,		
	$R_{exp}=7.98\%$	$c/a=1.008$	$c=5.634 \text{ \AA}$		
$\text{KN}_{0.49}\text{Li}_{0.01}\text{NT}$	$\chi^2=1.88$, $R_p=9.70\%$	$a=3.999$,	$a=3.961 \text{ \AA}$,	53	47
	$R_{wp}=10.40\%$,	$c=3.957$,	$b=5.629 \text{ \AA}$,		
	$R_{exp}=7.56\%$	$c/a=0.989$	$c=5.646 \text{ \AA}$		
$\text{KN}_{0.48}\text{Li}_{0.02}\text{NT}$	$\chi^2=2.23$, $R_p=9.63\%$	$a=3.996 \text{ \AA}$,	$a=3.960 \text{ \AA}$,	58	42
	$R_{wp}=10.90\%$,	$c=3.953 \text{ \AA}$,	$b=5.642 \text{ \AA}$,		
	$R_{exp}=7.32\%$	$c/a=0.989$	$c=5.631 \text{ \AA}$		
$\text{KN}_{0.47}\text{Li}_{0.03}\text{NT}$	$\chi^2=2.13$, $R_p=10.50\%$	$a=3.965 \text{ \AA}$,	$a=3.967 \text{ \AA}$,	68	32
	$R_{wp}=11.30\%$,	$c=4.015 \text{ \AA}$,	$b=5.672 \text{ \AA}$,		
	$R_{exp}=7.78\%$	$c/a=1.012$	$c=5.637 \text{ \AA}$		
$\text{KN}_{0.46}\text{Li}_{0.04}\text{NT}$	$\chi^2=2.62$, $R_p=11.70\%$	$a=3.966 \text{ \AA}$,	$a=3.964 \text{ \AA}$,	77	23
	$R_{wp}=12.60\%$,	$c=4.018 \text{ \AA}$,	$b=5.683 \text{ \AA}$,		
	$R_{exp}=7.79\%$	$c/a=1.013$	$c=5.642 \text{ \AA}$		
KNNT-0.01Li	$\chi^2=1.63$, $R_p=8.91\%$	$a=3.969 \text{ \AA}$,	$a=3.957 \text{ \AA}$,	57	43
	$R_{wp}=9.98\%$, $R_{exp}=7.82\%$	$c=3.997 \text{ \AA}$,	$b=5.644 \text{ \AA}$,		
		$c/a=1.007$	$c=5.626 \text{ \AA}$		
KNNT-0.02Li	$\chi^2=2.04$, $R_p=9.71\%$	$a=3.963$,	$a=3.957 \text{ \AA}$,	64	36
	$R_{wp}=11.00\%$,	$c=4.000$,	$b=5.645 \text{ \AA}$,		
	$R_{exp}=7.67\%$	$c/a=1.009$	$c=5.625 \text{ \AA}$		
KNNT-0.03Li	$\chi^2=2.39$, $R_p=11.60\%$,	$a=3.951 \text{ \AA}$,	$a=3.950 \text{ \AA}$,	70	30
	$R_{wp}=12.10\%$,	$c=3.994 \text{ \AA}$,	$b=5.632 \text{ \AA}$,		
	$R_{exp}=7.81\%$	$c/a=1.010$	$c=5.650 \text{ \AA}$		
KNNT-0.04Li	$\chi^2=2.31$, $R_p=11.30\%$	$a=3.950 \text{ \AA}$,	$a=3.949 \text{ \AA}$,	74	26
	$R_{wp}=11.80\%$,	$c=3.995 \text{ \AA}$,	$b=5.637 \text{ \AA}$,		
	$R_{exp}=7.78\%$	$c/a=1.011$	$c=5.645 \text{ \AA}$		

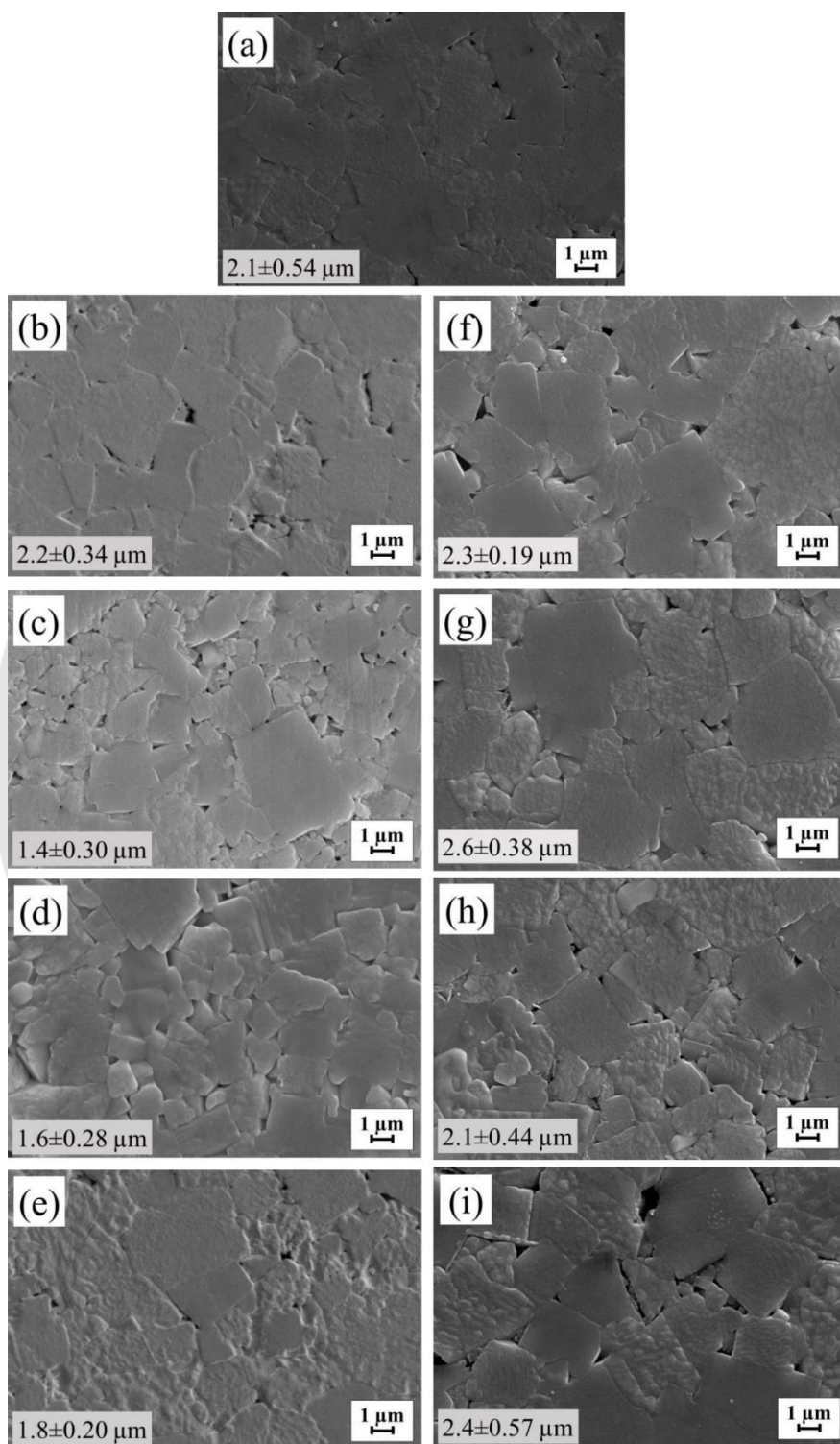


Figure 68 SEM micrographs of the (a) KNNT ceramics, (b-e) KN_{0.5-x}Li_xNT ceramics with $x=0.01-0.04$ and (f-i) KNNT-xLi ceramics with $x=0.01-0.04$.

The SEM images of the $\text{KN}_{0.5-x}\text{Li}_x\text{NT}$ and KNNT-xLi ceramics with $x=0-0.04$ are shown in Figure. 68 (a)-(i). The ceramic grains presented a rather rectangular shape, with a non-uniform grain size distribution as the growth of the grains was anisotropic for all compositions. As seen in Figure. 68 (a), it was found that the unmodified KNNT ceramic showed very dense, unclear grain boundaries and small pores. When doped with both substitutional and additional Li^+ , the grain boundaries become clear and pores were still observed. According to Zhen's study (84), the porous microstructure is primarily caused of the evaporation of the organic substances and alkali elements (K and Na). Chemical compositions of the $\text{KN}_{0.5-x}\text{Li}_x\text{NT}$ and KNNT-xLi ceramics ($x=0, 0.02$ and 0.04) were measured with an energy dispersive X-ray spectrometer (EDS) as summarized in Table 9. The elements of K, Na, Nb, Ta, O and Au were exposed. All specimens display a slight fluctuation in composition. The quantity of K and Na are very low as compared to the chemical formula, owing to their volatility. The average grain size of the unmodified KNNT ceramic was about $2.1\pm 0.54 \mu\text{m}$ (Figure. 68 (a)). For the $\text{KN}_{0.5-x}\text{Li}_x\text{NT}$ ceramics with $x=0.01-0.04$, the average grain sizes were in the range of 1.4 ± 0.30 to $2.2\pm 0.34 \mu\text{m}$ (Figure. 68 (b)-(e)). And the average grain size of the KNNT-xLi ceramics with $x=0.01-0.04$ was in the range of 2.1 ± 0.44 to $2.6\pm 0.38 \mu\text{m}$ (Figure. 68 (b)-(f-i)). The density value of both the $\text{KN}_{0.5-x}\text{Li}_x\text{NT}$ and KNNT-xLi ceramics decreased upon increasing x , as seen in Figure 69.

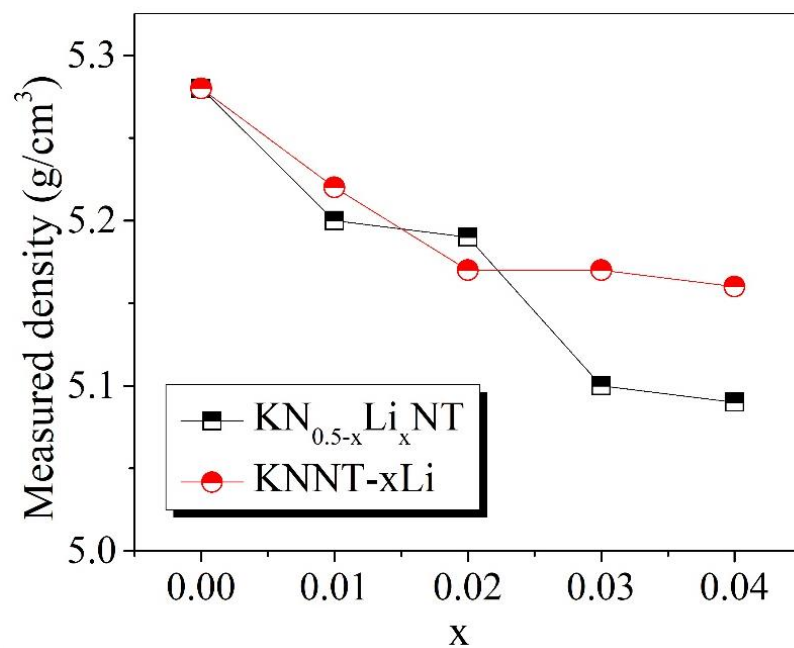


Figure 69 The measured density of the $\text{KN}_{0.5-x}\text{Li}_x\text{NT}$ and KNNT-xLi ceramics as a function of x .

Table 9 Chemical compositions of the $\text{KN}_{0.5-x}\text{Li}_x\text{NT}$ and KNNT-xLi ceramics as a function of x .

Samples	Elements (wt.%)				
	K	Na	Nb and Au	Ta	O
KNNT	8.10	5.92	44.41	25.04	16.53
$\text{KN}_{0.48}\text{Li}_{0.02}\text{NT}$	7.77	5.41	44.16	26.74	15.92
$\text{KN}_{0.46}\text{Li}_{0.04}\text{NT}$	7.48	5.05	42.96	31.75	12.77
KNNT-0.02Li	7.97	5.53	47.30	21.39	17.82
KNNT-0.04Li	7.82	3.19	50.01	24.23	17.74

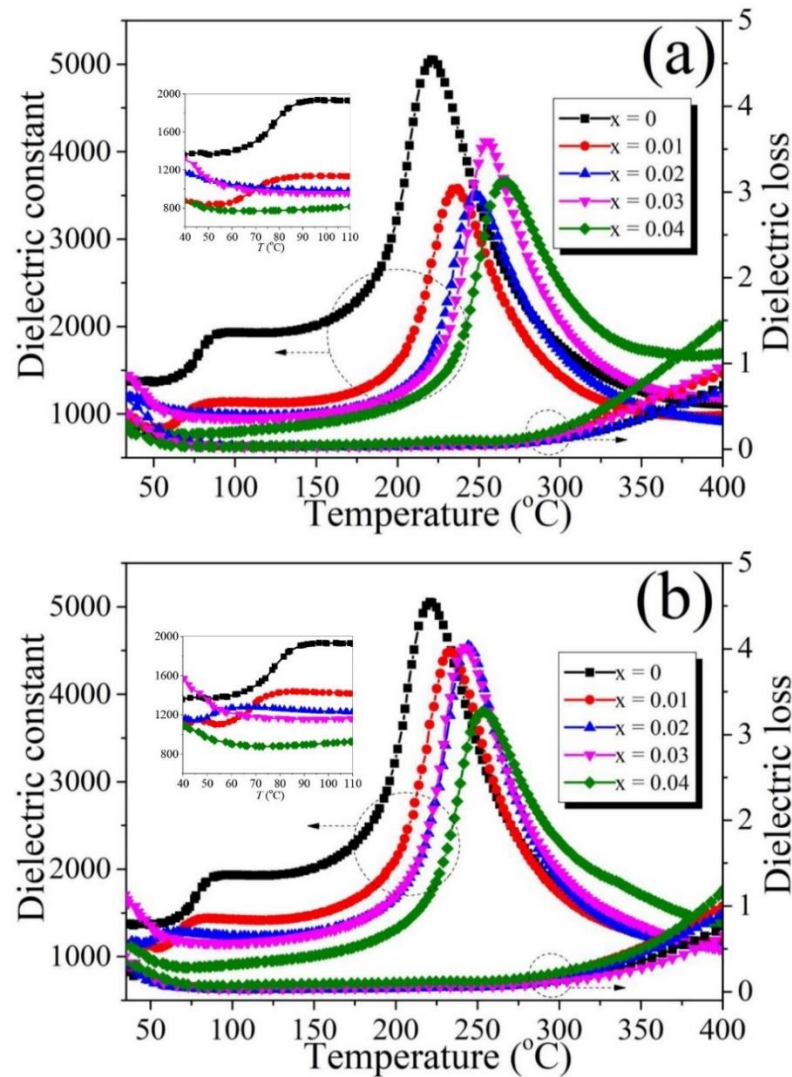


Figure 70 Temperature dependence of the dielectric constant and the loss tangent of the (a) $\text{KN}_{0.5-x}\text{Li}_x\text{NT}$ and (b) KNNT-xLi ceramics with various x , measured at 1 kHz.

The dielectric constant and dielectric loss of the $\text{KN}_{0.5-x}\text{Li}_x\text{NT}$ and KNNT-xLi ceramics with different x are displayed in Figure 70 (a)-(b). The unmodified KNNT ceramic had two-phase transition temperatures, associate with the ferroelectric orthorhombic-tetragonal phase transition at $\sim 90^\circ\text{C}$ ($T_{\text{O-T}}$) and ferroelectric tetragonal-paraelectric cubic phase transition at $\sim 221^\circ\text{C}$ (Curie temperature, T_{C}). When doped with substitutional Li^+ , $T_{\text{O-T}}$ of the $\text{KN}_{0.5-x}\text{Li}_x\text{NT}$ ceramic decreased to $\sim 77^\circ\text{C}$ when $x=0.01$. For the KNNT-xLi ceramics, $T_{\text{O-T}}$ decreased to $\sim 60^\circ\text{C}$ when $x=0.02$. While

the $\text{KN}_{0.5-x}\text{Li}_x\text{NT}$ ceramics at $x=0.02-0.04$ and KNNT-xLi ceramics at $x=0.03-0.04$, saw the T_{O-T} moved to temperatures too low to measure. On the other hand, the T_C of both $\text{KN}_{0.5-x}\text{Li}_x\text{NT}$ and KNNT-xLi ceramics shifted to higher temperatures ~ 266 and 253°C , respectively (Table 10), when x increased up to 0.04. The incremental increase of the T_C may be attributed to the increased tetragonal distortion, as seen by Long et al. (16). The dielectric constant at room temperature (ϵ_R) and the Curie temperature (ϵ_C) of all compositions are summarized in Table 10. The ϵ_C of the undoped KNNT ceramic was around 5115. With x increasing up to 0.02, the ϵ_C values of the $\text{KN}_{0.5-x}\text{Li}_x\text{NT}$ ceramics tended to decrease and then increased at $x=0.03$. When $x>0.03$, the ϵ_C value dropped again (Table 10). For the KNNT-xLi ceramics, the ϵ_C values declined with rising x , up to 0.01 and then increased at $x=0.02$. With $x>0.02$, the ϵ_C values dropped again. However, the in-depth explanation for the changing of the ϵ_C values could not be exactly determined. A possible explanation might be due to the complexity and fluctuation of the studied compositions (112, 113). For comparison in Table 10, one can see that ϵ_C values of the $\text{KN}_{0.5-x}\text{Li}_x\text{NT}$ ceramics with $x=0.01-0.04$ were only about 4141-3540, but that of the KNNT-xLi ceramics with $x=0.01-0.04$ were about 4595-3844. Thus, KNNT-xLi ceramics had much higher dielectric constants than $\text{KN}_{0.5-x}\text{Li}_x\text{NT}$ ceramics. The deterioration of the dielectric constants of the specimens with Li^+ was brought about by the low density and porous structures forming at the grain boundaries, leading to an elevated electrical conductivity. The dielectric loss ($\tan \delta$) at room temperature (T_R) and T_C of the KNNT ceramics with Li^+ substitutional and additional doping are shown in Table 10. The $\tan \delta$ at T_R of unmodified KNNT ceramics was about 0.23. The $\text{KN}_{0.5-x}\text{Li}_x\text{NT}$ and KNNT-xLi ceramics were found in the range of 0.21-0.59 and 0.23-0.43, respectively. The high $\tan \delta$ at T_R and at a temperature above T_C , which was related to high concentration flaws in the samples. The defect equations from the substitution of Li^+ in a KNNT lattice at A-sites (A_2O ; $\text{A}=\text{K}$ and Na) or B-sites (B_2O_5 ; $\text{B}=\text{Nb}$ and Ta) can be written as (23) and (24), respectively.



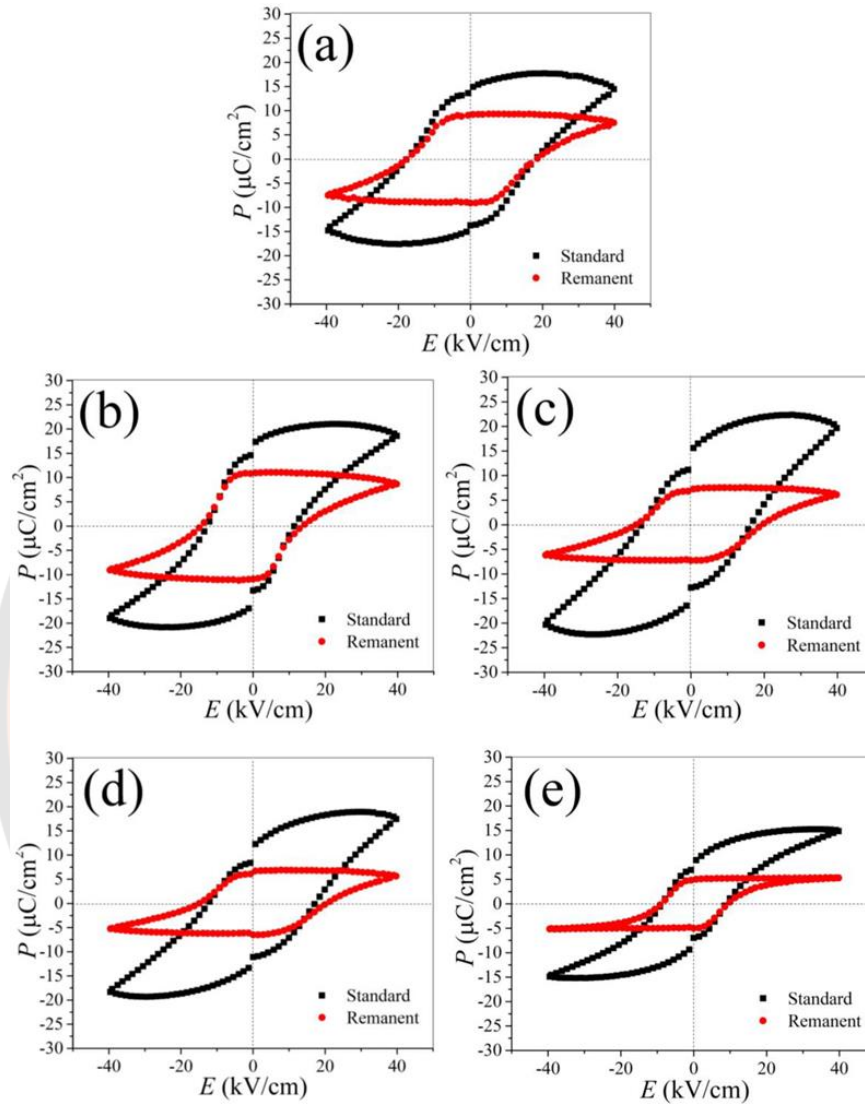
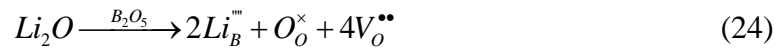


Figure 71 Room-temperature P - E hysteresis loops of the $KN_{0.5-x}Li_xNT$ ceramics with $x=0.01-0.04$.

The polarization-electric field (P - E) hysteresis loops with standard polarization hysteresis loops and remanent polarization hysteresis loops of the $KN_{0.5-x}Li_xNT$ samples with different x are plotted in Figure 71 (a)-(e). The standard polarization hysteresis loops display a typical P - E loop and leakage current for all compositions. The P - E loops were slimmer with rising x . The appearance of leakage

currents in the samples may be attributed to a high concentration of flaws and a low density, due to the volatility of the organic substances and alkali elements. It is well known that the standard polarization values obtained using the traditional hysteresis loops involves contributions from both the true-remanent (i.e., remanent polarization) and non-remanent (diode effects, leakage currents, etc.,) components (114, 115). To separate the non-remanent components and reveal the value of the remanent polarization (P_r), the samples polarization response was measured after two consecutive half-triangular waves of the same polarity (114, 115). For all samples, it can be observed that the remanent P - E hysteresis loops displays a reduction in P_r and becomes squarer compared with standard polarization hysteresis loops owing to the removal of the segment caused by conduction losses and other factors. The P - E hysteresis loops of the KNNT- x Li showed similar observations. The P_r and coercive electric field (E_C) of all compositions are listed in Table 10. The P_r value of the $\text{KN}_{0.5-x}\text{Li}_x\text{NT}$ ceramics increased from 9.20 to 10.89 $\mu\text{C}/\text{cm}^2$ when increasing x from 0 to 0.01 and then decreased (Table 10). The E_C value was found in the range of 9.19-20.14 kV/cm . For the KNNT- x Li ceramics, the P_r increased to $\sim 20.96 \mu\text{C}/\text{cm}^2$ when x went up to 0.04. The E_C of KNNT- x Li ceramics decreased from 17.78 to 10.70 kV/cm with x rising from 0 to 0.01, and then increased (Table 10). It can be observed that good remanent P - E hysteresis loops were found at $x=0.01$ for $\text{KN}_{0.5-x}\text{Li}_x\text{NT}$ ceramics ($P_r \sim 10.89 \mu\text{C}/\text{cm}^2$ and $E_C \sim 13.09 \text{kV}/\text{cm}$) and at $x=0.02$ for KNNT- x Li ceramics ($P_r \sim 15.65 \mu\text{C}/\text{cm}^2$ and $E_C \sim 11.46 \text{kV}/\text{cm}$). This result can be explained by large grain sizes (Figure 68), meaning that volume fraction of grain boundary and trapped space charge at the boundaries were reduces which makes ferroelectric domain reorientation easier and continuous (116), resulting in the improvement of the remanent P - E hysteresis loops of the samples.

Table 10 Dielectric and ferroelectric behaviors of KNNT ceramics as a function of Li⁺ additional and substitutional doping.

Samples	T_{O-T} (°C)	T_C (°C)	ϵ_R	$\tan \delta$ at T_R	ϵ_C	$\tan \delta$ at T_C	Remanent P - E hysteresis	
							P_r ($\mu\text{C}/\text{cm}^2$)	E_C (kV/cm)
KNNT	90	221	1372	0.23	5115	0.06	9.20	17.78
KN _{0.49} Li _{0.01} NT	77	234	877	0.42	3633	0.04	10.89	13.09
KN _{0.48} Li _{0.02} NT	-	247	1208	0.59	3540	0.05	7.03	18.89
KN _{0.47} Li _{0.03} NT	-	254	1441	0.41	4141	0.06	6.40	20.14
KN _{0.46} Li _{0.04} NT	-	266	903	0.21	3711	0.10	4.88	9.19
KNNT-0.01Li	75	233	1129	0.34	4541	0.06	13.02	10.70
KNNT-0.02Li	60	244	1155	0.32	4595	0.05	15.65	11.46
KNNT-0.03Li	-	243	1730	0.43	4588	0.06	20.36	19.01
KNNT-0.04Li	-	253	1153	0.37	3844	0.12	20.96	20.65

CHAPTER V

SUMMARY

First system, the effect of the firing conditions on the phase formation, microstructure, and electric properties of KNNT ceramics synthesized by the solid-state combustion method was studied. Pure KNNT powders were successfully formed after calcination at 600°C for 2 h. The average particle size increased when the calcination temperature was increased. The KNNT powder calcined at 600°C for 2 h showed rather square morphology and average particle size of ~160 nm, as verified by TEM. All the ceramics showed pure perovskite structure with coexisting *O* + *T* phases, as confirmed by XRD analysis. Rietveld refinement revealed that the tetragonality increased as the dwell time was increased from 2 to 4 h. The MPB region with a 50:50 ratio of *O*:*T* was obtained for the ceramic sintered at 1150°C for 4 h. The average grain size and density values increased as the dwell time was increased from 2 to 4 h but then degraded. KNNT ceramic with good crystalline morphology, the highest density ($\rho = 5.28 \text{ g/cm}^3$), the highest dielectric constant ($\epsilon_c = 5002$), and good ferroelectric behavior ($P_r = 18.50 \text{ } \mu\text{C/cm}^2$ and $E_c = 9.04 \text{ kV/cm}$) was obtained when using the firing condition of 1150°C for 4 h. The results of this work suggest that the firing conditions can play an important role in increasing and improving the densification, microstructure, and dielectric and ferroelectric properties of KNNT ceramics.

The KNNT ceramics with Cs⁺ substitutional ($\text{K}_{0.5-x}\text{Cs}_x\text{NNT}$) and additional (KNNT-*x*Cs) doping at *x*=0, 0.01, 0.02, 0.03 and 0.04 mol.% were synthesized by the solid-state combustion technique. The phase evolution, microstructure, dielectric and ferroelectric properties of the ceramics were investigated. All ceramics revealed a pure perovskite structure with coexisting *O*+*T* phases. Increasing both the amount of Cs⁺ substitutional and additional doping enhanced the content of orthorhombic phase, as verified by the Rietveld refinement technique. It has been demonstrated that Cs⁺ doping, either substitutional or additional, strongly decreased the density, dielectric and ferroelectric properties. The undoped KNNT ceramic showed a well-saturated *P*-

E hysteresis loop, while it became unsaturated and a leakage current was generated with Cs^+ doping. The KNNT- $x\text{Cs}$ ceramics demonstrated a higher density and dielectric properties than the $\text{K}_{0.5-x}\text{Cs}_x\text{NNT}$ ceramics. The deterioration in the dielectric and ferroelectric properties of the ceramics was mainly due to the inferior microstructure and low density induced by Cs^+ doping. The results of the phase evolution, microstructure, density, and electrical properties are all in agreement with each other.

For, a system of KNNT ceramics with Li^+ substitution ($\text{KN}_{0.5-x}\text{Li}_x\text{NT}$) and direct ($\text{KNNT-}x\text{Li}$) doping at $x=0, 0.01, 0.02, 0.03$ and 0.04 mol.% were fabricated via the solid-state combustion route. The phase structure, microstructure, dielectric, and ferroelectric properties of the specimens were inspected. The XRD results disclosed that all samples had coexisting orthorhombic and tetragonal phases. With increasing Li^+ doping, the content of the tetragonal phase of the ceramics was enhanced, as verified by the Rietveld refinement procedure. The density of both the $\text{KN}_{0.5-x}\text{Li}_x\text{NT}$ and $\text{KNNT-}x\text{Li}$ ceramics decreased with rising x . The Curie temperature (T_C) of both $\text{KN}_{0.5-x}\text{Li}_x\text{NT}$ and $\text{KNNT-}x\text{Li}$ ceramics shifted to higher temperatures with increasing x , due to increased tetragonal distortion, whereas the dielectric constant (ϵ_C) decreased. The worsening of the dielectric properties of the ceramics was affected by the increase of the defect concentration and low density, due to the volatilization of the alkali components. The $\text{KN}_{0.5-x}\text{Li}_x\text{NT}$ ceramics with $x=0.01$ showed good remanent P - E hysteresis loops ($P_r \sim 10.89 \mu\text{C}/\text{cm}^2$ and $E_C \sim 13.09 \text{ kV}/\text{cm}$), while for $\text{KNNT-}x\text{Li}$ ceramics, with the best results were with $x=0.02$ ($P_r \sim 15.65 \mu\text{C}/\text{cm}^2$ and $E_C \sim 11.46 \text{ kV}/\text{cm}$). All the results derived in this research are consistent with each other.

In summary, the deterioration in electrical properties of KNNT ceramics with Cs^+ and Li^+ substitution and direct doping can be attributed to the inappropriate $O:T$ phase ratio, low density and increase of the defect concentration in specimens.

We also studied the effect of ion radius on phase evolution, density and electric behaviors of KNNT ceramics. It can be concluded that the doping with Cs^+ at larger ion radius (1.88 \AA) into K^+ (1.64 \AA) and Na^+ (1.39 \AA) at A-site of KNNT ceramics increased the orthorhombic phase, whereas doping with Li^+ (1.15 \AA) at smaller ion radius into K^+ and Na^+ at A-site rise the tetragonal phase. However, the

results of density and electric behaviors for both Cs^+ and Li^+ doping into KNNT ceramics lead to the similar trend, i.e., declining.



REFERENCES

1. Qu J, Huang S, Xu Y, Jiao H, Xu D, Cheng X. Fabrication and properties of PZT piezoelectric ceramic tubes with large length–diameter ratio. *Ceramics International*. 2014;40(8, Part B):13019-24.
2. Lee T-G, Lee H-J, Kim D-H, Xu H, Park S-j, Park J-S, et al. Relation between structure and piezoelectric properties of $(1-x-y)\text{PbZrO}_{3-x}\text{PbTiO}_{3-y}\text{Pb}(\text{Ni}_{1/3}\text{Nb}_{2/3})\text{O}_3$ ceramics near triple point composition. *Journal of the European Ceramic Society*. 2016;36(16):4049-57.
3. Ledermann N, Muralt P, Baborowski J, Gentil S, Mukati K, Cantoni M, et al. $\{1\ 0\ 0\}$ -Textured, piezoelectric $\text{Pb}(\text{Zr}_x, \text{Ti}_{1-x})\text{O}_3$ thin films for MEMS: integration, deposition and properties. *Sensors and Actuators A: Physical*. 2003;105(2):162-70.
4. Chae M-S, Koh J-H. Piezoelectric behavior of $(1-x)(\text{PbMgNbO}_3\text{–PbZrTiO}_3)\text{–}x(\text{BaTiO}_3)$ ceramics for energy harvester applications. *Ceramics International*. 2014;40(1, Part B):2551-5.
5. Zhao C, Wu H, Li F, Cai Y, Zhang Y, Song D, et al. Practical High Piezoelectricity in Barium Titanate Ceramics Utilizing Multiphase Convergence with Broad Structural Flexibility. *J Am Chem Soc*. 2018;140(45):15252-60.
6. Zheng T, Wu J, Xiao D, Zhu J. Recent development in lead-free perovskite piezoelectric bulk materials. *Progress in Materials Science*. 2018;98:552-624.
7. Chen Z-h, Li Z-w, Qiu J-h, Zhao T-x, Ding J-n, Jia X-g, et al. Y_2O_3 doped $\text{Ba}_{0.9}\text{Ca}_{0.1}\text{Ti}_{0.9}\text{Sn}_{0.1}\text{O}_3$ ceramics with improved piezoelectric properties. *Journal of the European Ceramic Society*. 2018;38(4):1349-55.
8. Wu J, Xiao D, Zhu J. Potassium-sodium niobate lead-free piezoelectric materials: past, present, and future of phase boundaries. *Chem Rev*. 2015;115(7):2559-95.
9. Li L, Gong Y-Q, Gong L-J, Dong H, Yi X-F, Zheng X-J. Low-temperature hydro/solvothermal synthesis of Ta-modified $\text{K}_{0.5}\text{Na}_{0.5}\text{NbO}_3$ powders and piezoelectric properties of corresponding ceramics. *Materials & Design*. 2012;33:362-6.
10. Lv YG, Wang CL, Zhang JL, Wu L, Zhao ML, Xu JP. Tantalum influence on physical properties of $(\text{K}_{0.5}\text{Na}_{0.5})(\text{Nb}_{1-x}\text{Ta}_x)\text{O}_3$ ceramics. *Materials Research Bulletin*. 2009;44(2):284-7.

11. Zang G-Z, Yi X-J, Du J, Wang Y-F. Co₂O₃ doped (Na_{0.65}K_{0.35})NbO₃ piezoceramics. *Materials Letters*. 2010;64(12):1394-7.
12. Liu J, Zhu J, Li X, Wang M, Zhu X, Zhu J, et al. Effects of CuO doping on the electrical properties of 0.98K_{0.5}Na_{0.5}NbO₃-0.02BiScO₃ lead-free piezoelectric ceramics. *Materials Letters*. 2011;65(6):948-50.
13. Jaita P, Butnoi P, Sanjoom R, Random C, Yimmirun R, Rujijanagul G. Electric field-induced strain response of lead-free Fe₂O₃ nanoparticles-modified Bi_{0.5}(Na_{0.80}K_{0.20})_{0.5}TiO₃-0.03(Ba_{0.70}Sr_{0.03})TiO₃ piezoelectric ceramics. *Ceramics International*. 2017;43:S2-S9.
14. Bongkarn T, Chootin S, Pinitsoontorn S, Maensiri S. Excellent piezoelectric and ferroelectric properties of KNLNTS ceramics with Fe₂O₃ doping synthesized by the solid state combustion technique. *Journal of Alloys and Compounds*. 2016;682:14-21.
15. Zhao Y, Du J, Xu Z, Wei D, Fu Z, Wang Y. Domain evolution and corresponding piezoelectricity of lead-free In₂O₃-doped K_{0.5}Na_{0.5}NbO₃ ceramics together with improved fatigue resistance and temperature stability. *Materials Science and Engineering: B*. 2019;243:141-8.
16. Long C, Li T, Fan H, Wu Y, Zhou L, Li Y, et al. Li-substituted K_{0.5}Na_{0.5}NbO₃-based piezoelectric ceramics: Crystal structures and the effect of atmosphere on electrical properties. *Journal of Alloys and Compounds*. 2016;658:839-47.
17. Zhao R, Li Y, Zheng Z, Kang W. Phase structure regulation and enhanced piezoelectric properties of Li-doped KNN-based ceramics. *Materials Chemistry and Physics*. 2020;245:122806.
18. Lin D, Huang D, Zheng Q. Structure, dielectric and piezoelectric properties of K_{0.5}Na_{0.5}NbO₃-Bi_{0.5}(Na_{0.7}K_{0.2}Li_{0.1})_{0.5}TiO₃ ceramics. *Journal of Physics and Chemistry of Solids*. 2013;74(7):1021-5.
19. Shen Z-Y, Li Y-M, Luo W-Q, Wang Z-M. Enhancing piezoelectric properties by introducing Ni ion into B-site of Li/Sb-modified (K,Na)NbO₃ Pb-free piezoceramics. *Journal of the Ceramic Society of Japan*. 2012;120(1405):375-7.
20. Yan K, Wang F, Chen X, Wu D, Zhu K. Effects of A-site ionic size on the phase transition behavior of lead-free niobate ceramics. *Ceramics International*.

- 2019;45(16):20323-30.
21. Vendrell X, García JE, Bril X, Ochoa DA, Mestres L, Dezanneau G. Improving the functional properties of $(K_{0.5}Na_{0.5})NbO_3$ piezoceramics by acceptor doping. *Journal of the European Ceramic Society*. 2015;35(1):125-30.
 22. Wolfram T, Ellialtioglu S. *Electronic and Optical Properties of d-Band Perovskites*. Cambridge: Cambridge University Press; 2006.
 23. Galasso FS, editor *Structure, Properties and Preparation of Perovskite Type Compounds*1969.
 24. Johnsson M, Lemmens P. *Crystallography and Chemistry of Perovskites*. 2005;4.
 25. Peña MA, Fierro JLG. *Chemical Structures and Performance of Perovskite Oxides*. *Chemical Reviews*. 2001;101(7):1981-2018.
 26. Mickaël L. *Ferroelectrics - Material Aspects*2011. 532 p.
 27. Porta P, De Rossi S, Faticanti M, Minelli G, Pettiti I, Lisi L, et al. Perovskite-Type Oxides: I. Structural, Magnetic, and Morphological Properties of $LaMn_{1-x}Cu_xO_3$ and $LaCo_{1-x}Cu_xO_3$ Solid Solutions with Large Surface Area. *Journal of Solid State Chemistry*. 1999;146(2):291-304.
 28. Gazda M, Jasinski P, Kusz B, Bochentyn B, Gdula-Kasica K, Lendze T, et al. *Perovskites in Solid Oxide Fuel Cells. Diffusion and Defect Data-Solid State Data-Part B-Solid State Phenomena*. 2011;1567:65.
 29. Zaharii Z. *Polycrystalline Materials - Theoretical and Practical Aspects*2012. 178 p.
 30. Atta NF, Galal A, El-Ads EH, editors. *Perovskite Nanomaterials Synthesis, Characterization, and Applications*2016.
 31. Cady WG. *Piezoelectricity: An Introduction to the Theory and Applications of Electromechanical Phenomena in Crystals*: Dover Publications; 1964.
 32. Jaffe B, Roth RS, Marzullo S. *Piezoelectric Properties of Lead Zirconate-Lead Titanate Solid-Solution Ceramics*. *Journal of Applied Physics*. 1954;25(6):809-10.
 33. Smolensky GA, editor *New ferroelectrics of complex composition*. IV1961.
 34. Saito Y, Takao H, Tani T, Nonoyama T, Takatori K, Homma T, et al. Lead-free piezoceramics. *Nature*. 2004;432(7013):84-7.
 35. Barsoum M, Barsoum MW. *Fundamentals of Ceramics*: Taylor & Francis; 2002.
 36. Haertling GH. *Ferroelectric ceramics : History and technology*. *Journal of the*

- American Ceramic Society. 1999;82:797-818.
37. Zhang Y, Chen J, Dan H, Maraj M, Peng B, Sun W. Energy Storage and Electrocaloric Cooling Performance of Advanced Dielectrics. *Molecules*. 2021;26(2).
 38. Li F, Zhang S. Decoding the Fingerprint of Ferroelectric Loops: Comprehension of the Material Properties and Structures. *Journal of the American Ceramic Society*. 2014;97:1-27.
 39. Herring C. Effect of Change of Scale on Sintering Phenomena. *Journal of Applied Physics*. 1950;21(4):301-3.
 40. Handwerker C, Dynys J, Cannon R, Coble R. Metal Reference Line Technique for Obtaining Dihedral Angles from Surface Thermal Grooves. *Journal of the American Ceramic Society*. 2005;73:1365-70.
 41. Coble RL. Sintering Crystalline Solids. I. Intermediate and Final State Diffusion Models. In: Sōmiya S, Moriyoshi Y, editors. *Sintering Key Papers*. Dordrecht: Springer Netherlands; 1990. p. 55-67.
 42. Panda PK. Review: environmental friendly lead-free piezoelectric materials. *Journal of Materials Science*. 2009;44(19):5049-62.
 43. Jeong CK, Han JH, Palneedi H, Park H, Hwang G-T, Joung B, et al. Comprehensive biocompatibility of nontoxic and high-output flexible energy harvester using lead-free piezoceramic thin film. *APL Materials*. 2017;5(7):074102.
 44. Maeder MD, Damjanovic D, Setter N. Lead Free Piezoelectric Materials. *Journal of Electroceramics*. 2004;13(1):385-92.
 45. Bellaiche L, Garcia A, Vanderbilt D. Finite-temperature properties of $\text{Pb}(\text{Zr}_{1-x}\text{Ti}_x)\text{O}_3$ alloys from first principles. *Phys Rev Lett*. 2000;84(23):5427-30.
 46. Chen L, Qiu G, Peng B, Guo M, Zhang M. $(\text{K}_{0.5}\text{Na}_{0.5})(\text{Nb}_{1-x}\text{Ta}_x)\text{O}_3$ ceramics with a higher d_{33} : Preparation from a two-stage microwave hydrothermal process. *Ceramics International*. 2015;41(10, Part A):13331-40.
 47. Jaffe B, Cook WR, Jaffe H. CHAPTER 2 - THE PIEZOELECTRIC EFFECT IN CERAMICS. In: Jaffe B, Cook WR, Jaffe H, editors. *Piezoelectric Ceramics*: Academic Press; 1971. p. 7-21.
 48. Wang K, Li J-F. Analysis of crystallographic evolution in $(\text{Na,K})\text{NbO}_3$ -based lead-free piezoceramics by x-ray diffraction. *Applied Physics Letters*.

- 2007;91(26):262902.
49. Kosec M, Malič B, Benčan A, Rojac T. KNN-Based Piezoelectric Ceramics. In: Safari A, Akdoğan EK, editors. *Piezoelectric and Acoustic Materials for Transducer Applications*. Boston, MA: Springer US; 2008. p. 81-102.
 50. Zhou Y, Guo M, Zhang C, Zhang M. Hydrothermal synthesis and piezoelectric property of Ta-doping $K_{0.5}Na_{0.5}NbO_3$ lead-free piezoelectric ceramic. *Ceramics International*. 2009;35(8):3253-8.
 51. Malic B, Bernard J, Bencan A, Kosec M. Influence of zirconia addition on the microstructure of $K_{0.5}Na_{0.5}NbO_3$ ceramics. *Journal of the European Ceramic Society*. 2008;28(6):1191-6.
 52. Szymczak L, Ujma Z, Hańderek J, Kapusta J. Sintering effects on dielectric properties of $(Ba,Sr)TiO_3$ ceramics. *Ceramics International*. 2004;30(6):1003-8.
 53. JAEGER RE, EGERTON L. Hot Pressing of Potassium-Sodium Niobates. *Journal of the American Ceramic Society*. 1962;45(5):209-13.
 54. Jean F, Schoenstein F, Zaghrioui M, Bah M, Marchet P, Bustillo J, et al. Composite microstructures and piezoelectric properties in tantalum substituted lead-free $K_{0.5}Na_{0.5}Nb_{1-x}Ta_xO_3$ ceramics. *Ceramics International*. 2018;44(8):9463-71.
 55. Gu H, Zhu K, Pang X, Shao B, Qiu J, Ji H. Synthesis of $(K, Na)(Nb, Ta)O_3$ lead-free piezoelectric ceramic powders by high temperature mixing method under hydrothermal conditions. *Ceramics International*. 2012;38(3):1807-13.
 56. Yan H, Zhang Z, Zhu W, He L, Yu Y, Li C, et al. The effect of (Li,Ce) and (K,Ce) doping in Aurivillius phase material $CaBi_4Ti_4O_{15}$. *Materials Research Bulletin*. 2004;39(9):1237-46.
 57. Shannon RD. Revised effective ionic radii and systematic studies of interatomic distances in halides and chalcogenides. *Acta Crystallographica Section A*. 1976;32(5):751-67.
 58. Shirane G, Newnham R, Pepinsky R. Dielectric Properties and Phase Transitions of $NaNbO_3$ and $(Na,K)NbO_3$. *Physical Review*. 1954;96(3):581-8.
 59. Toby BH. EXPGUI, a graphical user interface for GSAS. *Journal of Applied Crystallography*. 2001;34:210-3.
 60. Larson AC, Dreele RB, Toby B. General structure analysis system -

- GSAS/EXPGUI. 1994;748.
61. Hewat AW. Cubic-tetragonal-orthorhombic-rhombohedral ferroelectric transitions in perovskite potassium niobate: neutron powder profile refinement of the structures. *Journal of Physics C: Solid State Physics*. 1973;6(16):2559-72.
 62. Lohkämper R, Neumann H, Arlt G. Internal bias in acceptor-doped BaTiO₃ ceramics: Numerical evaluation of increase and decrease. *Journal of Applied Physics*. 1990;68(8):4220-4.
 63. Wu J, Xiao D, Wang Y, Zhu J, Yu P, Jiang Y. Compositional dependence of phase structure and electrical properties in (K_{0.42}Na_{0.58})NbO₃-LiSbO₃ lead-free ceramics. *Journal of Applied Physics*. 2007;102(11):114113.
 64. Ren X, Peng Z, Chen B, Shi Q, Qiao X, Wu D, et al. A compromise between piezoelectricity and transparency in KNN-based ceramics: The dual functions of Li₂O addition. *Journal of the European Ceramic Society*. 2020;40(6):2331-7.
 65. Bunaciu AA, Udriștioiu EG, Aboul-Enein HY. X-ray diffraction: instrumentation and applications. *Crit Rev Anal Chem*. 2015;45(4):289-99.
 66. Sindhu M, Ahlawat N, Sanghi S, Agarwal A, Dahiya R, Ahlawat N. Rietveld refinement and impedance spectroscopy of calcium titanate. *Current Applied Physics*. 2012;12(6):1429-35.
 67. Panigrahi MR, Panigrahi S. Rietveld analysis of single phase Ba_{0.99}Dy_{0.01}TiO₃ ceramic. *Physica B: Condensed Matter*. 2010;405(18):3986-90.
 68. Yotthuan S, Charoonsuk T, Vittayakorn N, Thountom S, Suriwong T, Udeye T, et al. Effect of Firing Conditions on Phase Formation, Microstructure, and Electrical Properties of (K_{0.5}Na_{0.5})(Nb_{0.7}Ta_{0.3})O₃ Ceramics Synthesized by Solid-State Combustion Method. *Journal of Electronic Materials*. 2020;49(10):6143-55.
 69. Wikipedia. X-ray photoelectron spectroscopy 2021 [Available from: https://en.wikipedia.org/wiki/X-ray_photoelectron_spectroscopy].
 70. Nottingham Uo. X-ray Photoelectron Spectroscopy 2021 [Available from: <https://www.nottingham.ac.uk/nmrc/facilities/xps/x-ray-photoelectron-spectroscopy-xps.aspx>].
 71. Andres K. *An Introduction to Electron Microscopy Instrumentation, Imaging and Preparation*: Zurich; 2013.

72. Abd Mutalib M, Rahman M, Othman MH, Ismail A, Jaafar J. Scanning Electron Microscopy (SEM) and Energy-Dispersive X-Ray (EDX) Spectroscopy. 2017. p. 161-79.
73. Sinha A, Ischia G, Straffelini G, Gialanella S. A new sample preparation protocol for SEM and TEM particulate matter analysis. *Ultramicroscopy*. 2021;230:113365.
74. Wikipedia. Archimedes' principle [Available from: https://en.wikipedia.org/wiki/Archimedes%27_principle].
75. Wikipedia. Dielectric [Available from: <https://en.wikipedia.org/wiki/Dielectric>].
76. Wikipedia. Permittivity [Available from: <https://en.wikipedia.org/wiki/Permittivity>].
77. Stewart M, Cain M, Hall D. Ferroelectric hysteresis measurement and analysis. United Kingdom; 1999. Report No.: 1368-6550 Contract No.: NPL-R-CMMT/A--152.
78. Wang L, Wang X, Shi J. Measurement and Estimation of Ferroelectric Hysteresis Loops. *Ferroelectrics*. 2010;411(1):86-92.
79. Diamant H, Drenck K, Pepinsky R. Bridge for Accurate Measurement of Ferroelectric Hysteresis. *Review of Scientific Instruments*. 1957;28(1):30-3.
80. Lenka R, Mahata T, Sinha P, Tyagi A. Combustion synthesis of gadolinia-doped using glycine and urea fuels. *Journal of Alloys and Compounds - J ALLOYS COMPOUNDS*. 2008;466:326-9.
81. Pattipaka S, James AR, Pamu D. Enhanced dielectric and piezoelectric properties of BNT-KNNG piezoelectric ceramics. *Journal of Alloys and Compounds*. 2018;765:1195-208.
82. Kornphom C, Yotthuan S, Chootin S, Bongkarn T. The Influence of the Firing Temperatures on the Phase Evolution, Microstructure, Dielectric and Strain Responses of BCTS Ceramics Prepared by the Solid State Combustion Technique. *physica status solidi (a)*. 2018;215.
83. Kornphom C, Rittisak J, Laowanidwatana A, Bongkarn T. Enhanced dielectric and ferroelectric behavior in 0.94BNT-0.06BCTS lead free piezoelectric ceramics synthesized by the solid state combustion technique. *Integrated Ferroelectrics*. 2018;187(1):20-32.
84. Fu F, Shen B, Zhai J, Xu Z, Yao X. Electrical properties of Li doped sodium

- potassium niobate thick films prepared by a tape casting process. *Journal of Alloys and Compounds*. 2011;509(25):7130-3.
85. Sumang R, Wicheanrat C, Bongkarn T, Maensiri S. High densification and dielectric properties of lead-free $(K_{0.5}Na_{0.5})NbO_3$ piezoelectric ceramics with optimum excess Na_2O and K_2O contents. *Ceramics International*. 2015;41.
86. Wu J, Xiao D, Wu W, Zhu J, Wang J. Effect of dwell time during sintering on piezoelectric properties of $(Ba_{0.85}Ca_{0.15})(Ti_{0.90}Zr_{0.10})O_3$ lead-free ceramics. *Journal of Alloys and Compounds*. 2011;509.
87. Cheng H-l, Zhou W-c, Du H-l, Luo F, Zhu D-m. Effects of dwell time during sintering on electrical properties of $0.98(K_{0.5}Na_{0.5})NbO_3-0.02LaFeO_3$ ceramics. *Transactions of Nonferrous Metals Society of China*. 2013;23(10):2984-8.
88. Gu Q, Sun Q, Zhu K, Liu J, Qiu J. Low-temperature sintering and enhanced dielectric properties of alkali niobate ceramics prepared from solvothermally synthesized nanopowders. *Ceramics International*. 2017;43(1, Part B):1135-44.
89. Cong R, Qiu G, Yue C, Guo M, Cheng F, Zhang M. Oxygen-enriched sintering for improved piezoelectric performance of $(K_{0.5}Na_{0.5})(Ta_{0.3}Nb_{0.7})O_3$ lead-free ceramics: The impact of defects. *Ceramics International*. 2018;44(16):19764-70.
90. Sponchia G, Moshtaghoun BM, Benedetti A, Riello P, Gómez-García D, Domínguez-Rodríguez A, et al. Ceramics of Ta-doping stabilized orthorhombic ZrO_2 densified by spark plasma sintering and the effect of post-annealing in air. *Scripta Materialia*. 2017;130:128-32.
91. Zhong M, Li J, Shao J, Cao Y, Li K, Zhao W. An investigation into the enhanced permittivity properties of Zr co-doped $(Ga_{0.5}Nb_{0.5})_{0.03}Ti_{0.97}O_2$ ceramics. *Ceramics International*. 2019;45.
92. Guo D, Qin X, Lv M, Shi H, Su Y, Yao G, et al. Decrease of oxygen vacancy by Zn-doped for improving solar-blind photoelectric performance in $\beta-Ga_2O_3$ thin films. *Electronic Materials Letters*. 2017;13:1-6.
93. Cen Z, Zhen Y, Feng W, Zhao P, Chen L, Wang X, et al. Sintering temperature effect on microstructure, electrical properties and temperature stability of MnO-modified KNN-based ceramics. *Journal of the European Ceramic Society*. 2018;38.
94. Bueno P, Leite E, Bulhoes L, Longo E, Paiva-Santos C. Sintering and Mass

- Transport Features of (Sn,Ti)O₂ Polycrystalline Ceramics. *Journal of the European Ceramic Society*. 2003;23:887-96.
95. Zhen Y, Li J. Normal Sintering of (K,Na)NbO₃-Based Ceramics: Influence of Sintering Temperature on Densification, Microstructure, and Electrical Properties. *Journal of the American Ceramic Society*. 2006;89:3669-75.
96. Fang C, Liangyan C, Zhou D. Influence of domain on grain size effects of the dielectric properties of BaTiO₃ nanoceramics and nanoparticles. *Physica B: Condensed Matter*. 2013;409:83–6.
97. Trukhanov S, Trukhanov A, Szymczak H, Szymczak R, Baran M. Thermal stability of A-site ordered PrBaMn₂O₆ manganites. *Journal of Physics and Chemistry of Solids*. 2006;67:675-81.
98. Tang XG, Chew KH, Chan HLW. Diffuse phase transition and dielectric tunability of Ba(Zr_yTi_{1-y})O₃ relaxor ferroelectric ceramics. *Acta Materialia*. 2004;52(17):5177-83.
99. Trukhanov S, Lobanovsky L, Bushinsky M, Khomchenko V, Pushkarev N, Troyanchuk I, et al. Influence of oxygen vacancies on the magnetic and electrical properties of LaSrMnO manganites. *European Physical Journal B - EUR PHYS J B*. 2004;42:51-61.
100. Trukhanov S, Troyanchuk I, Trukhanov A, Fita I, Vasil'ev A, Maignan A, et al. Magnetic properties of La_{0.70}Sr_{0.30}MnO_{2.85} anion-deficient manganite under hydrostatic pressure. *Jetp Letters - JETP LETT-ENGL TR*. 2006;83:33-6.
101. Bhupajit P, Kornphom C, Vittayakorn N, Bongkarn T. Structural, microstructure and electrical properties of La₂O₃-doped Bi_{0.5}(Na_{0.68}K_{0.22}Li_{0.1})_{0.5}TiO₃ lead-free piezoelectric ceramics synthesized by the combustion technique. *Ceramics International*. 2015;41.
102. Coondoo I, Panwar N, Amorín H, Ramana E, Algueró M, Kholkin A. Enhanced Piezoelectric Properties of Praseodymium-Modified Lead-Free (Ba_{0.85}Ca_{0.15})(Ti_{0.90}Zr_{0.10})O₃ Ceramics. *Journal of the American Ceramic Society*. 2015;98.
103. Chen B, Tian Y, Lu J, Wu D, Qiao X, Liang P, et al. Ultrahigh storage density achieved with (1-x)KNN-xBZN ceramics. *Journal of the European Ceramic Society*.

- 2020;40.
104. Zeng JT, Kwok KW, Chan HLW. $K_xNa_{1-x}NbO_3$ powder synthesized by molten-salt process. *Materials Letters*. 2007;61(2):409-11.
105. Rafiq MA, Tkach A, Costa M, Vilarinho P. Defects and charge transport in Mn-doped $K_{0.5}Na_{0.5}NbO_3$ ceramics. *Physical Chemistry Chemical Physics*. 2015.
106. Xu Y, Liu D, Lai F, Zhen Y, Li J. Fabrication of (K,Na) NbO_3 Lead-Free Piezoceramic Microrod Arrays by Sol–Gel Processing with Micromachined Silicon Templates. *Journal of the American Ceramic Society*. 2008;91:2844-7.
107. Lee JK, Kim JH, Cho JH, Kim BI, Kim ES. Electrical properties of $[Li_{0.04}(K_{0.5}Na_{0.5})_{0.96-x}Ag_x](Nb_{1-y}Sb_y)O_3$ ceramics. *Ceramics International*. 2012;38:S339-S42.
108. Kumar P, Pattanaik M, Sonia S. Synthesis and characterizations of KNN ferroelectric ceramics near 50/50 MPB. *Ceramics International*. 2013;39:65–9.
109. Dai H, Chen Z, Xue R, Li T, Chen J, Xiang H. Structural and electric properties of polycrystalline $Bi_{1-x}Er_xFeO_3$ ceramics. *Ceramics International*. 2013;39:5373–8.
110. Mahdi R, Al-Bahnam N, Ajeel M, al-keisy A, Ali T, W.H AM. High-performance (K,Na) NbO_3 -based binary lead-free piezoelectric ceramics modified with acceptor metal oxide. *Ceramics International*. 2020;46.
111. Chen X, Ruan X, Zhao K, He X, Zeng J, Li Y, et al. Low sintering temperature and high piezoelectric properties of Li-doped (Ba,Ca)(Ti,Zr) O_3 lead-free ceramics. *Journal of Alloys and Compounds*. 2015;632:103-9.
112. Yao Z, Luo Q, Xu C, Zhang L, Hao H, Yu Z, et al. Titanium deficiency in tetragonal-structured (Ba,Ca)(Zr,Ti) O_3 piezoelectric ceramics. *Journal of Alloys and Compounds*. 2017;712.
113. Wang J, Luo L, Huang Y, Li W, Wang F. Strong correlation of the electrical properties, up-conversion photoluminescence, and phase structure in Er^{3+}/Yb_{3+} co-doped $(1-x)K_{0.5}Na_{0.5}NbO_3-xLiNbO_3$ ceramics. *Applied Physics Letters*. 2015;107:192901.
114. Prasertpalichat S, Cann D. Hardening in non-stoichiometric $(1-x)Bi_{0.5}Na_{0.5}TiO_3-xBaTiO_3$ lead-free piezoelectric ceramics. *Journal of Materials Science*. 2015;51.
115. Hussain A, Sinha N, Goel S, Joseph A, Kumar B. Y^{3+} doped 0.64PMN-0.36PT

- ceramic for energy scavenging applications: Excellent piezo-/ferro-response with the investigations of true-remanent polarization and resistive leakage. *Journal of Alloys and Compounds*. 2019;790.
116. Li C-X, Yang B, Zhang S-T, Liu D-Q, Zhang R, Sun Y, et al. Effects of Mn doping on multiferroic and magnetocapacitive properties of $0.33\text{Ba}_{0.70}\text{Ca}_{0.30}\text{TiO}_3$ - 0.67BiFeO_3 diphasic ceramics. *Journal of Alloys and Compounds*. 2014;590:346-54.



BIOGRAPHY

Name-Surname	Surirat Yotthuan
Date of Birth	21 March 1993
Address	1/1 No. 3, Ban Na Sub-district, Wachirabarami District, Phichit Province, 66140
Education Background	2015 B.Sc. (Applied Physics) Naresuan University 2017 M.Sc. (Applied Physics) Naresuan University 2022 Ph.D. (Applied Physics) Naresuan University
Publication	<ol style="list-style-type: none">1. Yotthuan S, Janlong N, Pinitsoontorn S, Suriwong T, Wongdamnern N, Udeye T, Bongkarn T. Phase formation, microstructure, electric and magnetic properties of NiO doping in $(\text{Ba}_{0.85}\text{Ca}_{0.15})(\text{Ti}_{0.90}\text{Zr}_{0.10})\text{O}_3$ ceramics. <i>Integr. Ferroelectr.</i> 2022;222(1):149-162.2. Sinkruason T, Thawong P, Yotthuan S, Jutimoosik J, Bongkarn T. Effect of Fe_2O_3 Doping on Phase Formation, Microstructure, Dielectric and Magnetic Properties of BNT-BKT-KNN Ceramics Prepared by the Solid-State Combustion Technique. <i>Integr. Ferroelectr.</i> 2021;223(1):196-205.3. Yotthuan S, Udeye T, Vittayakorn N, Pulphol P, Bongkarn T. The influences of Cs^+ substitution and direct doping on the phase evolution, microstructure and electrical properties of KNNT ceramics. <i>Ferroelectrics.</i> 2021;586(1):133-146.4. Kornphom C, Yotthuan S, Kidkhunthod P, Bongkarn T. Stabilization of the morphotropic phase boundary in $(1-x)\text{BNT}-x\text{BCTS}$ ceramics prepared by the solid-state combustion technique. <i>Radiat. Phys. Chem.</i> 2021;188(1):109638-10.5. Yotthuan S, Rueanggam S, Pinitsoontorn S, Chootin S, Bongkarn T. The phase structure, microstructure, dielectric and magnetic properties of $0.99(\text{K}_{0.45}\text{Na}_{0.52}\text{Li}_{0.03})(\text{Nb}_{0.94}\text{Sb}_{0.06})\text{O}_3-0.01\text{BiScO}_3$ ceramics with NiO doping. <i>Integr. Ferroelectr.</i> 2021;214(1):56-68.6. Yotthuan S, Charoonsuk T, Vittayakorn N, Thountom S, Suriwong T, Udeye T, Bongkarn T. Effect of firing conditions on phase formation, microstructure, and electrical properties of $(\text{K}_{0.5}\text{Na}_{0.5})(\text{Nb}_{0.7}\text{Ta}_{0.3})\text{O}_3$ ceramics synthesized by solid-state combustion method. <i>J. Electron. Mater.</i> 2020;49(10):6143-6155.7. Yotthuan S, Kornphom C, Prasertpalichat S, Suriwong T, Pinitsoontorn S, Bongkarn T. Phase ratio, dielectric, ferroelectric, and magnetic properties of BCTZ ceramics

with CuO doping synthesized by the solid state combustion technique. *Phys. Status Solidi A*. 2019;216(11):1800803-14.

8. Yotthuan S, Suriwong T, Pinitsoontorn S, Chootin S, Bongkarn T. Phase formation, dielectric, ferroelectric and magnetic properties of Cr₂O₃ doped (Ba_{0.85}Ca_{0.15})(Ti_{0.90}Zr_{0.10})O₃ ceramics. *Integr. Ferroelectr.* 2019;195(1):154-165.

9. Kornphom C, Yotthuan S, Chootin S, Bongkran T. The Influence of the firing Temperatures on the phase evolution, microstructure, dielectric and strain responses of BCTS Ceramics prepared by the solid state combustion technique. *Phys. Status Solidi A*. 2018;215(21):1701058-9.

10. Yotthuan S, Suriwong T, Pinitsoontorn S, Bongkran T. Effect of Fe₂O₃ doping on phase formation, microstructure, electric and magnetic properties of (Ba_{0.85}Ca_{0.15})(Ti_{0.90}Zr_{0.10})O₃ ceramics. *Integr. Ferroelectr.* 2018;187(1):100-112.

11. Yotthuan S, Kornphom C, Bongkran T. The effect of firing conditions on phase formation, microstructure and dielectric properties of BNKTNb-LSb ceramics prepared via the combustion technique. *Phase Transitions*. 2015;88(10):1035-1043.

Awards

2020 Best oral presentation award in Thesis and innovation independent study awards for graduate students Naresuan University

2021 Best poster presentation award in Ferroelectrics and Related Materials Chulalongkorn University